Doctoral Thesis

Electron Correlation in Copper and Iron-Based High Temperature Superconductors: An Angle-Resolved Photoemission Spectroscopy Perspective

Author(s):
Matt, Christian E.

Publication Date:
2016

Permanent Link:
https://doi.org/10.3929/ethz-a-010811979 →

Electron Correlation in Copper and Iron-Based High Temperature Superconductors

An Angle-Resolved Photoemission Spectroscopy Perspective

Dissertation

Christian Egon Matt

DISS. ETH NO. 23855

DISS. ETH NO. 23855

Electron Correlation in Copper and Iron-Based High Temperature Superconductors

An Angle-Resolved Photoemission Spectroscopy Perspective

A thesis submitted to attain the degree of

DOCTOR OF SCIENCES of ETH ZURICH

(Dr. sc. ETH Zurich)

presented by

CHRISTIAN Egon MATT

MSc ETH Physics
Swiss Light Source, Paul Scherrer Institute, CH-5232 Villigen PSI, Switzerland
Laboratory for Solid State Physics, ETH Zürich, CH-8093 Zürich, Switzerland

born on 23.09.1987
citizen of Germany

accepted on the recommendation of

Prof. Dr. Ming Shi
Prof. Dr. Joël Mesot
Prof. Dr. Philipp Aebi

2016

Abstract

In the field of modern condensed matter physics, strongly correlated electron compounds form a class of materials which exhibit exotic physical properties. These systems usually have a rich phase diagram with many structural, magnetic and electronic phases. However, rarely a sufficient description for the physical properties is provided by established theories. A small change of composition or external conditions such as temperature or magnetic/electric field may induce a drastic modification of the physical properties in these materials. Adjacent phases might be competing for the ground state at zero temperature or supporting each other. Thus, fundamental interest lies in the characterization of neighboring phases and their relation which is often non-trivial.

This thesis presents experimental studies of the electronic properties in single crystals of cuprate and iron-pnictide compounds by means of angle-resolved photoemission spectroscopy (ARPES). Despite huge scientific efforts, the mechanism of high-temperature superconductivity in cuprates and iron-pnictides is still under intense debate. The richness and complexity of the cuprate and the iron-pnictide phase diagram demand a careful experimental characterization of the individual phases to pave the way for a successful theoretical description.

In $La_{1.6-x}Nd_{0.4}Sr_xCuO_4$ we have investigated the electronic structure of the charge ordered and the pseudogap phase which are adjacent to the high-T_c superconducting phase. Our systematic study of the temperature-, momentum- and doping-dependent line-shape evolution of the low energy single-particle spectral function has provided insights into the relation between these three phases.

A link between the cuprates and iron-pnictide superconductors has been established by the recent discovery of an insulating, antiferromagnetically ordered phase in heavily copper doped $NaFe_{1-x}Cu_xAs$ ($x = 0.44$). Our combined study based on density functional theory (DFT) calculations and ARPES experiments unveiled the electronic structure and identified electronic correlation effects due to on-site Coulomb interaction and Hund's coupling as the driving force for the insulating behavior.

After investigating the effects of strong electron correlation the focus has been put on the interplay between the metallic spacer layer and the superconducting layer in $Ca_{0.9}La_{0.1}FeAs_2$. We have found that the metallicity of the spacer layer has unexpectedly small influence on the electronic correlation in the Fe-As layer.

The last chapter of this thesis presents the electronic band structure of the recently discovered iron-pnictide system $Pr_4Fe_2As_2Te_{1-x}O_4$. We revealed that the Fermi surface (FS) consists only of electron-like pockets centered at the corner of the Brillouin zone. So far, such a FS-topology has only been observed in heavily electron doped iron-chalcogenides. These findings impose strong constrains on the theoretical description of the superconducting pairing mechanism.

Zusammenfassung

Auf dem Gebiet der modernen Festkörperphysik bilden stark korrelierte Elektronensysteme eine Materialklasse, welche exotische physikalische Eigenschaften aufweist. Diese Systeme haben üblicherweise ein reichhaltiges Phasendiagramm mit diversen strukturellen, elektronischen und magnetischen Phasen. Etablierte Theorien liefern jedoch selten eine genaue Beschreibung der physikalischen Eigenschaften dieser Systeme. Eine kleine Änderung der Zusammensetzung oder eine kleine Variation externer Bedingungen wie Temperatur oder magnetischer oder elektrischer Felder können die physikalischen Eigenschaften dieser Materialien drastisch verändern. Nebeneinanderliegende Phasen können zum Beispiel von konkurrierendem Charakter sein und um den Grundzustand am Nullpunkt kämpfen oder sie können sich gegenseitig begünstigen. Deshalb besteht grundsätzliches Interesse in der Charakterisierung von benachbarten Phasen und deren gegenseitigen, oft nichttrivialen Beziehungen.

In dieser Thesis werden experimentelle Studien der elektronischen Eigenschaften von einkristallinen Kupraten und Eisenpniktiden, basierend auf winkel-aufgelöster Photoemissionsspektroskopie (ARPES), präsentiert. Trotz enormer wissenschaftlicher Anstrengung ist der Mechanismus der Hochtemperatursupraleitung in Kupraten und Eisenpniktiden immer noch Thema strittiger Diskussionen. Die Reichhaltigkeit und Komplexität des Kuprat- und Eisenpniktid-Phasendiagramms verlangt nach einer sorgfältigen experimentellen Untersuchung der einzelnen Phasen um den Weg für eine erfolgreiche theoretische Beschreibung zu ebnen.

In unseren Forschungsarbeiten haben wir die elektronische Struktur in der ladungsgeordneten Phase und in der Pseudogap Phase von $La_{1.6-x}Nd_{0.4}Sr_xCuO_4$ untersucht, welche sich beide in direkter Umgebung der hoch-T_c supraleitenden Phase befinden. Unsere systematische Studie der Linienform der ein-Teilchen Spektralfunktion in Abhängigkeit von Temperatur, Impuls und Dotierung ermöglicht Rückschlüsse über die Beziehung zwischen diesen drei Phasen.

Eine Verbindung zwischen Kuprat- und Eisenpniktid-Supraleitern wurde durch die kürzliche Entdeckung einer isolierenden, antiferromagnetisch geordneten Phase in stark kupferdotiertem $NaFe_{1-x}Cu_xAs$ ($x = 0.44$) gefunden. Unsere kombinierte Studie, basierend auf dichtefunktionaltheoretischen Berechnungen und ARPES Experimenten hat die elektronische Struktur aufgedeckt und hat herausgefunden, dass elektronische Korrelationen wegen Coulomb-Abstossung und Hund'scher Regel die Hauptursache für den isolierenden Zustand sind.

Nach der Untersuchung von Effekten durch stark korrelierte Elektronen wurde der Fokus auf den gegenseitigen Einfluss der metallischen Zwischenschicht und der supraleitenden Schicht in $Ca_{0.9}La_{0.1}FeAs_2$ gesetzt. Wir haben herausgefunden, dass der metallische Charakter der Zwischenschicht unerwartet kleinen Einfluss auf elektronische Korrelationen in der Fe-As Schicht hat.

Das letzte Kapitel dieser Thesis beinhaltet die elektronische Struktur der kürzlich entdeckten Eisenpniktidverbindung $Pr_4Fe_2As_2Te_{1-x}O_4$. Unsere Studie hat gezeigt, dass die Fermioberfläche nur aus Elektronartigen Fermiflächen an den Ecken der Brillouin-Zone besteht. Solch eine Topologie der Fermioberfläche wurde in der Gruppe der eisenbasierten Supraleiter bisher nur bei stark Elektron-dotierten Eisen-Chalkogen Verbindungen gefunden. Diese Entdeckungen sind mit starken Einschränkungen für die theoretische Beschreibung des supraleitenden Paarungsmechanismus verbunden.

Contents

List of abbreviations and acronyms

Cuprate:	copper-oxide based compound
SCM:	Strongly correlated material
SC:	Superconductor
CDW:	Charge density wave
SDW:	Spin density wave
OP:	Order parameter
BCS:	Theoretical description for superconductivity by John Bardeen, Leon Cooper, John-Robert Schrieffer [1]
BEC:	Bose-Einstein condensate
HTSC:	High temperature superconductor (mainly cuprates and iron-pnictides)
PG:	Pseudogap
FL:	Fermi liquid
FS:	Fermi surface

Variables:

h:	Planck's constant
E_{F} :	Fermi energy
J_{H} :	Hund's coupling energy
U:	On-site Coulomb repulsion
J:	Magnetic superexchange coupling
T_{c} :	superconducting transition temperature
T_{N} :	Néel temperature
T_{S} :	structural transition temperature
E_{B} :	Binding energy
m^*:	effective mass of electron
e:	charge of electron
c:	speed of light
FWHM:	Full width at half maximum
HWHM:	Half width at half maximum

Experimental and theoretical techniques

PSI:	Paul Scherrer Institut
SLS:	Swiss Light Source
SIS:	Surface and Interface Spectroscopy (beamline)
ADRESS:	Advanced Resonant Spectroscopies (beamline)
CARVING:	Complete Angle Resolved Variation for electron spectroscopy IN villiGen
UHV	Ultra High Vacuum
HARPES:	High-resolution angle-resolved photoemission spectroscopy
SARPES:	Spin and angle-resolved photoemission spectroscopy
SX-ARPES:	Angle resolved photoemission spectroscopy in the soft X-ray regime 200eV $< h\nu <$ 1200 eV
UV-ARPES:	Angle resolved photoemission spectroscopy in the ultraviolet regime 20eV $< h\nu <$ 200 eV
VUV:	Vacuum-Ultra-Violet
PE:	Photoemission
UV:	Ultraviolet
SX:	Soft X-ray
PES:	Photoelectron spectroscopy
XRD:	X-ray diffraction
DFT:	Density functional theory
DMFT:	Dynamical mean field theory
RPA:	Random Phase Approximation
GGA:	Generalized Gradient Approximation

Compounds

LBCO:	$La_{2-x}Ba_xCuO_4$
LSCO:	$La_{2-x}Sr_xCuO_4$
NdLSCO:	$La_{1.6-x}Nd_{0.4}Sr_xCuO_4$
LCO:	La_2CuO_4
Tl2201:	$Tl_2Ba_2CuO_{6+\delta}$
Bi2201:	$Bi_2Sr_2CuO_{6+\delta}$
Bi2212:	$Bi_2Sr_2CaCu_2O_{8+\delta}$
Bi2223:	$Bi_2Sr_2Ca_2Cu_3O_{10+\delta}$
YBCO:	$YBa_2Ca_3O_{7-\delta}$
Ba122:	$BaFe_2As_2$
Li11111:	$Li_{1-x}Fe_x)OHFeSe$
FeSe/STO:	monolayer FeSe on $SrTiO_3$
FePN:	Iron-pnictides
FeCH:	Iron-chalcogenides
IBSC:	Iron based superconductor

Chapter 1

Concepts in condensed matter physics

1.1 Introduction

The field of condensed matter physics is devoted to the study of physical properties in solid and liquid phases of matter. The different kinds of solids which are permanently present in our everyday life consist of a huge number of particles (protons, electrons, neutrons, etc.) which is in the order of 10^{23}. Often, these particles are not just randomly distributed but develop different kinds of structurally, electronically or magnetically ordered states as a result of their mutual interaction. Every state of matter provides its own characteristics and features which might transform a particular solid into useful device.
A particular electronic phase which has been hidden to humans for a long time is the superconducting state, - that is the completely unhindered flow of electricity. It has only been discovered around a century ago as a phenomenon which was limited, at that time, to very low temperatures below ~ 30 K. For higher temperatures these solids are in a metallic phase with finite resistivity and for a long time it was not clear what kind of interactions drive the system into this exotic state. Around 50 years later a group of theoreticians (John Bardeen, Leon Cooper and John R. Schrieffer) discovered that a complex interplay between the electrons and the crystal lattice is the key for superconductivity [1]. On that basis it was also predicted that such a technologically important state might not be realized at room temperatures but confined to lowest temperatures [2]. For that reason it came as a big surprise when superconductivity was discovered in 1986 in copper-based ceramics at temperatures well above the technologically important boiling point of nitrogen of 77 K [3]. The new discovery attracted an enormous boost in research activity since it was clear that the description for superconductivity in these new compounds must be different from the one of the already known superconductors. It has been suggested that new types of interactions must be responsible for the drastic enhancement of the superconducting transition temperature T_c. With the discovery of high-temperature superconductivity in materials containing the magnetic element iron, 25 years later, the physical description of high-temperature superconductivity has settled as one of the most important unsolved problems in the field of condensed matter physics [4].

1.2 Many-body systems

A solid is an ensemble of a large number of atoms ($\mathcal{O}(23)$). Each atom consists of a positively charged nuclei and Z_i negatively charged electrons. All physical properties and information about the system are contained in the many-particle wavefunction $\Psi(\mathbf{R}_i, (\mathbf{r}_j \mathrm{s}_j))$ which could

be obtained by solving the many-particle Schrödinger equation:

$$H|\Psi\rangle = [T+V]|\Psi\rangle = E|\Psi\rangle \tag{1.1}$$

It is not particularly hard to formulate a 'microscopic' Hamiltonian H [5, 6]. H can be split into parts which describe the ionic nucleus, the electrons and the interaction between them:

$$H = H_{\text{el}} + H_{\text{ion}} + H_{\text{el-ion}} \tag{1.2}$$

$$\begin{aligned} H_{\text{el}} = V_{\text{el-el}} + T_{\text{el}} &= +\frac{1}{8\pi\epsilon_0}\sum_{i\neq j}\frac{e^2}{|\mathbf{r}_i-\mathbf{r}_j|} - \frac{\hbar^2}{2}\sum_i \frac{\nabla_i^2}{m_e} \\ H_{\text{ion}} = V_{\text{ion-ion}} + T_{\text{ion}} &= \frac{1}{8\pi\epsilon_0}\sum_{i\neq j}\frac{e^2 Z_i Z_j}{|\mathbf{R}_i-\mathbf{R}_j|} - \frac{\hbar^2}{2}\sum_i \frac{\nabla_i^2}{M_i} \\ H_{\text{el-ion}} &= -\frac{1}{4\pi\epsilon_0}\sum_{i\neq j}\frac{e^2 Z_i}{|\mathbf{R}_i-\mathbf{r}_j|} \end{aligned}$$

where M_i and R_i is the mass and position of the nucleus and m_e, r_i and s_i is the mass, position and spin of the electron, respectively. The first terms in each line of the equation [eq. 1.2] represent the potential terms and the latter the kinetic terms of the electrons and nuclei, respectively. However, an exact solution of the Schrödinger equation with this Hamiltonian is far from feasible. One problem, and probably the hardest, is certainly the sheer number of involved particles which is in the order of $\mathcal{O}(23)$.

1.3 Correlated electrons - a one-electron problem

Progression in solving an equation such as eq. 1.1 requires a simplifications of the many body problem. One idea to describe the N electrons in the system is to reformulate the many body problem and consider a single electron in an effective potential build by the nuclei and the other $N-1$ electrons. The one-particle Schrödinger equation for the electron is then formulated as

$$-\frac{\hbar^2}{2m}\nabla^2\psi_i(\mathbf{r},s) + U_i(\mathbf{r})\psi_i(\mathbf{r},s) = \varepsilon\psi_i(\mathbf{r},s) \tag{1.3}$$

where $U_i(\mathbf{r}) = V_{\text{el-el}} + V_{\text{el-ion}}$ denotes the effective potential for the i^{th} electron. The set of all N one-particle equations is known as the *Hartree equations* and can be solved self-consistently in an iterative process. As starting point a U has to be guessed. The drawback of this approximation is that it fails to describe particular arrangements of the remaining $N-1$ electrons since they are treated like an average potential field.
Important physical properties such as exchange interaction, electron-electron interactions, screening, etc. are not captured by the Hartree equations. The, for a fermionic system essential exchange term (Fock term), should be added on the left hand side of equation 1.3. However, its integral form ($\int V(r,r')\psi(r')dr'$) makes the problem again intractable. Different theoretical and computational methods have been developed to solve the Hartree equation which are able to treat many-body effects in different ways [see section 1.11].

1.4 Strongly correlated electron materials

Strong many-body interactions are found in many materials. Especially systems which contain elements with partially filled $d-$ or f-shells, so called *transition metal* and *rare-earth* compounds, respectively. Many exotic phenomena have been emerging in the past

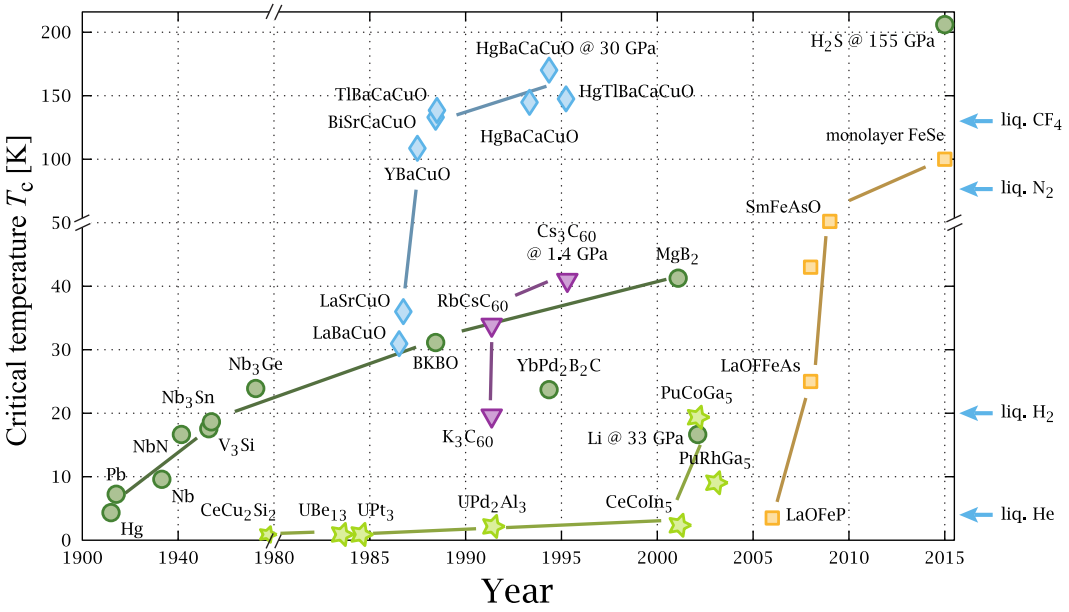

Figure 1.1: Timeline of discovery of various superconductors represented by their heighest transition temperature T_c. Cuprates are denoted by blue diamonds, and iron-pnictides by yellow squares [13]. Note the jump in the time and temperature axis.

decades in these *strongly correlated materials* (SCM).
With the explanation of the metal-insulator transition (MIT) in nickel-oxide perovskites (due to electron-electron correlation in 1938 [7, 8]), a new field of condensed matter research was born and many discoveries of huge scientific and technological relevance have followed. Certainly one of the most relevant phenomena for applications was the discovery of the colossal magnetoresistance (CMR) effect in manganese-oxides (manganites) e.g. $LaMnO_3$ [9, 10]. A magnetoresistant material changes it's electrical resistance up to several orders of magnitudes in the presence of a magnetic field, and is nowadays used in read-heads of hard-disc drives for data-storage. Another class of strongly correlated materials are the heavy fermion compounds (material containing rare-earth elements) where the effective mass of the charge carriers is enhanced by thousand times compared to the free electron mass. These compounds host interesting features e.g. a phase transition between superconductivity and magnetism [11, 12]. Furthermore the discovery of high temperature superconductivity in perovskite structured copper-oxides ceramics [3] in 1987 and in metallic, layered iron-pnictide compounds [4] in 2008 is certainly of high impact and relevant in the field of strongly correlated systems.

Soon after the initial discovery of superconductivity occurring at 35 K in $La_{2-x}Ba_xCuO_{4+\delta}$ by Bednorz and Müller [3] the transition temperature (T_c) has been pushed above the technological critical temperature of liquid nitrogen in $YBa_2Cu_3Cu_{7-\delta}$, $T_c = 90$ K [14]. For several years T_c kept rising, reaching up to ~ 135 K (at ambient pressure) in mercury based cuprates [15] and ~ 165 K under application of external pressure [16].
With the discovery of high temperature superconductivity in iron-based compounds a similar race of pushing the critical temperature to higher values has been initiated. Up to date the family of iron-based superconductors (IBSC) keeps growing. In variety they exceed by far the copper-oxides but the record T_c of ~ 55 K for bulk crystals [17] has not reached the level of the cuprates, yet. The timeline-plot [see Fig. 1.1] summarizes the history of important discoveries in the field of superconductivity.

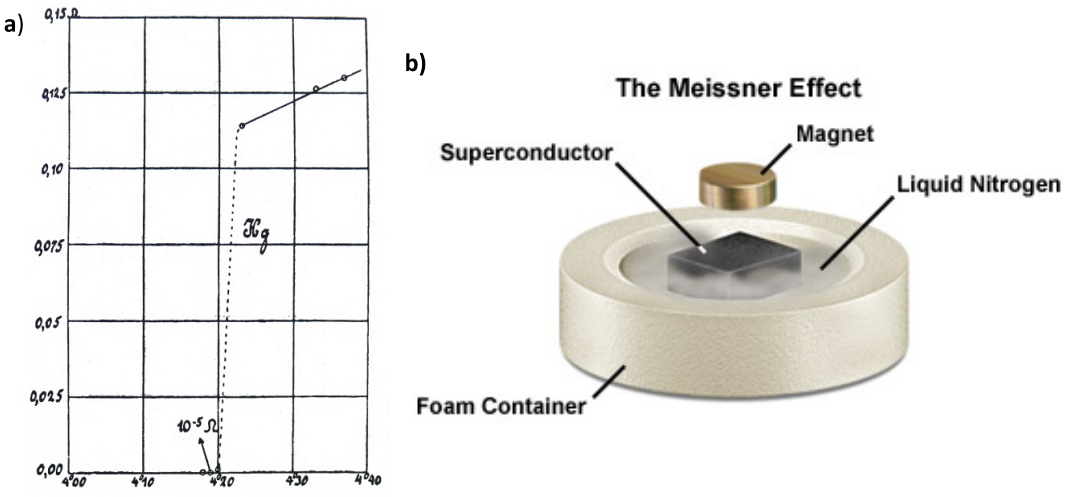

Figure 1.2: **(a)** Historic plot of the resistance (in ohms) versus temperature (Kelvin) of mercury [18]. **(b)** Experimental setup for demonstration of the Meissner effect. The levitation of the magnet is the result of the expulsion of the permanent magnet's field from the interior of the superconductor [19].

1.5 Superconductivity: An unexpected discovery

Historically, superconductivity was discovered in 1911 by H. Kammerlingh Onnes [18] in his research on the microscopic source of electrical resistance in metals. With his unique cryogenic facility, he was the first to liquify helium and perform resistivity measurements at temperatures below 4K where he observed a sudden jump to zero resistivity in mercury [see Fig. 1.2 a)]. In the subsequent years, superconductivity has been observed in a number of elemental metals [see Fig. 1.1, and Figure 1.3]. In 1933, perfect diamagnetism was observed by Meissner and Ochsenfeld and quickly established as the second hallmark of superconductivity [21]. Perfect diamagnetism, that is the complete expulsion of magnetic field from inside the superconductor is known as the Meissner effect. Usually, the Meissner effect is demonstrated in a setup as sketched in Figure 1.2 b). In the superconducting state the screening currents on the surface of a superconductor produce a magnetic field opposed to the external field.

Despite the huge attraction and relevance of the topic theoretical understanding of superconductivity only slowly developed. The phenomenological theories of the London brothers for electromagnetic fields in superconductors in 1935 [22] and Ginzburg and Landau about phase transitions [23] have been the first relevant theoretical contributions in the topic. Only in the 1950s, a full microscopic theory has been developed by Bardeen, Cooper and Schrieffer [1] which was capable to fully describe superconductivity.

1.6 BCS theory

In this subsection we briefly introduce the theory by Bardeen, Cooper and Schrieffer (BCS) with its basic idea about the pairing-mechanism which leads to superconductivity. A full treatment of the problem in all its details can be found in a vast number of books. An easy to read introduction with intuitive explanations is for example provided by Tinkham, [24], and a more technical treatment in [25, 26]. The BCS theory explains superconductivity arising due to a tiny attractive interaction between electrons which is mediated by lattice vibrations (phonons) [27]. The electrons form *Cooper pairs* which can be considered as quasiparticles with integer spin. Therefore they obey the Bose statistics which allows them to condense

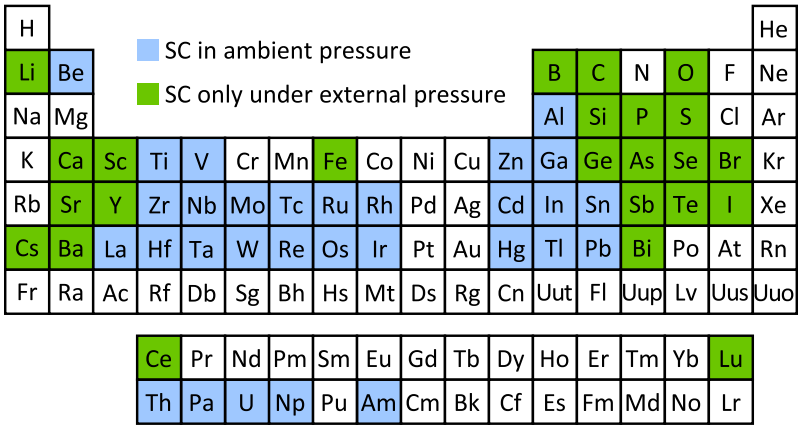

Figure 1.3: Periodic table indicating superconducting elements. Elements in blue are superconducting at ambient pressure and elements in green are only superconducting under external pressure. [20].

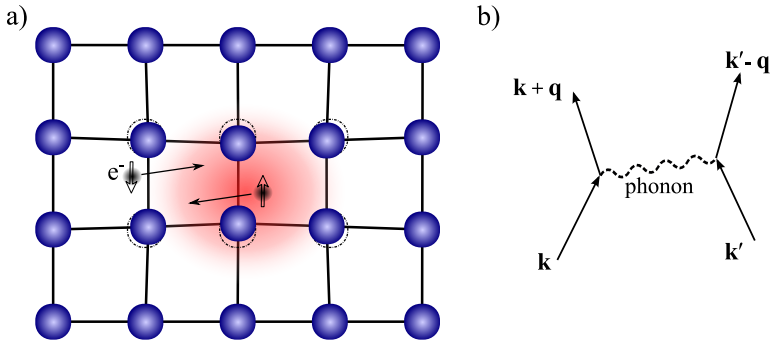

Figure 1.4: **(a)** Schematic of the retarded effective pairing interaction between electrons in a Cooper pair with opposite spin and momenta mediated by the lattice (phonons). Red area represents net positive charge "cloud" due to displacement of ions. **(b)** Diagrammatic representation of electron-phonon interaction.

into a single quantum state analogous to a Bose-Einstein condensate. The energy gain of the system transiting into the superconducting state therefore results mainly from the new ground state which has no longer to obey the Pauli exclusion principle. The Cooper-pair electrons in the BCS theory are singlet states with anti-parallel spin alignment and with opposite momenta. The (truncated) BCS pairing Hamiltonian in which the interaction term contains only the attraction between electrons with opposite spin σ and momenta $\mathbf{k}$ is written as:

$$H = \sum_{\mathbf{k},\sigma} \epsilon_{\mathbf{k}} n_{\mathbf{k}\sigma} + \sum_{\mathbf{k},\mathbf{k}'} V_{\mathbf{k},\mathbf{k}'} c^{\dagger}_{\mathbf{k}\uparrow} c^{\dagger}_{\text{-}\mathbf{k}\downarrow} c_{\text{-}\mathbf{k}'\downarrow} c_{\mathbf{k}'\uparrow} \tag{1.4}$$

Where $c^{\dagger}$ and c are the electron creation and annihilation operators, $n_{\mathbf{k}\sigma} = c^{\dagger}_{\mathbf{k}\sigma} c_{\mathbf{k}\sigma}$, $\epsilon_{\mathbf{k}}$ is the energy of the electron at momentum $\mathbf{k}$ and $V_{\mathbf{k},\mathbf{k}'}$ is the effective attractive interaction potential. As sketched in Figure 1.4, the physical idea for the origin of the net attractive interaction is that an electron polarizes the medium by a local distortion of the surrounding ionic nuclei lattice. This polarized "cloud", in turn, attracts a second electron [see Fig. 1.4 a), b)]. In this picture, the characteristic frequency is the phonon frequency and the interaction is proportional to $(\omega^2 - \omega^2_{\mathbf{q}})^{-1}$ with $\omega_{\mathbf{q}}$ the frequency of the phonon with momentum $\mathbf{q} = \mathbf{k} - \mathbf{k}'$ [see Fig. 1.4, b)]. An upper cutoff for the electron energy is then given by the Debye

frequency ω_D. Historically, the BCS theory was formulated to describe superconductivity mediated by phonons for which a momentum independent interaction potential $V_{\mathbf{k},\mathbf{k}'} = -V$ can be assumed in the vicinity of E_F.

BCS theory and the phenomenological theory by Ginzburg-Landau describe the phase transition between the normal and superconducting state as a second order phase transition which breaks the U(1) gauge symmetry. The corresponding order parameter Δ which is zero for $T > T_c$ and non-zero for $T < T_c$ is given by:

$$\Delta_{\mathbf{k}} = -\sum_{\mathbf{k}'} \Theta(\omega_D - |\epsilon_{\mathbf{k}'}|) V_{\mathbf{k},\mathbf{k}'} \langle c_{\text{-}\mathbf{k}'\downarrow} c_{\mathbf{k}'\uparrow} \rangle \tag{1.5}$$

where, Θ denotes the heavyside function and the brackets stand for the quantum and statistical average in a mean-field approach. In general, the order parameter (OP) is a complex number $\Delta = |\Delta| \exp(i\phi_{\text{sc}})$ where the amplitude is a measure for the superfluid density in the superconducting state. The phase ϕ_{sc} is arbitrary but unique, thus reflecting the macroscopic phase coherence of the superfluid condensate. When the system enters the superconducting state the electronic band dispersion, $\epsilon_{\mathbf{k}}$, gets modified by opening a quasiparticle gap at the Fermi level. The modified quasiparticle dispersion is then given by $E_{\mathbf{k}} = \sqrt{\epsilon_{\mathbf{k}}^2 + |\Delta(\mathbf{k})|^2}$. In BCS theory, which is a *weak-coupling* theory, the order parameter $\Delta(\mathbf{k})$ and critical temperature T_{c} are connected via the following relation.

$$2|\Delta| = 3.52 k_B T_c \tag{1.6}$$

In the weak coupling limit, $\lambda = N(0)V \ll 1$ with $N(0)$ denoting the density of states (DOS) at the Fermi level, T_{c} is given by

$$T_c = 1.13 \hbar \omega_D e^{1/\lambda}. \tag{1.7}$$

In BCS-described, phonon-mediated superconductivity with broken gauge symmetry, $\Delta(\mathbf{k})$ is isotropic in momentum-space. The compounds belonging to this class are called *conventional s-wave* superconductors.
In more exotic, unconventional, superconductors like the heavy fermion compounds or high-T_{c} cuprate and iron-based superconductors, the interaction potential $V_{\mathbf{k}\mathbf{k}'}$ might be anisotropic resulting in an order parameter with a different symmetry. It is now well established that copper-oxide superconductors have d-wave symmetry which is also the most probable scenario for heavy-fermion superconductors. In the case of iron-pnictide superconductors the strongest candidate at the moment of writing is a $s^{\pm}$ symmetry. The key question in the research of unconventional superconductivity which is directly connected to the superconducting order parameter is the origin of the attractive potential. The community is far from reaching consensus about the exact microscopic mechanism in any family, neither in the iron and copper based high-T_{c} superconductors nor in heavy-fermion superconductors.

1.7 Unconventional superconductivity in copper- and iron-based compounds

1.7.1 Introduction

In the following section the basic physical properties of copper- and iron-based superconductors (IBSC), which will be called high-T_{c} superconductors from now on, will be discussed and compared with the conventional BCS-superconductors. Immediately after the discovery of high-T_{c} superconductivity in the La-Ba-Cu-O system it became clear that superconductivity must be fundamentally different from the so far known superconductors (SC) in several key aspects [30, 31]. The most important difference is the enormous boost of the transition temperature to values which are difficult to be explained by electron-phonon coupling. Also, the

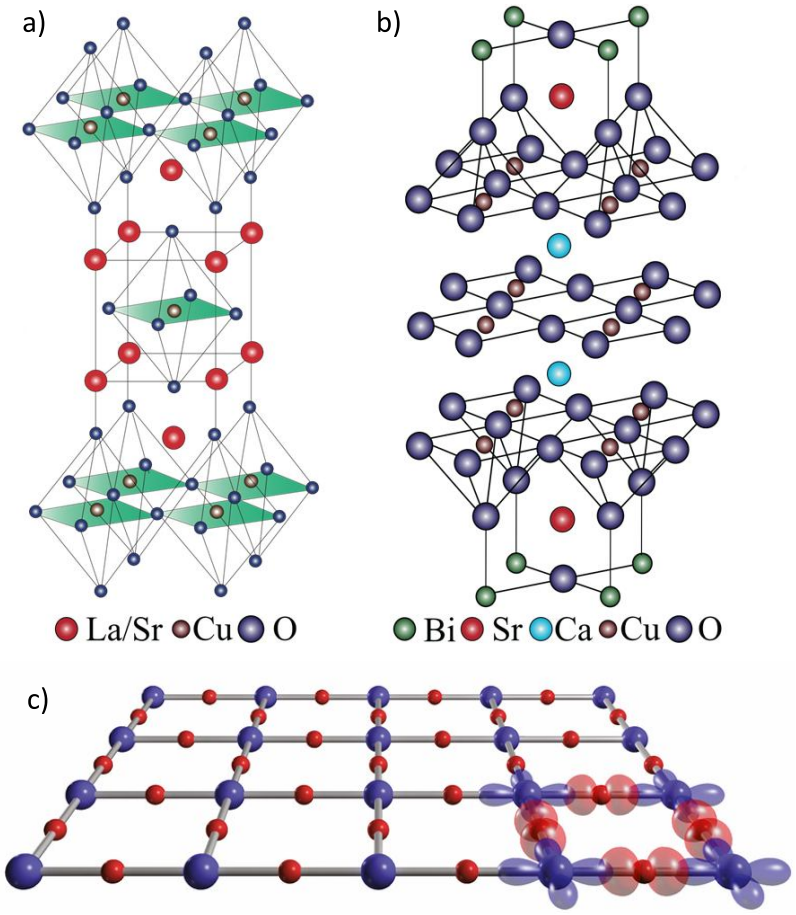

Figure 1.5: Crystal structure of cuprate SCs: **(a)** Crystal structure of $La_{2-x}Sr_xCuO_4$. **(b)** Crystal structure of $Bi_2Sr_2Ca_2Cu_3O_{10+\delta}$. [28]. Cu-O layer which is universal for all cuprates. Cu $d_{x^2-y^2}$ and O p_x/p_y-orbitals are indicated. [29]

maximum T_c values in iron-based superconductors were substantially higher than the ones of the known conventional superconductors and exceeding the McMillan limit, the theoretical upper limit of phonon-mediated BCS-described superconductivity [2][1]. A second significant distinction between conventional superconductors and copper- and iron-based superconductors is the crystal structure which is three dimensional for conventional but layered for all the copper and iron-based superconductors. The layered structure is reflected in the electronic structure which turns out to be quasi two-dimensional in the high-T_c compounds but much more dispersive along the third dimension in conventional SCs.

1.7.2 Conventional and high-T_c superconductors: Not entirely different

Despite these significant differences, the high-T_c SCs and conventional SCs share several commonalities. A very fundamental similarity is that in both, conventional and high-T_c superconductors, the electrons condense into spin-singlet Cooper pairs as seen in several

[1]Recently, H_3S was discovered to be superconducting with T_c = 203 K under ultrahigh pressure (155 GPa). At the moment of writing the pairing mechanism is still under debate but indeed strong indications point towards a conventional BCS superconductor[32]. Therefore the limit for $T_{c,max} \sim 40$ K proposed by McMillan might not be the ultimate limit.

experiments on cuprates [33] and the iron-pnictides [34–36][2]. Secondly, the magnetic flux quantization $\Phi = h/2e$ is observed in either type of superconductor [38–40], confirming the pairing of 2 electrons into a new quasiparticle with the basic charge of $2e$. Besides these, the conventional superconductors and the high-T_c compounds share the basic properties of zero electrical resistivity, perfect diamagnetism (Meissner-Ochsenfeld effect), Josephson effect, jump in specific heat at T_c and an energy gap in the electronic spectrum [41]. In the following two sections, basic features of both the cuprate and the iron-based superconductors (IBSCs) will be discussed in more detail.

1.8 Cuprate superconductors

The high-T_c cuprate superconductors have a layered perovskite-related crystal structure as sketched in Figure 1.5 and belong to the large class of ceramic materials. The common building block of all cuprates is the square planar CuO_2 layers [Fig. 1.5 c)] which are separated by insulating layers, so-called *charge-reservoir layers* [42]. One way of introducing charge carriers into the CuO_2 layers is by chemical substitution of atoms in those spacer layers with elements having excess holes or respectively electrons. The additional charge carriers are transferred to the CuO_2 layer. This kind of doping turns out to be a relatively "clean" method since it doesn't introduce disorder directly into the CuO_2 layer. Thus, the CuO_2 layer which is believed to be essential for superconductivity is not directly distorted by the substituting atoms. The cuprates are classified according to the parameter N which is the number of CuO_2 layers per unit cell -i.e. *singlelayer, doublelayer, ...* compounds. Figure 1.5 a) shows the crystal structure of the prototypical single-layered cuprate compound $La_{2-x}Sr_xCuO_4$ (LSCO) and Figure 1.5 b) the crystal structure of the triple-layered $Bi_2Sr_2Ca_2Cu_3O_{10+\delta}$(Bi2223). The effect of the layer number N on superconductivity is profound. Within a family, the maximum T_c increases with N for $N \leq 3$ [43, 44].

1.8.1 Electronic structure of cuprates

The low energy electronic states are provided by the CuO_2 layer which therefore determine all the macroscopic electronic properties of the compound [48]. For example, the conductivity in the CuO_2 plane is typically $10^3 - 10^4$ times larger than along the c-direction, perpendicular to the layers. The following discussion will be based on LSCO since it is the main cuprate material studied in this work, and is one of the simplest cuprates concerning the crystal structure and chemical composition. However, the discussion is representative for all the cuprates since it is mainly focused on the common CuO_2 layer. In the undoped parent compound ($La_{2-x}Sr_xCuO_4$, $x = 0$) , the valency of copper is Cu^{2+} implying a $3d^9$ configuration of the d-orbitals. Due to the crystal field, the d levels are split into t_{2g} and e_g levels which are further separated due to a Jahn-Teller distortion of the CuO_6 octahedra as scetched in Figure 1.6 d). The highest Cu-d level, $d_{x^2-y^2}$, is half filled at $x = 0$ and hybridized with O $2p_x$ and O $2p_y$ forming three bands, the bonding (B), non-bonding (NB) and antibonding (AB) band. While the B and NB band are both fully occupied, the AB band is half filled and crossing the Fermi level (E_F) [see Fig. 1.6 b)]. Therefore the low energetic bandstructure is often described in a effective three-band model [30, 49]. This picture is consistent with density functional theory (DFT) calculations -i.e. the AB-band is the topmost band, crossing E_F and the other Cu $3d$ and O $2p$ bands are fully occupied [see Fig. 1.6 c)] 1.7 a-d). In this picture, the undoped parent compound is predicted to be a metal. However, in reality it is found to be an antiferromagnetically ordered insulator with an energy gap of 2 eV [50, 51].
In the so-called *Mott-Hubbard* insulating state, the on-site Coulomb repulsion between the electrons on the Cu-site, the Hubbard U, is much larger than the electron kinetic energy

[2]Note: Spin-singlet formation is not a common feature among all superconductors. For example it is widely believed that Sr_2RuO_4 is a p-wave, spin-triplet superconductor [37].

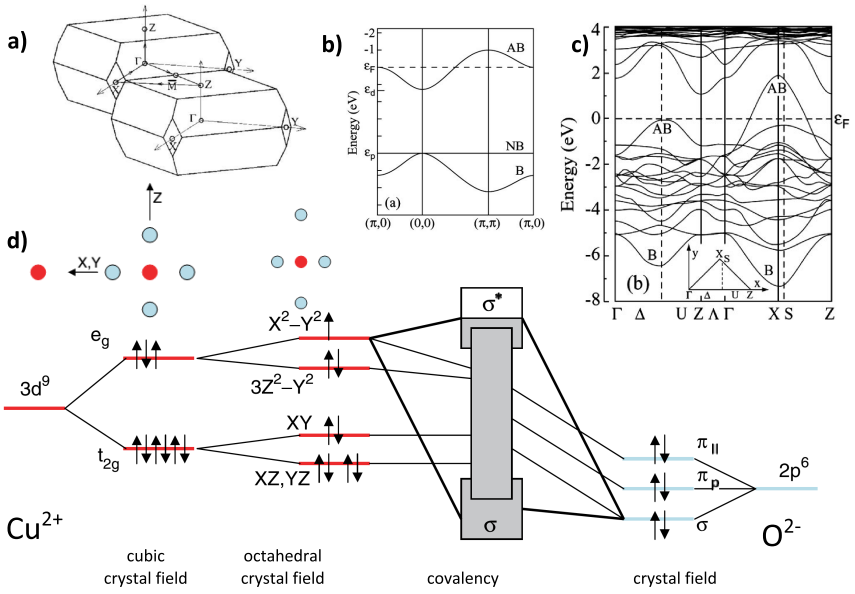

Figure 1.6: Energy levels of cuprate superconductors I: **(a)** Brillouin zone of La_2CuO_4. **(b)** Bonding (B), Non-bonding (NB) and antibonding (AB) bands of the Cu-O plaquette [see Fig. 1.7 e)] [45]. **(c)** Band structure calculations for La_2CuO_4 [46]. **(d)** Crystal field splitting and hybridization of the Cu 3*d* and O 2*p* states in LCO [47]. Adapted from [44, 48]

t which is given by the band width W. The large U induces a splitting of the conduction band into a lower Hubbard band (LHB) and an upper Hubbard band (UHB) [see Fig. 1.7 a, b)] [52–54]. In the case of the cuprates, however, the charge-transfer energy Δ between Cu-sites and O-sites is smaller than U resulting in an inversion of the energy levels of those states. These systems (with $\Delta < U$) are then called *charge-transfer insulators* [see Fig. 1.7 c)] [55].

1.8.2 The cuprate phase diagram

A typical temperature versus hole doping phase diagram of cuprates is shown in Figure 1.8. It is exceptionally rich and hosting many phases adjacent to superconductivity; some of them have only been recently discovered [59] and many are still far from being fully understood [56]. The following paragraph will briefly introduce each phase with its characteristic properties and physical parameters. It turns out, that superconductivity lies in a range of doping which so far defies a proper description, not only for superconductivity but also the surrounding phases. However, on the extreme doping sides i.e. the Mott-insulating parent compound and the heavily doped Fermi-liquid metallic state, the situation is less complex and the physics is fairly well accounted for by existing theories [30, 60–62].

Insulating region

The parent compound is an antiferromagnetically ordered insulator resulting from strong electron-electron correlations as described by the Mott-Hubbard model [30] [see Figure 1.8 b)]. The kinetic energy gain, t, of an electron hopping from one Cu site to another is much smaller than to on-site Coulomb repulsion U of the d electrons on the Cu sites[3]. Due to the strong covalent bonding between Cu $3d_{x^2-y^2}$ and O p orbitals, the lowest energy excitation is a charge transfer-excitation with a charge transfer gap of $\Delta \sim 2$ eV [64] [see Fig. 1.7 c)].

[3]Calculations estimate U in the order of 8 - 10 eV [63].

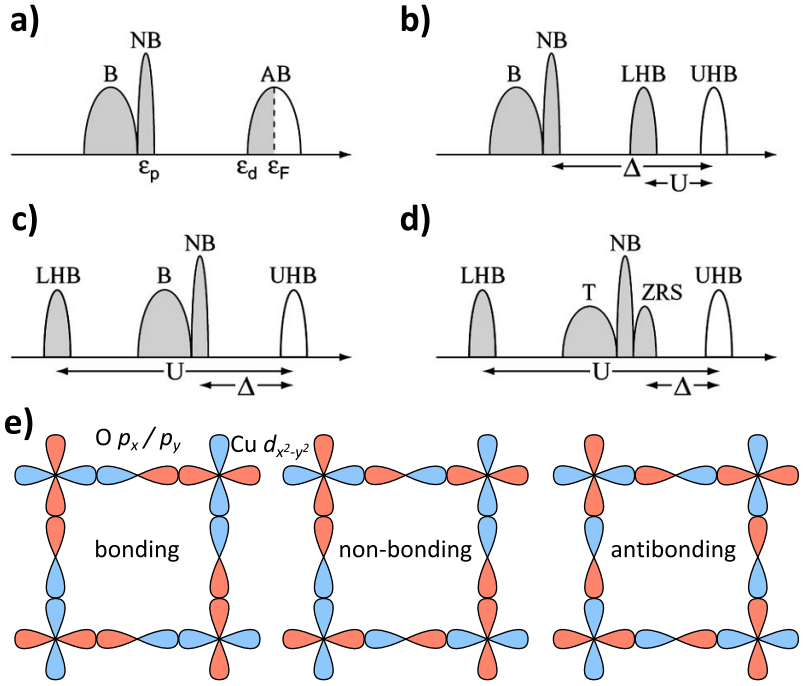

Figure 1.7: Energy levels of cuprate superconductors II: Density of states (DOS) for **(a)** the non interacting, metallic case; **(b)** the Mott insulating case ($\Delta > U$). **(c)** a charge transfer insulator ($U > \Delta > W$) **(d)** the splitting of the Nonbonding band into triplet and Zhang-Rice singlet states. **(e)** Cu-O plaquette, forming bonding, non-bonding and antibonding hybridized wave functions. Adapted from [44, 48]

Below $T_N \sim 300$K, the local magnetic moments of the Cu atoms are aligned anti-parallel due to superexchange interaction. In this picture, spins can virtually hop between the Cu sites via the intermediate O $2p$ orbitals. The coupling strength between the neighboring spins is given by[4] $J \sim t_{\text{eff}}^2/U_{dd}$. Due to the relatively small size of the charge-transfer gap Δ, J is expected to be strong, as confirmed by experimental values $J \sim 0.11 - 0.13$ eV [66, 67].

Fermi-liquid regime

In the opposite extreme (high doping), the system is metallic with delocalized electrons ($t \gg U$) and good conductivity. Though, the electron "traffic-jam" [56] of the undoped Mott insulating case is overcome, the electrons still can feel each other and their interactions are not negligible. In this case, electrons are described by Landau's Fermi liquid (FL) theory for metals [68, 69]. This theory treats electrons as *quasiparticles* i.e. "dressed" electrons with enhanced mass m^*. The fundamental idea of the Fermi liquid theory is to describe interacting fermions in the terminology of free fermions propagating in the medium of the remaining electrons. A basic property of a metal which is described by Fermi liquid theory is a quadratic temperature dependence of its resistivity:

$$\rho(T) = \rho_0 + \alpha T^2 \tag{1.8}$$

where ρ_0 and α are constants. Such a temperature dependent resistivity is for example shown in Figure 1.8 c), for overdoped $Tl_2Ba_2CuO_{6+\delta}$ (Tl2201). The T^2-dependence of $\rho(T)$

[4] Since $t_{dd} \gg U_{dd}$ direct hopping between the Cu orbitals which would give $J \sim t_{dd}^2/U$ is suppressed. The effective hopping parameter is defined as $t_{\text{eff}} = t_{pd}^2/\Delta$ where t_{pd} is the charge hopping integral from Cu $3d$ to O $2p$ [65].

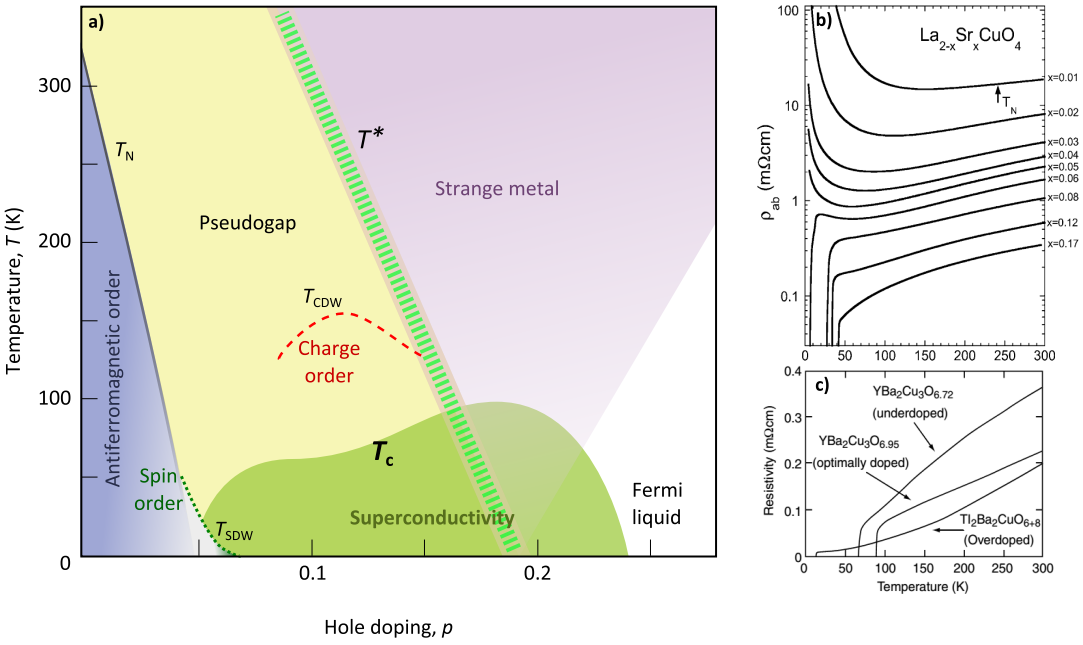

Figure 1.8: Temperature vs. hole doping phases in cuprates. **(a)** Schematic phase diagram of hole-doped copper-oxides. T_{SDW}, T_{CDW} and T_{c} indicate the transition temperature for the the spin-density, charge-ordered and superconducting phase, respectively. T^* denotes the crossover to the pseudogap regime and T_{N}, the Néel temperature, the transition to the antiferromagnetically ordered phase, [56]. **(b)** and **(c)** In-plane resistivity curves for LSCO and YBCO. Adapted from [57, 58].

is often used as a criterion to check for Fermi liquid like behavior in a compound. In highly overdoped, non superconducting cuprates T^2 dependence of the resistivity has been observed in Tl2201[70] and LSCO [71]. The Wiedemann-Franz law, another hallmark of Fermi liquid like behavior, has also been observed in this doping regime [72]. Additionally, it has been found that near E_{F} the bandstructure consists of a single band, with a well defined Fermi surface which forms a large, hole like pocket around the X and Y point [see Fig. 1.9 c)] [73].

Superconducting phase

In the phase diagram, between the Mott-insulating and Fermi-liquid metallic phase, superconductivity is found inside the *superconducting - dome*. On the hole-doped side, superconductivity sets on at $x \approx 5\%$, where x denotes the amount of holes per Cu-atom. The maximum T_{c} is found at the optimal doping at $x \approx 15\%$. So far, the highest T_{c} at ambient pressure is still hosted by the cuprate family $T_{\mathrm{c,max}} \approx 135$ K, achieved over 2 decades ago [15]. Upon further increasing doping, T_{c} is decreasing until SC disappears at $x \approx 28\%$. Cuprate compounds are two-dimensional, layered materials with only small variation of the electronic structure along the k_z-direction. However, the superconducting gap is very anisotropic in the $k_x - k_y$-plane. It has been established by different techniques that it is predominantly of d-wave symmetry:

$$\Delta_{\mathrm{sc}}(\mathbf{k}) = \frac{|\Delta|}{2}[\cos(k_x a) - \cos(k_y a)] \tag{1.9}$$

In determining the gap function, ARPES played a crucial role since it is able to directly probe the momentum resolved magnitude of the gap (absolute value) as plotted in Figure

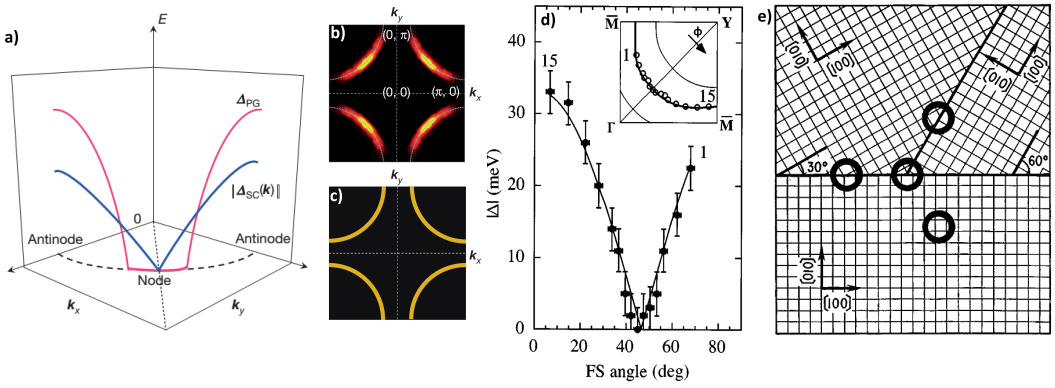

Figure 1.9: Fermi surface, Fermi arcs and SC-order parameter. **(a)** Blue / Red line: Momentum dependence of the absolute value of the superconducting gap and pseudogap, respectively, in the first quadrant of the Brillouin Zone (BZ) [56]. **(b)** Intensity map of the Fermi surface in the pseudogap phase as measured by ARPES. Bright sections mark the Fermi arcs, spectral weight is gapped out in the Antinodal region near the BZ-edge. **(c)** Large Fermi surface as predicted by band theory in the overdoped regime (confirmed by ARPES, quantum oscillations and STM) [56]. **(d)** Amplitude of superconducting gap as a function of Fermi-surface angle ϕ for Bi2212 as measured by ARPES. FS-angle ϕ is indicated in inset [74]. **(e)** Experimental setup of the π-ring experiment. Epitaxially grown superconducting YBCO films which adapt the orientation of the substrate. Center ring is π ring which should show half integer flux quantization for $d_{x^2-y^2}$ pairing symmetry. This experiment succeeded to proof the d-wave pairing symmetry [75].

1.9 d) [74]. However, the ultimate proof for the d-wave symmetry had to be provided by a phase sensitive experiments [see Fig. 1.9 e) and Ref. [75]].

<u>Normal state:</u> Strange Metal - Pseudogap Phase - Charge Order

Strange metal state: It is well established that on the far overdoped side of the phase diagram, the system is well described by Fermi liquid theory [61]. When doping is gradually reduced from the heavily overdoped side, physical quantities start to deviate from Fermi liquid like behavior. For example, in the normal state of optimally doped cuprates ($T > \mathrm{T}_c$), the resistivity is no longer showing T^2-like behavior but increases linearly with temperature [see Fig. 1.8 b) and c)] [62, 76, 77]). The temperature dependence of the resistivity becomes

$$\rho_{\mathrm{ab}}(T) = \rho_0 + \alpha T \tag{1.10}$$

The deviation from FL-like behavior has also been observed in Hall effect and heat transport measurements (Wiedemann-Franz law) [78, 79]. A phenomenological *marginal Fermi liquid* theory has been proposed to account for this *strange-metal behavior* [80].

Pseudogap phase: When doping is further reduced, the system enters a so-called *pseudogap region*. This state is characterized by a gap in the spin response and the charge excitation [81] below a temperature T^* which is monotonously increasing with underdoping. It was first observed as a gap in spin susceptibility in magnetization and nuclear magnetic resonance (NMR) experiments [82, 83]. Later, ARPES directly confirmed the existence of an energy gap (Δ^*) in the electronic excitation spectra which mimics the d-wave character of superconductivity but has so-called *Fermi - arcs* [see Fig. 1.9 a), b)]. Fermi arcs are disconnected portions of the Fermi surface where Δ^* vanishes [84–86]. It has been found that the length of the Fermi arc, i.e. the portion which is gapless, becomes larger with increasing doping [84, 87]. A solid description of the disconnected portion of the Fermi surface and of the overall PG phase is still missing. It is under ongoing debate if the pseudogap phase is a

precursor of the superconducting state with e.g. preformed (fluctuating) pairs but lacking phase coherence or if it is another ordered phase competing with superconductivity. This issue has been debated intensively since the discovery of the pseudogap state in 1989 [56, 81].

Charge-Ordered phase: Since the first discovery of real space ordering of spins and charge into so-called 'stripes' in the $La_{1.6-x}Nd_{0.4}Sr_xCuO_4$ and $La_{2-x}Ba_xCuO_4$ cuprates it has been clear that this state is a phase competing with superconductivity. The stripe-order which is a combination of incommensurate spin order and charge-density wave like ordering was initially revealed by Neutron experiments at $x = 1/8$ where the superconducting dome has a strong dip with reduced T_c [see Fig. 1.8 a)] [88, 89]. The specialty of those compounds is that the low temperature-tetragonal structural phase, which doesn't exist in the other cuprate compounds, locks the stripes in the manner of a pinning potential. Therefore it was believed for a long time that static stripes only appear in these compounds. Only recently it was found that static, short-range incommensurate charge order is a universal phase in all the cuprates [56, 59, 90–92]. However, unlike the stripe phase, no coinciding magnetic order has been observed.

1.8.3 Theories for superconductivity in cuprates

Since the discovery of high-temperature superconductivity in cuprates, several attempts to describe the *pairing mechanism* have been made [93]. However, so far there is no consensus on the proposals and a proper description is still missing [94]. The reason lies in the complexity of the phase diagram since a theory for superconductivity not only has to describe superconductivity itself but also has to give the description for at least the phases in the direct neighborhood of the superconducting dome. Since this work is mainly focused on normal state properties of cuprates, only the most important theories will be briefly discussed. Common to all of them is that they all have their merits and shortcomings. As stated by T. Devereux in Ref. [94], most likely there is no 'silver bullet' that will describe everything, in the sense that there is no single cause for the exceptional high-T_c in the cuprates but SC is caused by the constructive interplay of many "forces".

Spin fluctuations: Motivated by the observation that superconductivity emerges in the vicinity of the antiferromagnetically ordered phase, this approach is based on collective spin fluctuations which are mediating the pairing. The d-wave order parameter, as well as some parts of the phase diagram (e.g. strange metal phase), are reproduced [95, 96].

Resonating valence bond (RVB) approach: Originally proposed by P.W. Anderson in the beginning of the cuprate era, this approach is based on a spin liquid state hosting magnetic singlet pairs. Neighboring spin bonds are fluctuating between a paired state and a non-paired state. The superconducting phase, described with the correct order parameter (d-wave) as well es a pseudogap phase, with preformed pairing but lacking phase coherence, is predicted. The RVB-approach could also describe the strange-metal phase and other features of the phase diagram [97, 98].

Loop currents and other competing orders: In 1997, Ch.Varma proposed a model of the occurrence of spontaneous loop currents in the two dimensional O-Cu-O plaquettes which describes the pseudogap (PG) phase as a competing order to superconductivity. The proposed quantum critical point of the PG-phase inside the SC-dome triggers scale-invariant quantum fluctuations which mediate superconductivity and also lead to other anomalous normal state properties (strange metal) [99, 100]. Other 'hidden order' competing scenarios include the d-density wave [101] or nematic order [102, 103].

Other theoretical approaches to account for superconductivity in cuprates are for example the formation of stripes [104] or theories which are based on strong electron-phonon coupling (polarons) [25, 105, 106].

1.9 Iron-based superconductors

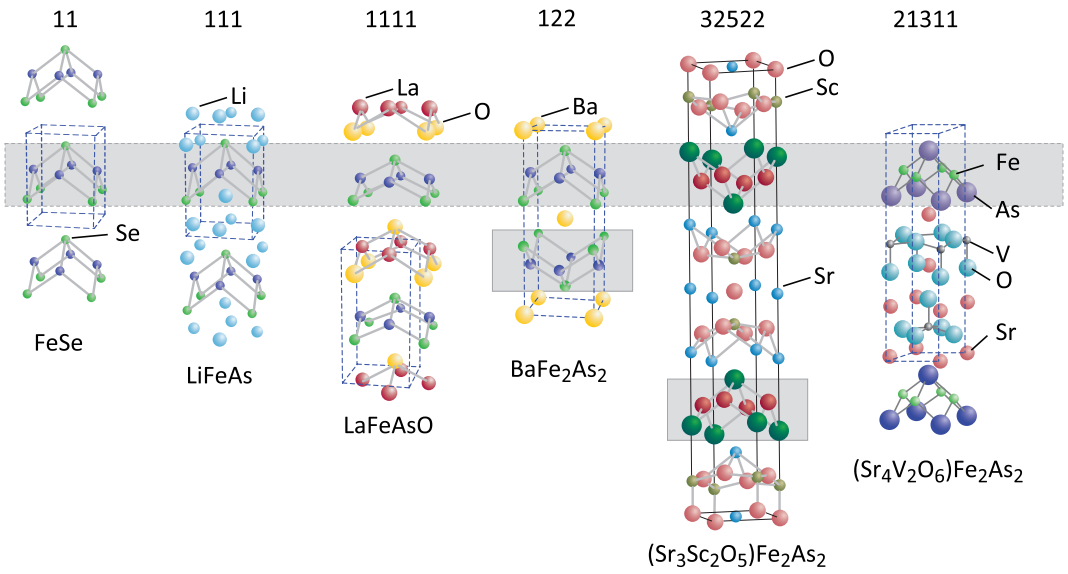

Figure 1.10: Representative crystal structures of different iron-pnictide families. Grey area indicates the common FePn respectively FeCh layer. Adapted from [107].

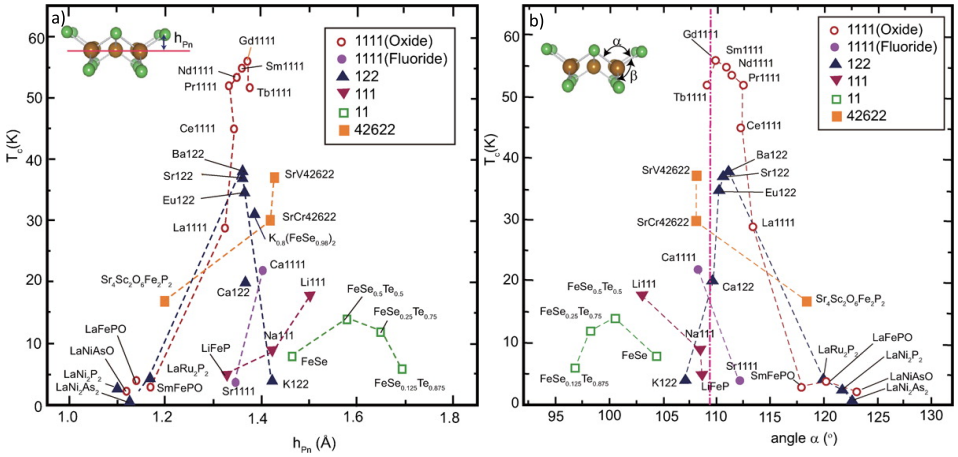

Figure 1.11: **(a)** Plot of T_c vs pnictogen height h_{Pn} as indicated in inset. Highest T_c values are found around $h_{Pn} \sim 1.4$ Å. **(b)** A positive correlation of pnictogen angle and T_c for several material types is observed. Highest T_c is found for $\alpha \approx 109.5°$ which corresponds to a regular tetrahedron. Adapted from [108].

Immediately after the discovery of high-T_c superconductivity in a material containing magnetic iron, a lot of research activities in the field of superconductivity has been dedicated to iron-based superconductors (IBSC) [34, 107, 109–111]. After the initial discovery that fluorine doped LaFeAsO can have a maximum T_c of 26 K [4], the maximum transition temperature was quickly pushed to 55 K in related quaternary compounds ($ReFeAsO_{1-\delta}$, Re = rare earth metal) [112]. Rapidly, other families with different chemical composition and crystal structure have been synthesized. The quaternary pnictides, also known as '1111' family are difficult to synthesize (by high pressure synthesis) and only small single crystals

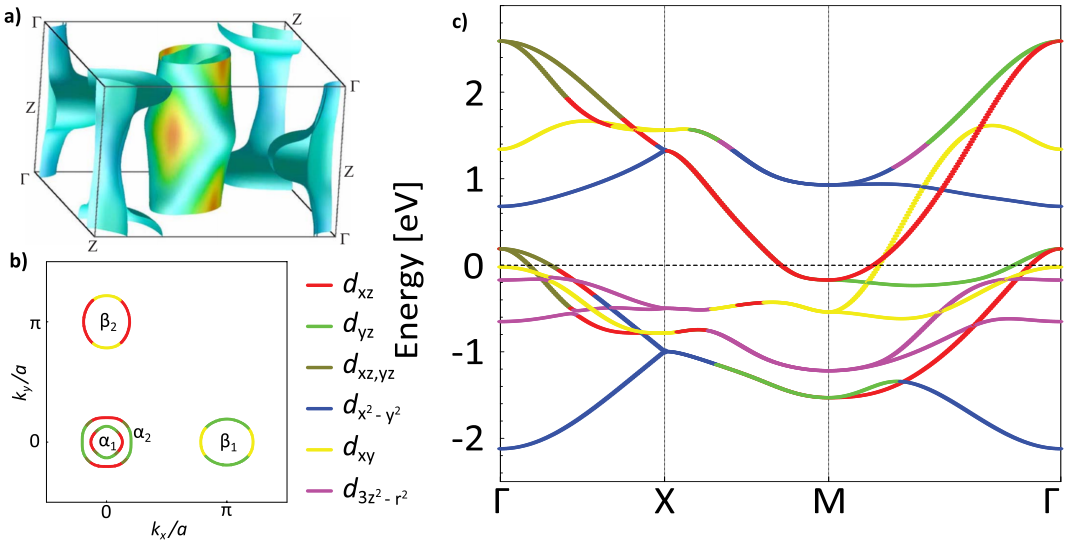

Figure 1.12: Calculated electronic structure of the 122 iron-pnictide family. Adapted from [114, 115].

have been available. However, other, slightly different structures like the $AeFe_2As_2$ (Ae = Ba, Sr), known as '122' structure or the '111' family, AFeAs (A = Li, Na) have been synthesized soon and relatively large single crystals could be obtained. Since then, many other compositions have been found. A complete overview about all families which have been discovered up to date and related compounds which have been synthesized but which are not superconducting has been collected in an extensive review by H. Hosono [113]. Here, the discussion is limited on some of the most commonly investigated iron-based superconductors [Fig. 1.10]. Common to all the iron-based superconductors is the single iron-pnictide (FePn; Pn=As, P) or iron-chalcogenide (FeCh; Ch=Se, Te) layer. Compared to cuprate superconductors, it slightly differs from the CuO layer in the aspect that the ligand Pn/Ch atom doesn't lie in the Fe layer but is alternatively above or below the Fe plane. The distance between Pn/Ch - atom and the Fe layer is defined as h_{Pn} which varies for different families and also within a family upon chemical substitution of atoms. As presented in Figure 1.11 a), a positive correlation is found for the T_{c} of a certain compound and its h_{Pn}. The fact that there is a optimal h_{Pn} for which maximum T_{c} values can be found sets a necessary condition for maximizing T_{c}. A similar relation is also observed between T_{c} and the Pn-Fe-Pn bond angle α [see Fig. 1.11 b)] which is found to give highest T_{c} for $\alpha = 109.47°$ which corresponds to a regular tetrahedron. Although both the optimal h_{Pn}-rule and the regular tetrahedron rule have been used as a guideline for crystal synthesis, their physical meaning is not fully understood [108]. Another difference between the iron-based superconductors and the cuprates is that the FePn (FeCh) layer is always sandwiched by a spacer material. There are no double or triple layer compounds[5].
Very important for technological applications is that the IBSC-crystals are not brittle ceramics but metals which are more robust and flexible.

1.9.1 Electronic structure

With simple valence counting, for the representative '122' case ($BaFe_2As_2$), one finds that the Ba is in the 2+ and As in 3- configuration, giving a 2+ ionic state for Fe. Two electrons of the Fe atom are removed from the 4*s* shell. The remaining 6 valence electrons fill the Fe

[5]Of course this is not valid for the 11 families.

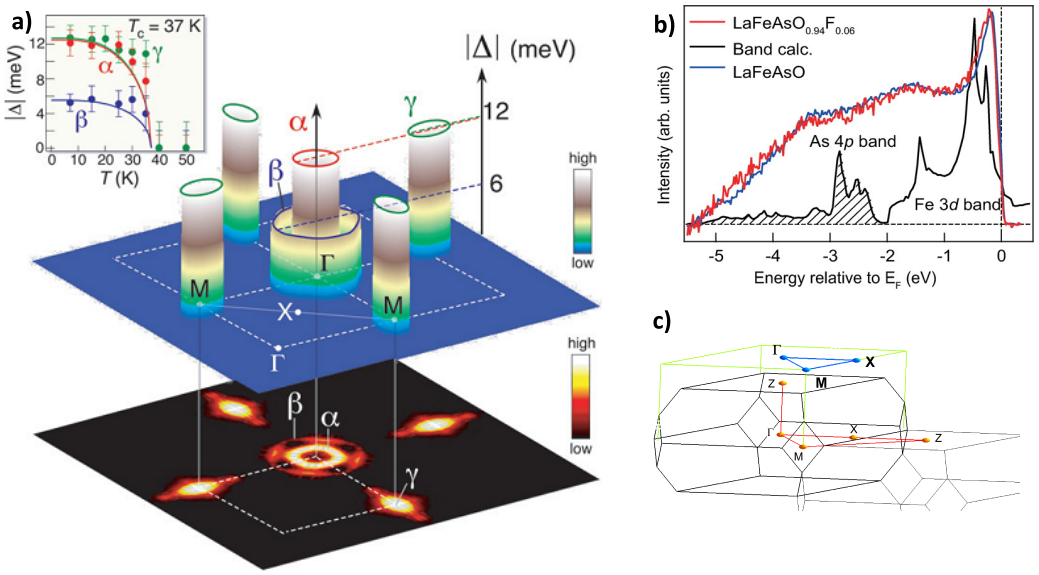

Figure 1.13: Electronic structure of the 122 and 1111 iron-pnictide family as measured by ARPES. Adapted from [108, 116].

d shell and are equally distributed over the 5d orbitals due to a relatively small crystal field splitting which results in strong hybridization of all d orbitals [117, 118]. As predicted by calculations, states from the iron orbitals dominate the DOS around E_F and the spacer layer respectively the pnictogen (chalcogen) atoms have only minor contribution [see Fig. 1.13 b)]. Figure 1.12 a) shows the Fermi surface (FS) in 3D momentum space of the prototypical '122' $BaFe_2As_2$ (Ba122) parent compound, calculated by using density functional theory (DFT)[6]. The calculated bandstructure along high symmetry lines (indicated by blue lines in Figure 1.13 c) is plotted in Figure 1.12 c) which demonstrates the hybridization of the different Fe 3d orbitals. It can be seen from the color-coded plot of the bands that all the five orbitals are contributing to the bands close to E_F. However, for Ba122 only the bands derived from d_{xz}, d_{yz} and d_{xy} orbitals cross the Fermi level and form the Fermi surface. The FS consists of 2 hole-like bands around $\Gamma = (0,0)\frac{1}{a}$ and one electron-like band around $(\pi,0)\frac{1}{a}$ and one around $(0,\pi)\frac{1}{a}$ [7]. The FS is shown in the unfolded BZ of the 1 Fe-unit cell [Fig. 1.12 b)] with color-coded contribution of the individual orbitals. The FS of optimally doped $Ba_{1-x}K_xFeAs_2$ obtained from ARPES measurement is illustrated in Fig. 1.13 a), lower panel.

Although IBSCs are metallic they are known to be poor conductors with large resistivity close to the Mott-Ioffe-Regel limit [120, 121]. It has been found that electronic correlations are relatively strong in IBSCs resulting in an overall electron-mass enhanced of $m^*/m \approx 2-4$ [122–124]. In terms of electronic bandstructure, enhanced electron-electron correlations are directly connected to a band width renormalization which can be determined in a direct

[6] The FS in Fig. 1.12 a) is plotted in the projected Brillouin zone as shown in Figure 1.13 c). Usually the electronic bandstructure and Fermi surface [Fig. 1.12 a), c)] is presented in the BZ of the folded 2 Fe unit cell (uc) as shown in Figure 1.13 c) for the 122 family, which is the correct primitive structural cell in the paramagnetic phase. However, theoretical studies often work with the unfolded 1 Fe unit cell since they neglect that there exist two inequivalent Fe site due to alternating positions of the As ligands above and below the Fe plane [see FS in Figure 1.12 b)]. Implications of the 2 Fe unit cell on the electronic structure and ARPES results are discussed by V. Brouet *et al.* [119]. If not mentioned differently, during this report, always the primitive unit cell (with 2 Fe per uc) will be used. Due to the negligible k_z dependence of the electronic structure of many of the iron-pnictides, the projected (tetragonal) BZ [green lines in Fig. 1.13 c)] is often used in the data presentation.

[7] In the notation of the unfolded BZ (2 Fe unit cell).

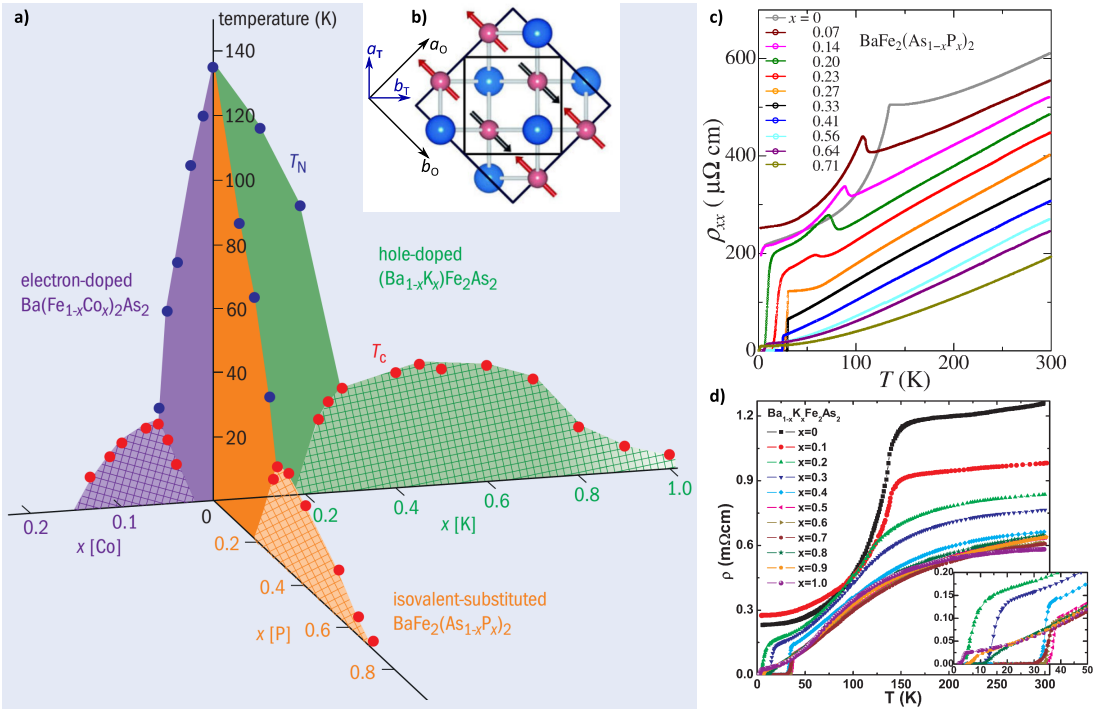

Figure 1.14: **(a)** Temperature vs. chemical substitution phase diagram for Ba122. Superconductivity occurs for either doping electrons ($Ba(Fe_{1-x}Co_x)_2As_2$), doping holes ($Ba_{1-x}K_xFeAs_2$) or chemical substitution of isovalent elements ($BaFe_2(As_{1-x}P_x)_2$). Adapted from [129]. **(b)** In-plane magnetic spin arrangement (arrows on the Fe-site) for 122 and 1111 compounds. Large black square denotes the orthorhombic (AFM) unit cell while small black square represents the tetragonal (PM) unit cell. Adapted from [108]. **(c)** In-plane resistivity for $BaFe_2(As_{1-x}P_x)_2$. Note the doping range in which the normal-state resistivity shows almost perfectly linear behavior. Adapted from [130]. **(d)** In-plane resistivity for $Ba_{1-x}K_xFeAs_2$. Inset shows zoom-in at low temperatures. Adapted from [131].

comparison between the measurement and a calculation which doesn't include correlations (e.g. DFT) [125]. Due to the multi-orbital nature of the IBSCs Hund's exchange coupling (J_H) plays a crucial role for electronic correlations [118, 126, 127]. The non-negligible average interaction parameters were found to be $U = 3 - 5$ eV and $J_H = 0.4 - 0.5$ eV from constrained-RPA calculations, where U denotes the Hubbard U for on-site correlations [128].

1.9.2 Phase diagram of iron-based superconductors

Due to the high number of different families it will be difficult to descripe the phase diagram of every family in detail. However, there are some features which are shared by a large number of different families and will be discussed on the prototypical example of Ba122. Figure 1.14 shows the temperature vs. chemical substitution phase diagram for Ba122. Similar to cuprate superconductors, superconductivity in iron-based compounds emerges upon doping electrons or holes to the parent compound[8]. However, in IBSC superconductivity can also be induced by applying external pressure (hydrostatic or uniaxial) [132, 133] or chemical pressure by chemical substitution of isovalent elements.

[8]The 111 materials (LiFeAs and NaFeAs) are already superconducting for $x = 0$

Antiferromagnetic, orthorhombic phase

Below the Néel temperature ($T_N \sim 150$ K for Ba122), the parent compound of iron-based superconductors develops long-range antiferromagnetic (AFM) order, similar to many other classes of unconventional superconductors[9]. For 1111, 111 and 122 compounds, spins are ferromagnetically arranged along a_O-direction and AFT-ordered along b_O [see Fig. 1.14 b)]. The magnetic ordering occurs at a temperature lower than the structural transition (T_S) from the high-temperature tetragonal phase to a low temperature orthorhombic phase where the lattice constant along a_O slightly shrinks. With increasing doping, T_S and T_N are simultaneously and gradually suppressed until they vanish. In the case of 122 compounds T_S and T_N vanish at a doping value which is close to optimal doping[10]. For some compounds (e.g. 122, 111), a coexistence of AFM and SC is found in an intermediate range [Fig. 1.14 c), d)]. Below T_N (T_S) the resistivity is suppressed (has a kink), and at T_c it drops rapidly to zero (see, for example red or green curve in Figure 1.14 c). The microscopic nature of the magnetism is still under debate [109, 110]. The first proposal is an itinerant picture in which Fermi surface nesting between the hole pocket around Γ and the electron pockets around M leads to a Lindhard-type spin density wave (SDW) state [116, 134]. The second proposal is a localized picture which sets the iron-pnictides close to a Mott insulating transition where AFM arises due to electron exchange interaction [121, 135]. An extensive introduction of magnetism can be found in refs. [136–138].

Superconducting phase

Unlike cuprate superconductors, IBSCs are multiband systems. Therefore the search for the correct symmetry of the order-parameter is more involved and requires more precise measurements. ARPES measurements, which were among the first experiments to determine the symmetry of the order parameter (OP), point towards a nodeless, symmetric OP [see Fig. 1.13 a)] [116]), which is consistent with early theoretical predictions that the OP has a s-wave form but with sign change between the different FS sheets [139, 140]. The, so-called $s^{\pm}$order parameter is given by:

$$\Delta_{s\pm}(\mathbf{k}) = \Delta_0 \cos(k_x a)\cos(k_y a) \tag{1.11}$$

However, to experimentally determine the sign of the OP and rule out other possibilities like s^{++} or $d_{x^2-y^2}$ turned out to be very complex. Strong support for the $s^{\pm}$scenario comes from inelastic neutron scattering which shows a magnetic resonance at a wave vector $Q = (\pi, \pi)$. Researchers assign this resonance to a certain type of spin excitation. Since Q is spanning the distance between the hole and electron pockets the resonance can only exist when the gap changes its sign between the pockets [141–143]. Other indications for $s^{\pm}$ come from quasiparticle interference [144] as well as other kind of phase sensitive experiments [40].

1.9.3 Theories for superconductivity in IBSC

For the microscopic mechanism of the superconductivity, there exist several scenarios. It is widely believed that magnetic fluctuations play a crucial role and are involved either directly or indirectly in the formation of the Cooper pairs [34].
A widely discussed scenario is the itinerant electron picture in which fermionic states situated close to the Fermi level interact via Coulomb interaction leading to Stoner-type magnetic ordering and also superconductivity [145].
Another scenario is based on the local electron picture which, in essence is based on the Mott-Hubbard model in the strong coupling limit and is treated in the formalism of the

[9] LiFeAs is an exception and has no magnetic ordering.
[10] Optimal doping refers to the doping value where the highest superconducting transition temperature is found.

Table 1.1: Transition temperature and low temperature values of the energy gap, the coherence length, the London penetration depth and the upper critical field. To date, numbers in literature vary strongly and thus are only rough guides. For Pb and Nb, the critical field B_c rather than B_{c2} is quoted. (ab) and (c), refer to in-plane and out-of-plane properties, respectively; max. indicates the maximum energy gap. Adapted from [20].

Material	T_c **(K)**	Δ **(meV)**	ξ_{GL} **(nm)**	λ_L **(nm)**	B_c, B_{c2} **(T)**
Pb	7.2	1.38	51-83	32-39	0.08 (B_c)
Nb	9.2	1.45	40	32-44	0.2 (B_c)
$YBa_2Cu_3O_{7-\delta}$	92	15-25 (max)	1.6 (ab)	150 (ab)	240 (ab)
			0.3 (c)	800 (c)	110 (c)
$Bi_2Sr_2CaCu_2O_{8+\delta}$	94	15-25 (max)	2 (ab)	200-300 (ab)	> 60 (ab)
			0.1 (c)	> 15000(c)	> 250 (c)
$Ba_{0.6}K_{0.4}Fe_2As_2$	38	4-12	1.5 (ab)	190 (ab)	$70 - 235$ (ab)
			> 5 (c)	0.9 (c)	$100 - 140$ (c)
$NdO_{0.82}F_{0.18}FeAs$	50	(37)	3.7 (ab)	190 (ab)	$62 - 70$ (ab)
			0.9 (c)	> 6000(c)	300 (c)

$t - J$ model [121, 135, 146].
An approach which is less often discussed in literature is based on the strong polarizability of the large anions (As^{3-}) resulting in strong charge fluctuations on the Fe ions. As a consequence Coulomb repulsion on the iron site is effectively reduced, which could open a pairing channel for the Fe d electrons [147, 148].

1.10 Energy, temperature and length scales in high-T_c superconductors

Besides the order parameter and T_c, which surely belong to the most important parameters of superconducting compounds, there are more variables which are also essential for fully characterizing a superconductor. Different kinds of superconductors not only could differ in terms of pairing mechanism but also in the different length and energy scales.

When the system enters the superconducting state, electrons form pairs and condense into a BEC. The number of particles (n_S) which contribute to the condensation is related to the London penetration depth in the London equations [22, 149]:

$$\lambda_L = \sqrt{\frac{m^* c^2}{4\pi e^2 n_s}} \tag{1.12}$$

where m^* is the electron effective mass and e the charge of the electron. λ_L describes the distance of a penetrating external magnetic field B_{ext} until it decayed to a magnitude B_{ext}/e. For cuprates and IBSCs, it was found that the penetration depth is roughly one order of magnitude larger than in conventional superconductors [see Table 1.1] [149].
The second characteristic length scale which is often used to classify superconductors is the Ginzburg Landau coherence length $\xi(T)$. It defines the length scale over which the wave function $\psi(\mathbf{r})$ can vary without excessive energy increase. Considering vertices, on this length scale the Cooper-pair density vanishes around a vertex axis [20, 23, 24][11]. It

[11] Sometimes, ξ is also called the stiffness of ψ.

has been shown experimentally that $\xi(T)$ in high-T_c superconductors can differ from that in conventional superconductors by one order of magnitude. The ratio between the two mentioned length scales, λ and ξ gives the Ginzburg-Landau parameter: $\kappa = \lambda/\xi_{GL}$ which defines if the superconductor is of *type I* ($\kappa < 1/\sqrt{2}$) or of *type II* ($\kappa > 1/\sqrt{2}$). In a type I superconductor external magnetic field B_{ext} is fully expelled for B_{ext} below a critical field B_c. Above B_c, the external field destroys superconductivity. For a type II superconductor B_{ext} is fully expelled for $B_{ext} < B_{c1}$ and SC destroyed for $B_{ext} > B_{c2} > B_{c1}$. For $B_{c1} < B_{ext} < B_{c2}$ the system is in the Shubnikov phase and quantized magnetic flux lines, called *vortices* (with elementary flux quanta $\phi = h/2e$) penetrate through the superconductor [150]. The values presented in table 1.1 show clearly that the HTSCs are type II SCs with extreme κ values. In conventional superconductors, the superconducting energy gap has a constant amplitude in k-space and is connected to the critical temperature via the following relation $\Delta = 3.52 k_B T_c$. For the HTSCs the OP is not constant and it is not clear if such a relation holds or not. In cuprates, with the pseudogap Δ^* and a gap along the zone diagonal in very underdoped cuprates [151] there exist other energy scales for which it is not yet clear whether and how they are connected to superconductivity. Other energy scales in the HTSCs which are describing electronic interactions are the Hubbard U and the superexchange interaction J for the cuprates and the Hubbard U, magnetic exchange J and Hund's coupling J_H for IBSCs [127, 152].

1.11 Density functional theory (DFT) calculations

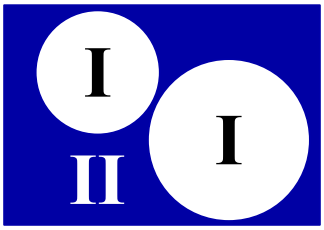

Figure 1.15: Partition of the real space into (I) atomic spheres around the atoms and (II) interstitial regions. Adapted from [153].

Since the middle of the 20th century calculations based on density functional theory (DFT) became an increasingly and widely employed tool to calculate electronic properties in the field of condensed matter and quantum chemistry research. It has been successfully applied to calculate binding energies of molecules and the DOS, bandstructure and other properties of solids. To calculate the electronic properties, the many-particle problem (equation 1.1) for solids ($N \sim 10^{23}$) has to be solved. As already discussed in the beginning of this chapter, so far it has been an impossible task to find an exact solution of this equation. To solve the problem, several approximations have to be made.

In DFT the electrons are assumed to be "the principal actors". The nuclei are much heavier and therefore considered as static, with no kinetic energy[12]. Their only purpose is to provide the (Coulomb-)potential landscape $V_{ext} = H_{el-ion}$. The DFT formalism assumes that this landscape will be the main thing which differs for every system and the rest will, in principle, not change. The Hamiltonian can then be written as

$$H = T + U + V_{ext} \tag{1.13}$$

where $T = T_{el}$ (electron kinetic energy) and $U = V_{el-el}$ (electron-electron interaction) are independent of the particular solid and "universal" for every N-electron body.

[12]This approximation is commonly known as Born-Oppenheimer approximation.

With the theorems of Hohenberg and Kohn [154] this equation became solvable. In those theorems, the ground-state density $\rho(\mathbf{r})$ is the key variable which, once it is known, implies knowledge of the wave function and therefore knowledge of the potential.

$$\rho(\mathbf{r}) \Rightarrow \Psi(\mathbf{r}_1,...,\mathbf{r}_N) \Rightarrow V_{\text{ext}} = V_{\text{ext}}(\mathbf{r}) \tag{1.14}$$

The total energy functional which has to be minimized in order to solve the problem is of the form:

$$E_V[\rho] = \langle\Psi|T+U|\Psi\rangle + \int d^3r\, \rho(\mathbf{r})V_{\text{ext}}(\mathbf{r}) \tag{1.15}$$

This functional has its global minimum at the groundstate density which corresponds to the ground state potential [6, 154, 155]. However, it still contains the complications of the many particle problem 1.1.

Kohn and Sham transformed this functional in such a way that it is reduced to a energy functional for a *non-interacting* classical electron gas living in two external potentials, the one produced by the nuclei V_{ext} and one which stems from electron-exchange and electron-correlation effects V_{xc}[156]. The $T = T_0 + V_c$ and $U = V_H + V_x$ are split into an non-interacting and an interacting part which gives the Kohn-Sham (KS) equation:

$$[T_0 + V_{\text{H}} + V_{\text{xc}} + V_{\text{ext}}]\phi_i(\mathbf{r}) = \epsilon_i\phi_i(\mathbf{r}) \tag{1.16}$$

where $V_{\text{xc}} = V_{\text{x}} + V_{\text{c}}$ is the exchange interaction and $V_{\text{H}} = \frac{e^2}{4\pi\epsilon_0}\int dr' \frac{\rho(\mathbf{r}')}{|\mathbf{r}-\mathbf{r}'|}$ is the (non-interacting) Hartree term[13]. The strong assumption of this approach is that the exchange interaction can be written as a local exchange potential. The solution of equation 1.16 will provide the wave functions $\phi_i(\mathbf{r})$ which, in turn, determine the potentials. Thus the KS equation can be solved self-consistently [6, 153].

In modern computer codes, in order to increase accuracy, gradient terms have been added to the exchange-correlation potentials, which are captured in the generalized gradient approximation (GGA). It is obvious that the computational task (to solve the KS equation) can be highly simplified if the basis set for the orbitals is chosen in a smart way. A widely employed method is to subdivide the space according to Figure 1.15 into atomic spheres (I) and interstitial space (II). In the atomic spheres, a combination of spherical harmonics and radial functions is used as a basis and in (II) a plane wave expansion is used. In modern codes, more sophisticated versions of basis functions have been introduced as well as more accurate ways to treat electronic correlations and relativistic effects. These are discussed in many books (e.g. [157, 158]) but will go beyond the scope of this work.
The ARPES data presented in this work is often compared to results from DFT-calculations, which have been mainly calculated by using the wien2k package [159].

[13]Note that the single particle wave functions $\phi_i(\mathbf{r})$ are not the wave functions of the electrons, however they are providing the correct density $\rho(\mathbf{r}) = \sum_i \phi_i^*(\mathbf{r})\phi_i(\mathbf{r})$.

Chapter 2

Photoemission spectroscopy - theory and application

2.1 Introduction

As an integral part of any solid, electrons and their properties have to be well understood in order to explain the physics of a certain compound. Energy, momentum and spin are basic physical quantities which lie at the heart of any theoretical description and therefore are desired to be known in great detail. Angle-resolved photoemission spectroscopy (ARPES) is a technique which is able to directly access those quantities[1] with tremendously improved precision, during the past decades. This uniqueness has boosted ARPES to be one of the most powerful and widely used experimental tools in the field of condensed matter physics in the past century.

Photoemission (PE) spectroscopy experiments are based on the photoelectric effect; the emission of electrons from a material under radiation of light with sufficient energy. The photoelectric effect was discovered by Heinrich Hertz in 1887 and was described by Albert Einstein in 1905 by the postulation of light quanta[2] with energy $h\nu$. Einstein's theory was experimentally proven by Millikan in 1914 when he demonstrated that the kinetic energy E_{kin} of the emitted electron scales with the frequency of the photon ν: $E_{kin} = h\nu - \phi$ where ϕ denotes the *work function* of the irradiated material.
Several decades after its discovery and after important technical developments such as photon sources, electron analyzers and the ultra high vacuum (UHV) technique, photoelectron spectroscopy experienced its breakthrough in the 1960's as a probe for electronic structure in physics and chemistry [160–162]. By applying the energy conservation law

$$E_{\mathrm{kin}} = h\nu - \phi - E_{\mathrm{B}} \tag{2.1}$$

the electronic density of states $n(E)$ could be measured as a function of the electron binding energy E_{B}. In 1970 after O.E. Kane suggested to use also the momentum of the outgoing electron [163], the first experiments have been conducted in angle-resolved mode and a full mapping of the momentum resolved electronic bandstructure became possible [164, 165].

Since the discovery of high temperature superconductivity in layered copper-oxide compounds (cuprates) ARPES became a heavily employed, standard tool to map out the electronic band structure in great detail [3]. For example, ARPES contributed essentially to establish many characteristic energy scales in cuprate superconductors: The momentum dependence of the gaps in the single particle spectral function which are present in the system (superconducting gap, pseudogap, charge-ordering gap....) [74, 151, 166, 167], exploration

[1] The results presented in this work are focused on energy and momentum resolved but spin integrated photoemission.

[2] Nowadays, these quanta are called photons.

of kinks in the bandstructure [168, 169], discovery of Fermi arcs and studies of the Fermi surface topology [170, 171][3]. The discovery of high-T_c superconductivity in iron-pnictide compounds has further stimulated the ARPES community and triggered another boost of ARPES experiments. The substantial improvement of energy and momentum resolution of ARPES instruments provided the basis for resolving the different Fermi surface sheets, its multi-orbital nature and the Fermi surface dependent superconducting gap structure. [110, 116, 123, 172]. Recently ARPES is also heavily employed as a main tool in the research of topological insulators, Dirac and Weyl-semimetals and related compounds [173–175].

The results presented in this work will be concentrated on high energy- and momentum resolved, spin integrated ARPES (HR-ARPES) for photon energies in the ultraviolet as well as in the soft X-ray range (UV-ARPES respectively SX-ARPES). Since the iron-pnictide and copper-oxide compounds which are discussed in this work host a spin-degenerate bandstructure a investigation in terms of spin-resolved photoemission spectroscopy is not required.

2.2 Theory

2.2.1 Introduction

The quantum mechanical rigorous description of the photoemission process is given in the so called *one-step* model which treats the whole process starting from photo excitation of the electron until detection with a single quantum mechanical propagation operator. However, the many body ($\mathcal{O}(23)$) problem in this model cannot be solved analytically and its theoretical treatment would go beyond the scope of the introduction presented here. A simplified model which is widely used in the ARPES community is provided by the *three - step model*.

2.2.2 Three - step model

Under certain approximations the PE process can be split into three successive steps which deliver a reasonable qualitative description of the underlying physics. The different steps of the so called *three-step model* as illustrated in Figure 2.1 and Figure 2.3 [44, 176] are:

1. Absorption of photon and optical excitation of an electron in the bulk,
2. Transport of the electron to the surface,
3. Escape of the electron into the vacuum and detection by the electron-analyzer.

First Step - Optical excitation

The interaction of an external electromagnetic field with an electronic system containing N electrons will excite the system from its ground state (initial state) Ψ_i^N to a final state Ψ_f^N. If the interaction is weak (low intensities of the external field) in first order perturbation theory, the transition probability is described by Fermi's golden rule:

$$w_{fi} = \frac{2\pi}{\hbar}|\langle\Psi_f^N|V_{\mathrm{ep}}|\Psi_i^N\rangle|^2\delta(E_f - E_i - h\nu) \tag{2.2}$$

where E_f and E_i are the initial and final-state energies of the N-particle system. The electron-photon interaction potential V_{ep} is given by

$$V_{\mathrm{ep}} = -\frac{e}{2m_e c}\left[\mathbf{p}\cdot\mathbf{A}(\mathbf{r}) + \mathbf{A}(\mathbf{r})\cdot\mathbf{p}\right] + \frac{e^2}{2m_e c^2}|\mathbf{A}(\mathbf{r})|^2 \tag{2.3}$$

[3] For a review of ARPES on cuprate superconductors, see [44, 48]

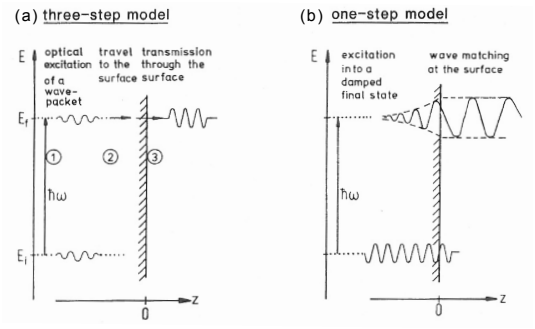

Figure 2.1: **(a)**: Schematic of the three-step model: (1) Excitation of the electron by the photon. (2) travel of the electron to the surface (3) transmission through the surface into the vacuum. **(b)**: One-step model: A bloch wave electron is excited and described as a free wave in vacuum which is damped inside the solid. Adapted from [176].

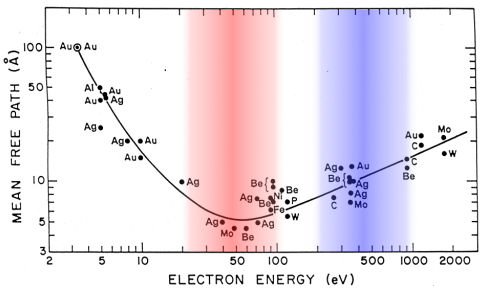

Figure 2.2: Universal curve of the photoelectron escape depth for various materials. The red/blue shaded region is representing the photon energy range of the SIS respectively ADRESS beamline at PSI. Adapted from [177].

where $\mathbf{A}$ denotes the electromagnetic vector potential of the external electromagnetic field and $\mathbf{p} = -i\hbar\boldsymbol{\nabla}$ is the electronic momentum operator. The variables e, m_e, c denote the charge of the electron, its mass and the speed of light. In first order approximation, the second term $|\mathbf{A}(\mathbf{r})|^2$ can be neglected. Note, the first order approximation is only valid for a relatively low incoming photon flux.
Because the gauge is not fixed in electrodynamics the Coulomb gauge ($\boldsymbol{\nabla} \cdot \mathbf{A} = 0$) can be chosen to give a vanishing commutator relation[4] $[\mathbf{p}, \mathbf{A}(\mathbf{r})] = \mathbf{A}(\mathbf{r})\cdot\mathbf{p} - \mathbf{p}\cdot\mathbf{A}(\mathbf{r}) = i\hbar\boldsymbol{\nabla}\cdot\mathbf{A} = 0$. Consequently, the electron-photon potential V_{ep} transforms into:

$$V_{\text{ep}} = \frac{e}{m_e c}\mathbf{A}\cdot\mathbf{p}. \tag{2.4}$$

In a material with weak electronic correlation the photoemission process in the N-particle wave function, Ψ^N, can be treated within the so called *sudden approximation* limit i.e. the excitation of the electron is instantaneous and the interaction of the excited electron and the $N-1$ electrons is negligibly weak. This assumption is justified for photon energies of 10 eV and above [180]. Under this consideration the final-state wave function can be expressed as

$$\Psi_f^N = c_{\mathbf{k}}^{\dagger}|\Psi_f^{N-1} \tag{2.5}$$

with $c_{\mathbf{k}^\dagger}$ being the creation operator for the photoelectron ϕ_f. Ψ_α can then be written as $\Psi_\alpha^N = \mathcal{A}\phi_\alpha^{\mathbf{k}}\Psi_\alpha^{N-1}$, $(\alpha = i, f)$ with $\mathcal{A}$ denoting the fermionic anti-symmetrization operator which ensures that Ψ_α^N complies with the Pauli exclusion principle and ϕ_α denoting the wavefunction of the photoelectron. The $N-1$ particle wave function Ψ_f^{N-1} is, rigorously speaking, not an eigenstate of the $N-1$ particle Hamiltonian, but can be written as a superposition of eigenstates with eigenenergy E_m^{N-1}. Using eq. 2.5, the matrix element in equation 2.2 can be transformed into:

$$\langle\Psi_f^N|V_{\text{ep}}|\Psi_i^N\rangle = \langle\phi_f^{\mathbf{k}}|V_{\text{ep}}|\phi_i^{\mathbf{k}}\rangle\langle\Psi_f^{N-1}|\Psi_i^{N-1}\rangle \tag{2.6}$$

where $M_{f,i}^{\mathbf{k}} = \langle\phi_f^{\mathbf{k}}|V_{\text{ep}}|\phi_i^{\mathbf{k}}\rangle$ is the one-particle dipole matrix element which plays an important role in ARPES experiments. The kinetic energy of the photoexcited electron in the solid is

[4]Sometimes $\boldsymbol{\nabla}\cdot\mathbf{A} = 0$ is also discussed within the *dipole approximation* which assumes a small variation of the external field compared to atomic distances in the UV-regime [179].

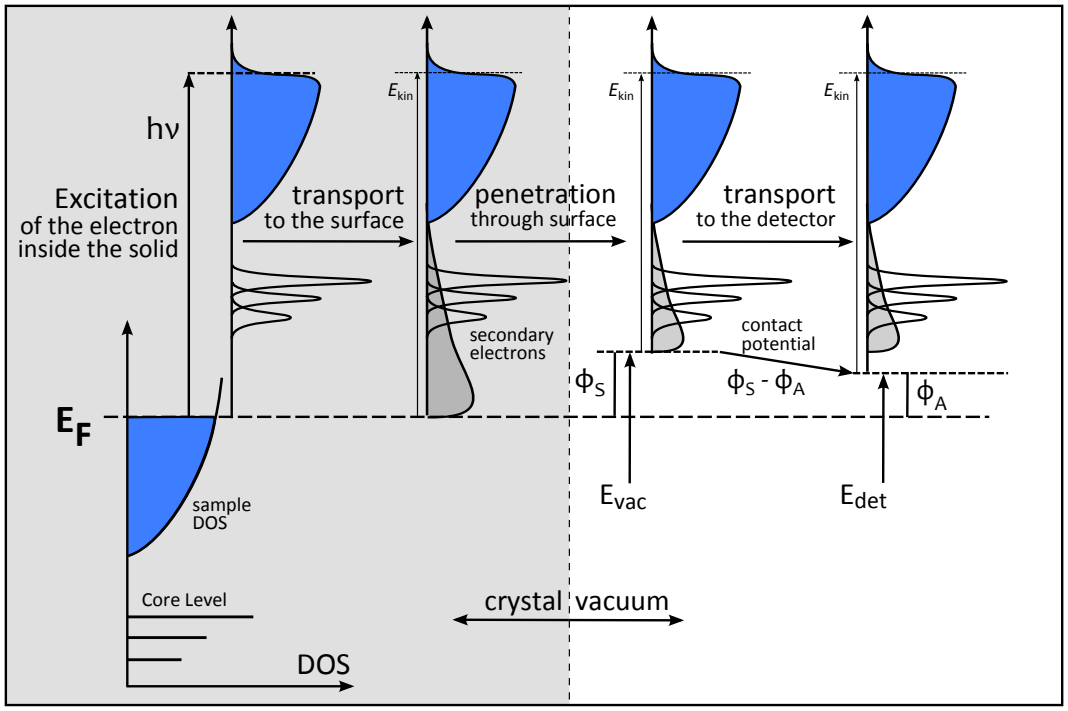

Figure 2.3: Schematic energy diagram of the three step model, describing the photoemission process. The three model describes the photoexcitation of the electron, the transport to the sample surface and the penetration through the surface. After penetration, the electrons travel, without interaction, to the detector. Adapted from [176, 178].

given by $E_{\text{kin}} = E_f^N - E_f^{N-1}$ and with $|\Psi_i^{N-1}\rangle = c_{\mathbf{k}}|\Psi_i^N\rangle$ the total photoemission intensity is then given by the summation over all initial and final states:

$$I(\mathbf{k}, h\nu) = \frac{2\pi}{\hbar} \sum_{f,i} |M_{i,f}^{\mathbf{k}}|^2 \sum_m |\langle \Psi_m^{N-1} | c_{\mathbf{k}} | \Psi_i^N \rangle|^2 \delta(E_{\text{kin}} + E_m^{N-1} - E_i^N - h\nu) \quad (2.7)$$

$$= \sum_{i,f} |M_{f,i}^{\mathbf{k}}|^2 \, A^-(\mathbf{k}, \omega) \quad (2.8)$$

Here, $A^-(\mathbf{k}, \omega)$ and $\omega = E_{\text{kin}} - h\nu - \mu$ denote the electron removal *spectral function* and the energy of the electron in the solid. The chemical potential $\mu = E_0^N - E_0^{N-1}$ is defined as the energy difference of the ground states of the N-particle system and the $(N-1)$ particle system. The electron removal spectral function can be considered as the probability of removing an electron with energy ω and momentum $\mathbf{k}$ from the N-electron system $|\Psi_i^N\rangle$. Analogously, in the inverse photoemission process, the electron addition spectral function $A^+(\mathbf{k}, \omega)$ can be considered as the probability for adding an electron to the system. The *one-particle spectral function* is the sum of both: $A(\mathbf{k}, \omega) = A^-(\mathbf{k}, \omega) + A^+(\mathbf{k}, \omega)$. The one-particle spectral function provides an indication how well such an excitation is described by a non-interacting particle [181]. Important information about the electronic system such as the strength of electronic correlations, single particle scattering rates, etc can be extracted from the one-particle spectral function. A more detailed description of the photoexcitation process is given in [176, 179, 180, 182].

In a slightly different formulation the photocurrent can be written as

$$I(\mathbf{k}, \omega) = I_0(\mathbf{k}, \nu, \mathbf{A}) f(\omega) A(\mathbf{k}, \omega) \quad (2.9)$$

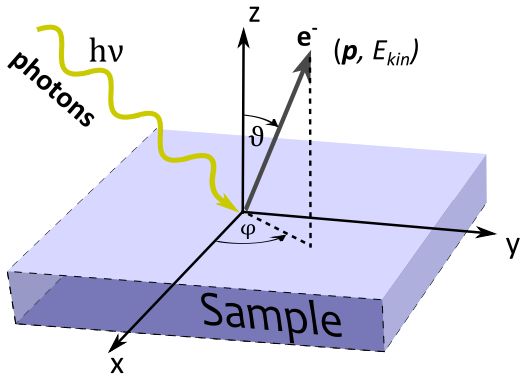

Figure 2.4: Geometry of a typical ARPES experiment. The electron emission is measured by the angles ϑ and φ. The energy of the incoming photon is given by $h\nu$.

with $I_0(\mathbf{k}, \nu, \mathbf{A}) \propto |M_{f,i}^{\mathbf{k}}|^2$ and

$$f(\omega) = \frac{1}{e^{(\omega - E_F)/k_B T} + 1} \tag{2.10}$$

denoting the Fermi-Dirac distribution function which takes into account that photoemission only probes occupied states.

Second Step: Transport of the electron to the surface

After photoexcitation, some electrons travel to the surface of the crystal without being scattered. Inelastic scattering is the main cause for electrons to lose their information about momentum and energy. The scattered electrons are called secondary electrons and contribute to the intrinsic background in the low kinetic energy shown in Figure 2.1. Usually this background is momentum independent and can be easily subtracted [183]. The *mean free path*, i.e. the average path until the electron undergoes a scattering process, depends very much on the kinetic energy of the electron. As shown in Figure 2.2, for many different elemental materials the average escape depth follows approximately an *universal curve* with a minimum at a kinetic energy of $E_{\text{kin}} = 50$ eV. At lower or higher kinetic energy, the escape depth increases and the measurement becomes more bulk sensitive. It has been demonstrated that in the soft X-ray regime the mean free path is large enough for probing the electronic structure of a material below a thin capping layer or at interfaces [184].

Third Step: Electron transmission into the vacuum and detection by electron-analyzer

ENERGY CONSERVATION

Once the electron has reached the surface of the solid, it has to overcome the surface potential barrier to escape into the vacuum. For that the kinetic energy of the electron has to be at least as high as the material work-function[5] ϕ_S or higher. All electrons with lower energy are scattered back and won't be emitted from the sample.

After transmission into the vacuum, the kinetic energy of the photoelectron is given by the energy conservation law (eq. 2.1) as also illustrated in Figure 2.3. Usually, the detector is electrically connected with the sample and therefore the Fermi level is in equilibrium. When the photoelectron enters the analyzer it gains a kinetic energy of ϕ_A -i.e. the analyzer

[5] ϕ_S depends on the sample and varies between 4 and 6 eV.

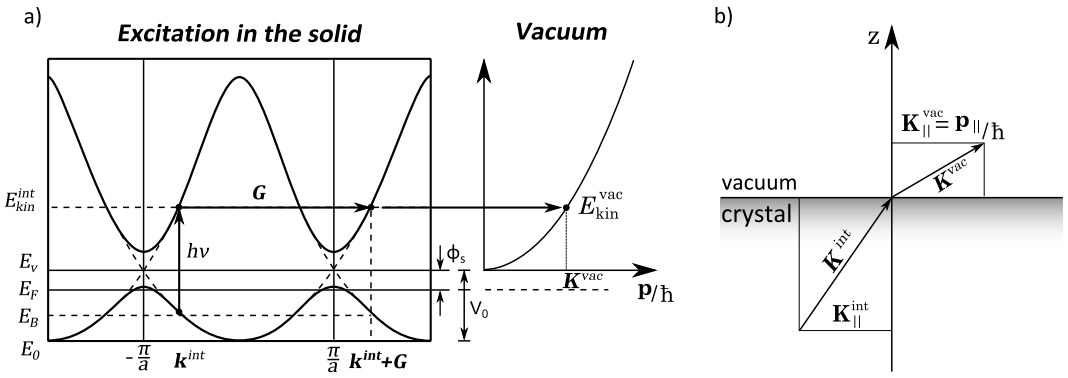

Figure 2.5: (a) Free electron final state model for PES. It is assumed that a free electron parabola with its vertex at the bottom of the valence band (E_0) intersects with the final state energy E_{kin} at the given momentum of the electron inside the crystal. The wave vector in the vacuum is then given by the intersection of the final state energy with the parabola which has its bottom at the vacuum level E_v. **(b)** Momentum diagram for third step. Free electron in crystal has momentum $\mathbf{K}^{\mathrm{int}} = \mathbf{k}^{\mathrm{int}} + \mathbf{G}$ and electron in vacuum $\mathbf{K}^{\mathrm{vac}} = \mathbf{p}^{\mathrm{vac}}/\hbar$ while only $\mathbf{K}_{||}^{\mathrm{int}} = \mathbf{K}_{||}^{\mathrm{vac}}$ is conserved. Adapted from [176].

work function. In vacuum, the photoelectron has a kinetic energy of:

$$E_{\mathrm{kin}}^{\mathrm{vac}} = h\nu - E_{\mathrm{B}} - \phi_S \tag{2.11}$$

The kinetic energy eventually measured by the detector is:

$$E_{\mathrm{kin}} = E_{\mathrm{kin}}^{\mathrm{vac}} + (\phi_S - \phi_A) = h\nu - E_{\mathrm{B}} - \phi_A \tag{2.12}$$

Once the analyzer work function ϕ_A has been determined[6], one can obtain the kinetic energies of the electrons in the solid.

MOMENTUM CONSERVATION

In vacuum the momentum of a photoelectron has an absolute value of $p = \sqrt{2m_e E_{\mathrm{kin}}^{\mathrm{vac}}}$ and its direction is given by the emission angles ϑ and φ [Fig. 2.4].
For the following discussion, the momentum of the photoelectron is split into a component parallel to the crystal surface and perpendicular:

$$\mathbf{p}/\hbar = \mathbf{K}^{\mathrm{vac}} = \mathbf{K}_{||}^{\mathrm{vac}} + \mathbf{K}_{\perp}^{\mathrm{vac}} \tag{2.13}$$

Since the crystal is considered to be semi-infinite with in-plane translational invariance, the momentum parallel to the crystal surface is conserved when the electron penetrates through the surface.

$$\mathbf{K}_{||}^{\mathrm{int}} = \mathbf{K}_{||}^{\mathrm{vac}} \tag{2.14}$$

As a function of the outgoing transmission angles [see Fig. 2.4], $\mathbf{K}_{||}^{\mathrm{vac}}$ is written as:

$$\mathbf{K}_{||}^{\mathrm{int}} = \mathbf{K}_{||}^{\mathrm{vac}} = \frac{\mathbf{p}_{||}}{\hbar} = \frac{\sqrt{2m_e E_{\mathrm{kin}}^{\mathrm{vac}}}}{\hbar} \sin\vartheta \begin{pmatrix} \cos\varphi \\ \sin\varphi \\ 0 \end{pmatrix} \tag{2.15}$$

Since the translational symmetry is broken perpendicular to the crystal surface, the determination of the perpendicular momentum requires further assumptions. In the free electron

[6] Usually, $\phi_A \approx 4.5$ eV

final state (FEFS) model it is assumed that the final state of the electron is that of a free electron [see Figure 2.5 and 2.3]:

$$E_{\mathrm{kin}}^{\mathrm{int}} = \frac{\hbar^2(\mathbf{K}^{\mathrm{int}})^2}{2m_e} - |E_0| \tag{2.16}$$

where E_0 is the bottom of the free electron parabola [see Fig. 2.5 a)]. With equation 2.11 and $E_{\mathrm{kin}}^{\mathrm{int}} = E_{\mathrm{kin}}^{\mathrm{vac}} + \phi_S$, $k_\perp$ is then given by:

$$(k_\perp + G_\perp) = \sqrt{\frac{2m_e}{\hbar^2}(E_{\mathrm{kin}}^{\mathrm{int}} + |E_0|) - (\mathbf{K}_{||}^{\mathrm{int}})^2} = \sqrt{\frac{2m_e}{\hbar^2}(h\nu - E_{\mathrm{B}} - \phi_S + V_0) - (\mathbf{K}_{||}^{\mathrm{int}})^2} \tag{2.17}$$

where $\mathbf{K}^{\mathrm{int}} = \mathbf{K}_\perp^{\mathrm{int}} + \mathbf{K}_{||}^{\mathrm{int}}$. Here, the "inner potential", $V_0 = |E_0| + \phi_S$, is an adjustable parameter.

2.2.3 Spectral function

In the preceding section the photoemission process has been described in a phenomenological three step model. In the first step, which describes the optical excitation of the electron, the spectral function $A(\mathbf{k},\omega) = A^+(\mathbf{k},\omega) + A^-(\mathbf{k},\omega)$ has been introduced as a basic quantity of photoemission spectroscopy. By definition, the spectral function is directly related to the Green's function $G(\mathbf{k},\omega)$ which describes the propagation of the electron in the crystal [179, 185, 186]:

$$A(\mathbf{k},\omega) = -\frac{1}{\pi}\mathrm{Im}G(\mathbf{k},\omega). \tag{2.18}$$

In time domain, the Green's function is defined as

$$\begin{aligned} G(\mathbf{k}_1,t_1;\mathbf{k}_2,t_2) &= \Theta(t_1-t_2)G^-(\mathbf{k}_1,t_1;\mathbf{k}_2,t_2) + \Theta(t_2-t_1)G^+(\mathbf{k}_1,t_1;\mathbf{k}_2,t_2) \\ &= i\Bigg[\Theta(t_1-t_2)\langle\Psi_0^N|c_{k_1}(t_1)c_{k_2}^\dagger(t_2)|\Psi_0^N\rangle \\ &\quad - \Theta(t_1-t_2)\langle\Psi_0^N|c_{k_2}^\dagger(t_2)c_{k_1}(t_1)|\Psi_0^N\rangle\Bigg]. \end{aligned} \tag{2.19}$$

Here, the creation and annihilation operators $c_k^\dagger(t)$, $c_k(t)$ are given within the Heisenberg picture $c_k^{(\dagger)}(t) = \exp(\frac{i}{\hbar}Ht)c_k^{(\dagger)}\exp(\frac{i}{\hbar}Ht)$ and $\Theta(t)$ denotes the heavy-side function. The transformation into frequency domain gives

$$G^\pm(\mathbf{k},\omega) = \sum_m \frac{|\langle\Psi_m^{N\pm1}|\hat{c}_k^\pm|\Psi_i^N\rangle|^2}{\omega \mp (E_m^{N\pm1} - E_i^N) \pm i\eta}. \tag{2.20}$$

To evaluate the many-body Green's function for a system with interactions, F.J. Dysen introduced the *self energy* $\Sigma(\omega)$ as an energy-dependent effective potential. The interactions of the single-particle with the many-body system can be treated within a one particle formalism [185, 187]. By adding the self energy $\Sigma(\mathbf{k},\omega) = \Sigma'(\mathbf{k},\omega) + i\Sigma''(\mathbf{k},\omega)$ to the single-particle electron energy, $\epsilon_{\mathbf{k}}$, and using equation 2.18 the Green's function and the spectral function transform into

$$G(\mathbf{k},\omega) = \frac{1}{\omega - \epsilon_k - \Sigma(\mathbf{k},\omega)} \tag{2.21}$$

$$A(\mathbf{k},\omega) = -\frac{1}{\pi}\frac{\Sigma''(\mathbf{k},\omega)}{[\omega - \epsilon_k - \Sigma'(\mathbf{k},\omega)]^2 + [\Sigma''(\mathbf{k},\omega)]^2} \tag{2.22}$$

Note that the Green's function is a linear response function to an external perturbation with causality between the real and imaginary part. Therefore the real and imaginary part

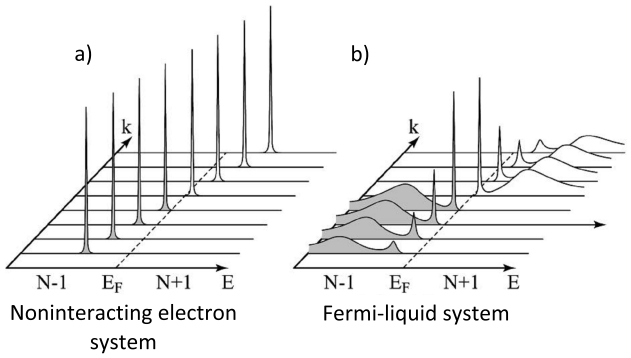

Figure 2.6: **(a)** Momentum and energy resolved one-electron removal ($E < E_F$) and addition ($E > E_F$) spectral function for an non-interacting electronic system with a single band crossing E_F. **(b)** The same spectrum for the case when electronic correlation is finite, represented by the case of an interacting Fermi-liquid. Adapted from [44].

of $G(\mathbf{k},\omega)$ and $\Sigma(\mathbf{k},\omega)$, respectively, have to fulfill the Kramer-Kronig relations. For the trivial, non-interacting system, $\Sigma(\mathbf{k},\omega) = 0$ and the observed electron dispersion reflects a single eigenstate of the $N \pm 1$-particle ground state. Whereas, if correlations are present, the final state is not an eigenstate of the system anymore and electronic states have a reduced lifetime and renormalized energy $\epsilon_{\mathbf{k}}$ with an increased effective mass m^*, respectively. The spectral function is then split into a coherent part which is, as illustrated in Figure 2.6 reminiscent of the sharp non-interacting case and an incoherent part which is a rather broad feature in the spectrum [see Fig. 2.6 b)]. The coherent spectral weight is scaled by the so called *coherence factor* $Z_{\mathbf{k}} = (1 - \partial\Sigma'/\partial\omega)^{-1}$. With $\epsilon'_{\mathbf{k}} = Z_{\mathbf{k}}(\epsilon_{\mathbf{k}} + \Sigma')$ and $\Gamma_{\mathbf{k}} = Z_{\mathbf{k}}\Sigma''$, the spectral function in the Fermi liquid case is written as

$$A(\mathbf{k},\omega) \quad = \quad \frac{1}{\pi}\frac{Z_{\mathbf{k}}\Gamma_{\mathbf{k}}}{[\omega - \epsilon'_{\mathbf{k}}]^2 + \Gamma^2_{\mathbf{k}}} + A_{incoh} \tag{2.23}$$

2.2.4 Resolution

The ARPES measurement can be affected by many intrinsic respectively external effects. For example, secondary electrons contribute to the background of the ARPES spectra and the finite instrumental resolution will broaden the ARPES signal. Also, the signal will be broadened by the the instrumental resolution. Therefore a realistic description of the experimental ARPES intensity is given by the convolution of eq. 2.9 with the energy resolution function $R(\omega)$, the momentum resolution function $Q(\mathbf{k})$ and the background B.

$$I^{\exp}(\mathbf{k},\omega) = \int d\omega' d\mathbf{k}' I_0(\mathbf{k},\nu,\mathbf{A}) f(\omega') A(\mathbf{k}',\omega') R(\omega - \omega') Q(\mathbf{k} - \mathbf{k}') + B. \tag{2.24}$$

Usually $R(\omega)$ is of Gaussian form but $Q(\mathbf{k})$ has no generalized form. Also the background function B could take different forms: It could be simply a constant or a of more elaborate form like the often used, so called Shirley background [188]. Although the momentum resolution function is not exactly known, the momentum resolution $\Delta\mathbf{k}$ can be analyzed. As described by equation 2.15 the in-plane momentum $\mathbf{k}_{||}$ depends on the precision of the measured outgoing angle ϑ and the value of the kinetic Energy E_{kin}. Therefore, $\Delta\mathbf{k}_{||}$ is given by

$$\Delta\mathbf{k}_{||} \sim \sqrt{2m\frac{E_{\text{kin}}}{\hbar^2}} cos\vartheta \cdot \Delta\vartheta. \tag{2.25}$$

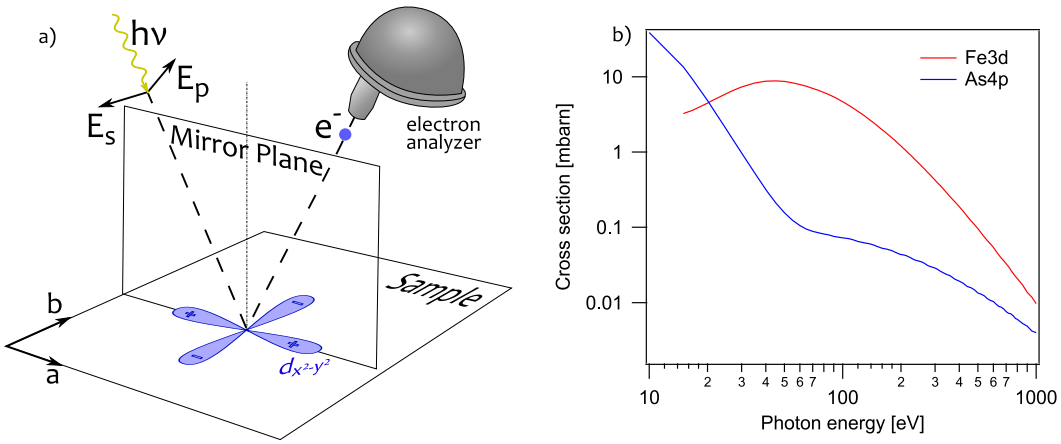

Figure 2.7: **(a)** Schematic of an ARPES experiment on a $d_{x^2-y^2}$ derived initial state. The symmetry of a $d_{x^2-y^2}$ orbital is represented by the blue object. The mirror plane is defined by the orbital. To derive the polarization selection rules, the detector and in-coming photon are positioned in the mirror plane. The photon polarization can be in-plane (E_p) or perpendicular to the mirror plane (E_s). Adapted from [44]. **(b)** Calculated energy dependence of the photo ionization cross section for Fe $3d$ and As $4p$ states [190].

In an ARPES experiment $\Delta\vartheta$ is given as a constant of the measurement setup and depends mainly on the installed electron analyzer. For state of the art analyzers $\Delta\vartheta \approx 0.15°$ which gives $\Delta\mathbf{k}_{||} \approx 0.01\text{Å}^{-1}$ at $h\nu \sim 20$ eV. As stated by equation 2.25 the in-plane momentum resolution can be improved during an ARPES experiment by lowering the photon energy or measuring at larger emission angles ϑ.
The out of plane momentum resolution $\Delta\mathbf{k}_\perp$ is basically determined by the inverse escape depth [189]

$$\Delta\mathbf{k}_\perp \sim \frac{1}{\lambda}. \tag{2.26}$$

As illustrated in Figure 2.2, the mean free path of the photoelectron has a minimum for kinetic energies between 50 eV and 100 eV and increases towards higher energies leading to improved $\Delta\mathbf{k}_\perp$. Consequently the resolution of the in-plane and out of plane momentum have opposed photon energy dependence.

2.2.5 Matrix elements

As presented in the formalism about the optical excitation of an electron the ARPES intensity depends on the squared matrix element $|M^{\mathbf{k}}_{f,i}|^2 = |\langle\phi^{\mathbf{k}}_f|V_{\text{ep}}|\phi^{\mathbf{k}}_i\rangle|^2$ with $V_{\text{ep}} \propto \mathbf{A}\cdot\mathbf{p}$. Since the momentum operator fulfills the commutator relation $\hbar\mathbf{p}/m = -i[\mathbf{x}, H]$, the matrix element can be written as

$$|M^{\mathbf{k}}_{f,i}|^2 \propto |\langle\phi^{\mathbf{k}}_f|\mathbf{e}\cdot\mathbf{x}|\phi^{\mathbf{k}}_i\rangle|^2 \tag{2.27}$$

where $\mathbf{e}$ is the unit vector along the direction of the photon vector potential $\mathbf{A}$. The following example will explain the light polarization selection rules of the ARPES intensity in the case of a $d_{x^2-y^2}$ initial state. If we consider the geometrical setup, as indicated in Figure 2.7, such that the incoming light and the outgoing electron trajectory lie in the mirror plane of the initial state ($d_{x^2-y^2}$ orbital) the overall symmetry of $|M^{\mathbf{k}}_{f,i}|^2$ has to be even. In the FEFS approximation we assume that the photo-electron wave function is a plane wave $\phi^{\mathbf{k}}_f \propto \exp(-i\mathbf{k}\cdot\mathbf{r})$ which has even parity. To fully **suppress** the ARPES intensity the

following matrix relation has to be satisfied [44, 176]:

$$\langle e^{-i\mathbf{k}\cdot\mathbf{r}}|\mathbf{e}\cdot\mathbf{x}|\phi_i^{\mathbf{k}}\rangle = 0 \quad \text{for} \begin{cases} \text{if } \phi_i^{\mathbf{k}} \text{ even} & \text{and } \mathbf{A} \text{ odd; } \langle +|-|+\rangle \\ \text{if } \phi_i^{\mathbf{k}} \text{ odd} & \text{and } \mathbf{A} \text{ even; } \langle +|+|-\rangle \end{cases} \tag{2.28}$$

Here $\mathbf{A}$ was defined to be even if the direction of the polarization vector is in-plane ($\mathbf{e} \parallel \mathrm{E_p}$) or odd if ($\mathbf{e} \parallel \mathrm{E_s}$). In ideal case, the ARPES intensity of a particular initial state may be completely suppressed. However, if these conditions are not entirely fulfilled, partial intensity will be observed. In conclusion, this method presents a way to distinguish between bands which are composed by different orbitals (with different symmetry) in a multi-band system.

Besides the polarization of the photon, the photon energy is a parameter which has strong impact on the matrix element and therefore on the photoemission intensity. In Figure 2.7 b), the energy dependence of the photo ionization cross section is compared for the Fe $3d$ and As $4p$ initial states. It can be observed that the energy dependence of the cross section of different atomic shells differ significantly and therefore allow to further tune the orbital sensitivity of the ARPES experiment.

2.3 Application

2.3.1 Lightsources

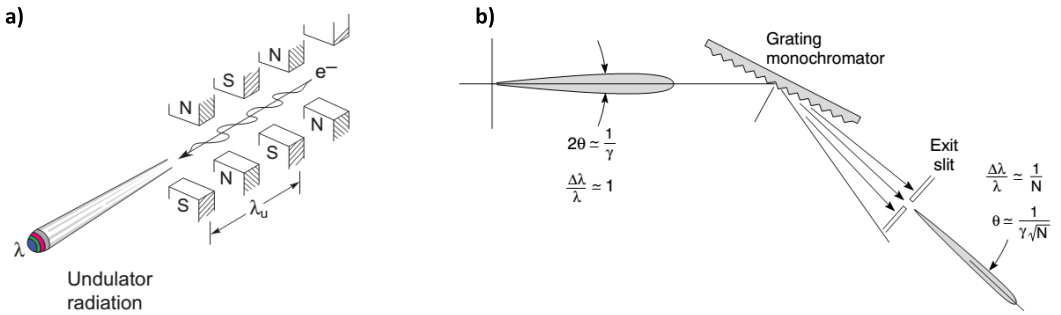

Figure 2.8: **(a)** Schematic illustration of an undulator. λ_u denotes the periodicity of the magnet-arrangement and N the number of oscillation periods. **(b)** Sketch of a planar grating monochromator as the most important part of a beamline. $\Delta\lambda$ is the 'natural' band width. Adapted from [191].

In lab systems light sources are usually Helium- or Xenon-discharge lamps ($h\nu \sim 21$ eV, $h\nu \sim 8$ eV) and Laser sources ($6 - 14$ eV). The advantage of such sources is that they are relatively easy to handle and are not too large/expensive. Disadvantages are the narrow available energy range, limitations in polarization and brilliance as well as spot size. All these parameters, the full spectrum from UV (~ 8 eV) to hard X-ray ($5 - 10$ keV) with full choice of polarization, high brilliance and small spot size are provided at a synchrotron light source [192, 193]. In a synchrotron, electrons are accelerated in a linear accelerator (LINAC) to high velocities ($v \approx c$) and injected into a ultra high vacuum storage ring where they are kept at constant kinetic energy (2.4 GeV at Swiss Sight Source (SLS)). The storage ring of a third-generation synchrotron, like SLS, has straight sections where so-called *undulators* are installed. An undulator is an array of aligned magnets in which the electrons execute a "slalom" motion [see Fig. 2.8 a)]. The synchrotron light is produced when charged particles are accelerated. In this case they are deflected by the magnetic field B_0 when they are forced on the slalom track. For slow particles (v≪c) the radiation is emitted isotropically

in all directions, similar to that of an oscillating dipole (classical antenna). For relativistic speeds ($v \approx c$), the angular distribution of the emitted light has the form of a narrow cone of width $1/\gamma$ (with $\gamma = (1-\beta^2)^{-1/2}$, $\beta = \frac{v}{c}$), as illustrated in Figure 2.8 b). The advantage of the undulator is, that the light produced in the beginning of the undulator interferes with the light produced by the successive slalom periods, until the electron has passed through the whole undulator with N periods. Consequently the intensity depends strongly on the undulator wavelength λ_u and peaks at a constructive interference wavelength which is, for ($v \approx c$) determined by

$$\lambda = \frac{\lambda_\mathrm{u}}{2\gamma^2}\left(1 + \frac{K^2}{2}\right) \tag{2.29}$$

with the dimensionless constant $K = eB_0\lambda_u/2\pi mc$. Thus, the tuning parameters B_0 and λ_u allow to continuously change the wavelength of the emitted light. From the undulator the photon-beam will be guided through a beamline to the sample in the measurement-endstation. The most important ingredient of a beamline is the monochromator [see Fig. 2.8 b)], which is usually composed by plane gratings and the exit slit, which together set the energy resolution (band width) of the photon beam.

2.3.2 SIS and ADRESS beamline

At Swiss Light Source (SLS) with the Surface and Interface Spectroscopy (SIS) beamline and Advanced Resonance Spectroscopies (ADRESS) beamline, there are two beamlines which are equipped with an ARPES endstation. The majority of the data presented in this work has been measured at these two beamlines. The SIS beamline is designed for the ultra violet (UV) photon energy range [194] and provides four different photon polarizations (linear horizontal (LH), linear vertical (LV), circular plus (CP) and circular minus (CM)). The ADRESS beamline is designed for the soft X-ray regime [195, 196] and also provides four photon polarizations. Beamline specifications for both beamlines are listed in table 2.1. The advantages of UV-ARPES compared to ARPES in the SX regime are:

- Higher overall energy resolution which is usually between 5 and 20 meV compared to $>$ 35 meV for SX-ARPES.
- Better in-plane momentum resolution (directly connected to energy resolution [see equation 2.25]).
- Larger photo excitation cross section [see Figure 2.7 b)].
- Smaller influence of Debye Waller factor on intensity [see Ref. [196]].

Disadvantages are:

- Lower out-of-plane momentum resolution (directly connected to photon energy [see equation 2.26]).
- Smaller penetration depth [see Fig. 2.2].

Table 2.1: Beamline specifications of the SIS and ADRESS beamline at Swiss Light Source, PSI.

	Energy [eV]	**resolving power** $E/\Delta E$	**flux**	**spot size**
SIS	10 - 800	10000	(at 20 eV) $10^{15} ph/s/0.1\%$BW	50 x 100 μm^2
ADRESS	300 - 1600	33000	(at 1 keV) $10^{13} ph/s/0.01\%$BW	10 x 75 μm^2

2.3.3 Sample preparation for an ARPES experiment

The experiments presented in this work have been conducted on bulk single crystals[7]. Before the experiment the crystals have been aligned using a Laue diffractiometer and cut by a tungsten wire saw to a typical size of 1 x 1 x 1 mm^3. In the next step, the crystals were glued on the copper sample holders [see Fig. 2.9 b)] with electrically and thermally conducting silver epoxy[8]. For the air sensitive compounds (compounds which usually contain Alkaline metal elements, e.g. NaFeAs) the whole sample preparation has been conducted in Helium atmosphere and non-reacting glue has been used instead of silver epoxy[9]. After curing the glue for several hours on a hot plate ($80 - 100$ °C) the samples were introduced via a prevacuum chamber (load lock with pressure $\sim (10^{-8})$ mbar) into the main chamber which was kept constantly under ultra high vacuum (UHV) ($< \mathcal{O}(10^{-10})$ mbar). Before putting the sample on the main manipulator, the polycrystalline sample holder resp. a gold foil close to the sample has been sputtered for ~ 30 minutes to supply a reference spectrum for detector calibration. After clamping the sample into the cold finger of the cryostat [see Fig. 2.9 c)] and establishing the desired temperature the sample has been cleaved with either a top-post glued on the sample top surface or a specially designed cleaving tool [197]. Since ARPES probes the first few atomic layers, such a procedure is absolutely necessary since it provides a clean surface. At low temperatures in the UHV chamber, the sample surface live-time is between 1 and 4 days, strongly depending on the material.

2.3.4 CARVING manipulator - angle to k-space transformation

Both, the UV-ARPES and the SX-ARPES endstation are equipped with a *CARVING* manipulator which has six degrees of freedom (3 translational, 3 rotational) and has a temperature range from 10 K up to 300 K. The head of the manipulator is shown in Figure 2.9 c) with the three rotational degrees of freedom indicated by (θ, ϕ, χ). The round sample holder [Fig. 2.9 b)] is mounted in the center of the head clamped onto the cold finger, in excellent thermal contact with the liquid Helium cryostat and electrically well grounded. It is of great advantage to have 3 rotational degrees of freedom since it allows to (re-)align the sample during the measurement in such a way that every cut along a certain direction in $k-$space can be obtained. The following section will describe the transformation of manipulator angles into momentum space. It will also include a description how to correct for misalignment between the sample coordinate system (CS) and manipulator CS - i.e. for the likely case that the sample is not perfectly glued on the sample holder but slightly tilted.

The laboratory frame (x', y', z') is defined as indicated in Figure 2.9 a). The z'-axis points towards the center of the nose of the analyzer, the x'-axis is the second horizontal axis and the y'-axis is vertical. In the initial position $(\theta, \phi, \chi) = (0, 0, 0)$, the manipulator CS (x'', y'', z'') is equal to the laboratory CS [see Fig. 2.9 d)]. In laboratory frame, the electron momentum for the horizontal analyzer slit is expressed by:

$$\mathbf{k}' = k \begin{pmatrix} -\sin\alpha \\ 0 \\ \cos\alpha \end{pmatrix} \tag{2.30}$$

where $k = \sqrt{2mE_{\mathrm{kin}}^{\mathrm{vac}}}/\hbar$ is the absolute value of the electron momentum. Now, the goal is to transform $\mathbf{k}'$ into $\mathbf{k}$ which is given in the intrinsic coordinates of the crystal (x, y, z). Note that during the transformation the absolute value, k, will be unchanged. First, $\mathbf{k}'$ is transformed into the CS of the sample holder, $\mathbf{k}''$, and then the correction of the crystal

[7] At SIS beamline it is also possible to perform ARPES measurements on thin films which have been grown in-situ by pulsed laser deposition (PLD).

[8] According to the sample different types have been used: EPO-TEK E4110, H20S, H21D from POLYSCIENCE.

[9] Insulating Torr Seal from Varian in combination with graphite.

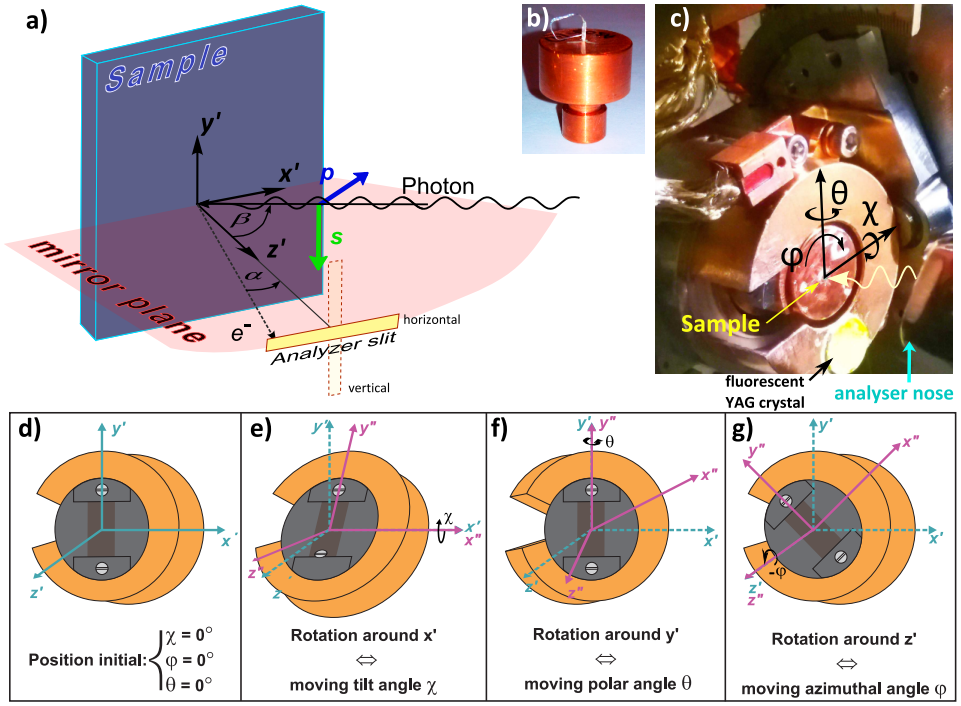

Figure 2.9: **(a)** Schematic drawing of the ARPES experimental setup. The laboratory frame is denoted by (x', y', z'). In this frame, the z'-axis points towards the center of the nose of the analyzer, the x'-axis as the second horizontal axis lies in the mirror plane and the y'-axis is vertical. The angle between incoming beam and z' axis is $\beta = 45°$ at SIS and $\beta = 25°$ at ADRESS. The angle α denotes the angle of the outgoing electron to the z' axis, in the mirror plane. The mirror plane is defined by the incoming photon beam and the z' axis. **(b)** Typical copper sample holder with a post glued on flat sample and wire attached to the post. **(c)** Photograph of the head of the CARVING manipulator with the rotational degrees of freedom indicated by $(\theta, \phi, tilt = \chi)$. **(d) - (g)** Illustration of different rotational degrees of freedom of the CARVING manipulator. Adapted from [198].

misalignment with respect to the sample holder is applied. To transform $\mathbf{k}'$ into the sample holder CS, the three rotation matrices for all three independent rotation axes have to be considered.

$$R_\Theta = \begin{pmatrix} \cos\Theta & 0 & -\sin\Theta \\ 0 & 1 & 0 \\ \sin\Theta & 0 & \cos\Theta \end{pmatrix}, R_\chi = \begin{pmatrix} 1 & 0 & 0 \\ 0 & \cos\chi & \sin\chi \\ 0 & -\sin\chi & \cos\chi \end{pmatrix}, R_\Phi = \begin{pmatrix} \cos\Phi & -\sin\Phi & 0 \\ \sin\Phi & \cos\Phi & 0 \\ 0 & 0 & 1 \end{pmatrix} \tag{2.31}$$

Now, $\mathbf{k}''$ (in sample holder CS) is given by

$$\mathbf{k}'' = R_\Phi R_\chi R_\Theta \mathbf{k}' \tag{2.32}$$

For the very likely case that the sample is not properly aligned with the sample holder and slightly tilted, the $\mathbf{k}''$ has to be corrected in order to get the momentum in the CS of the crystal, $\mathbf{k}$. In this correction, the z and z'' will be aligned but the azimuthal angle, ϕ, won't be corrected (this is a simple offset). The final transformation is given by

$$\mathbf{k} = \begin{pmatrix} \cos\beta & -\sin\beta & 0 \\ \sin\beta & \cos\beta & 0 \\ 0 & 0 & 1 \end{pmatrix} \begin{pmatrix} \cos\gamma & 0 & -\sin\gamma \\ 0 & 1 & 0 \\ \sin\gamma & 0 & \cos\gamma \end{pmatrix} \begin{pmatrix} \cos\beta & \sin\beta & 0 \\ -\sin\beta & \cos\beta & 0 \\ 0 & 0 & 1 \end{pmatrix} R_\Phi R_\chi R_\Theta \, \mathbf{k}' \tag{2.33}$$

where γ denotes the magnitude of the misalignment between z (sample) and z'' (sample holder) and β the direction in which z is "tilted". In case of a vertical analyzer slit, the transformation would be similar but $\mathbf{k}'$ of equation 2.30 has the following form $\mathbf{k}' = k(-\sin\alpha, \cos\alpha, 0)^T$.

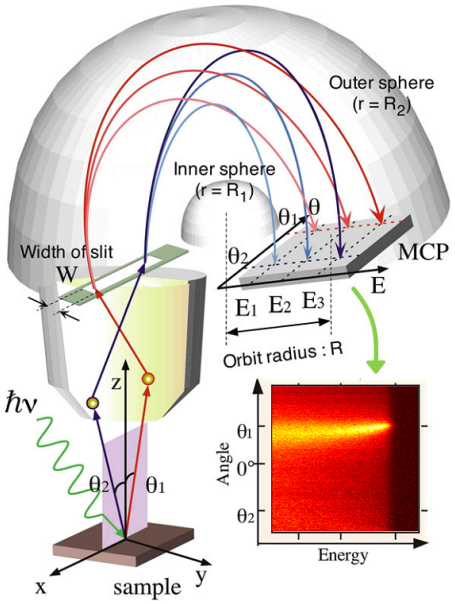

Figure 2.10: Schematic of a hemispherical electron energy and momentum analyzer. Adapted from [199].

2.3.5 Electron analyzer

At the heart of any ARPES endstation is the electron analyzer. There exist many different methods to analyze the energy of charged particles e.g. electrons [176]. One type of instruments is the time-of-flight analyzer which is able to obtain a full 3D map (k_x, k_y, E_B) but has limitations in energy resolution and has particular requirements on the light source. Another type is the spherical deflection analyzer (or hemispherical deflection analyzer, HDA) which consists of a concentric inner and outer hemisphere which are on different electrostatic potentials [see Fig. 2.10]. The electrons pass through the entry slit, are deflected by the electric field between the spheres and are detected by a two dimensional detector[10]. If an electron with energy E_0 enters exactly between the two spheres (at a radius $R_0 = (R_1 + R_2)/2$), the potential difference between the inner and the outer sphere ΔV has to be

$$e\Delta V = E_0(R_1/R_2 - R_2/R_1) \tag{2.34}$$

All electrons with a slightly higher or lower energy will reach the detector either at a larger or smaller radius. The energy resolution of such an analyzer is given by $\Delta E = KE_0$ where the constant K depends on the analyzer geometry. In order to improve the resolution, the electrons are retarded prior they enter the hemispheres to decrease their energy E_0. In this process, the electrons are decelerated without changing the absolute spread in their energy. The energy to which the electrons are decelerated is called the pass energy, E_p. The second direction of the 2D-detector (tangential to the spheres) gives the momentum of the electrons

[10] Old fashioned analyzers don't have an entrance slit and instead have a single pinhole for entrance and a single pinhole in front of the detector.

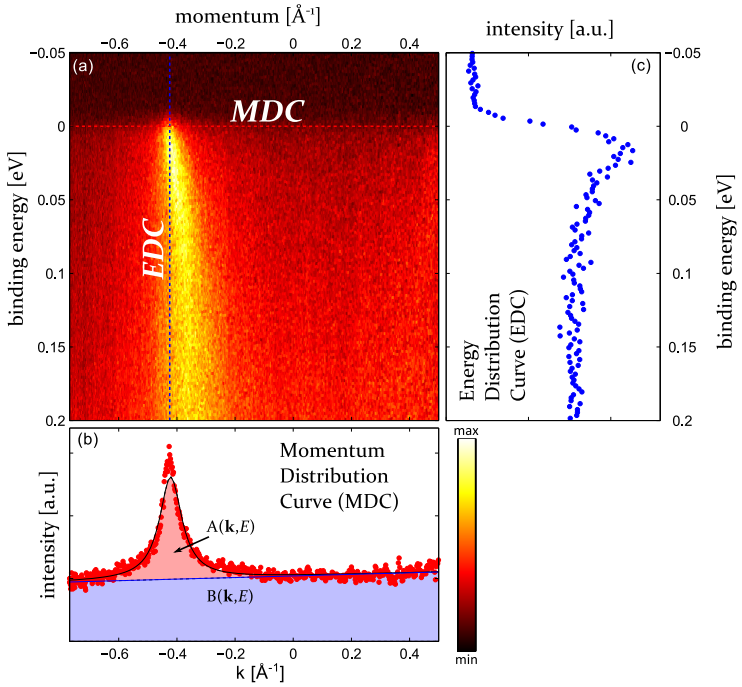

Figure 2.11: **(a)** ARPES intensity map showing the band dispersion of $La_{1.6-x}Nd_{0.4}Sr_xCuO_4$ $x = 0.20$ as function of the binding energy and momentum **k**. The horizontal red dashed line indicates the position of the momentum distribution curve (MDC) presented in **(b)** and the blue line the position of the energy distribution curve (EDC) shown in **(c)**. Extrinsic background is indicated by the blue shaded area in **b)** ($\sim B(\mathbf{k}, E)$ and the red region illustrates intensity described by the spectral function $A(\mathbf{k}, E)$. The black line is a Lorentzian fit of the MDC-spectral function. Adapted from [200].

and corresponds to their "takeoff-direction" from the sample.
In modern analyzers, the detector consists of several building blocks. In the first stage, when the electrons arrive at the detector, the electron-intensity is amplified by a multichannel plate (MCP). Then, the electrons are accelerated and hit a phosphor-coated screen where they create fluorescent light which is detected by a CCD camera. The detector-resolution is in general given by the spot size of a single event.

The electron analyzer which is installed at the UV-ARPES endstation at the SIS beamline is a Scienta R4000 ($\pm 15°$)[11] or at SX-ARPES endstation a SPECS PHOIBOS-150 (variable acceptance angles $\pm 4°$ or $\pm 8°$). All data presented in this thesis has been acquired by using those analyzers.

2.3.6 Data analysis

A typical ARPES spectrum is shown in Figure 2.11 in a color-coded energy versus momentum intensity plot which shows the valence band of NdLSCO along the (π, π) direction. In principle the intensity is given by the spectral function [see equation 2.22 and 2.23)]. In order to extract quantitative information, the spectrum can be analyzed along the energy or momentum direction. The energy distribution curve (EDC) along the blue dashed line

[11] some data has been recorded with a Scienta SES-2002 (angular acceptance angle $\pm 8°$) which has been previously installed at the SIS beamline.

in panel a) is shown in panel c). Along this direction, the spectrum is characterized by a peak at $E_B <\approx 0$ and suppression of spectral weight for negative binding energies due to the Fermi-Dirac distribution function. The momentum distribution curve (MDC), along the red dashed line in panel a) is taken at the Fermi level and presented in panel b). In this case it is characterized by a single peak which stems from the single band which is crossing the Fermi level and a background. It has been shown that the low energetic MDC background ($E < 0.2$ eV is purely extrinsic and can be modeled by a linear curve [183]: $B_{\mathrm{MDC}}(\mathbf{k}, E) = a + bk$. The intrinsic signal, which is the total signal without the extrinsic background is then best described by a Lorentzian lineshape (black line fitted to red data points). A data analysis based on the MDC and EDC line shape is the standard way of ARPES-data analysis and will be used regularly throughout this work. Whenever the analysis becomes more intricate and specialized, an introduction of the methods will be given.

Chapter 3

Electron scattering, charge order, and pseudogap physics in $La_{1.6-x}Nd_{0.4}Sr_xCuO_4$

3.1 Introduction

Partial gapping of spectral weight in the apparent absence of any metal instability appears in many strongly correlated electron systems [201–204]. This so-called pseudogap phenomenon is, for example, found in the normal state of charge-density-wave (CDW) systems, above the CDW onset temperature [166]. A pseudogap phase has also been reported in the normal state of high-temperature cuprate superconductors. The nature of these pseudogaps is still being debated [81, 205–213]. Recently, it has become clear that charge ordering is a universal property of hole-doped cuprates [90, 91, 214–226]. Around the so-called 1/8-doping, the CDW onset temperature appears much before the superconducting transition temperature. The normal state of cuprates should hence be revisited to identify a single particle gap from CDW order and to investigate the spectral gapping in absence of both superconductivity and CDW order. We therefore present an angle-resolved photoemission spectroscopy (ARPES) study of the well-known charge stripe ordered system $La_{1.6-x}Nd_{0.4}Sr_xCuO_4$ (Nd-LSCO), in which charge and spin orders are coupled [88, 227]. As shown in the phase diagram [Fig. 3.1], this material has a strongly suppressed superconducting transition temperature, which allows a low temperature study of the normal state. We have studied the spectral lineshape evolution as a function of momentum, temperature and doping. On the overdoped side, Nd-LSCO $p = 0.20$, a spectral gap is observed at $(\pi, 0)$[1]. This gap can be closed by either increasing doping to $p = 0.24$, increasing temperature to $T \sim 80$ K or moving in momentum towards the zone diagonal. The normal state gap Δ redistributes spectral weight up to $\sim 2.5\Delta$, but the total weight remains conserved. Analysis of the spectral lineshape suggests a correlation between the gap amplitude and electron scattering. In the underdoped regime $p < 0.15$, the lineshape at $(\pi, 0)$ changes. Compared to the overdoped side of the phase diagram, a significant suppression of spectral weight is observed. This effect is discussed in terms of quasiparticle decoherence and competing orders. In particular, the idea that charge stripe order can contribute to the suppression of spectral weight at $(\pi, 0)$ is discussed.

[1] In the following $(\pi, 0)$ will be used for the location in the BZ which is often described as the antinodal region located at $(k_x, k_y) = (\pi, 0)\ a^{-1}$, in the literature. The diagonal region ($(k_x, k_y) = (\pi, \pi)\ a^{-1}$) in the BZ where the node of the d-wave order parameter is located will be noted as (π, π).

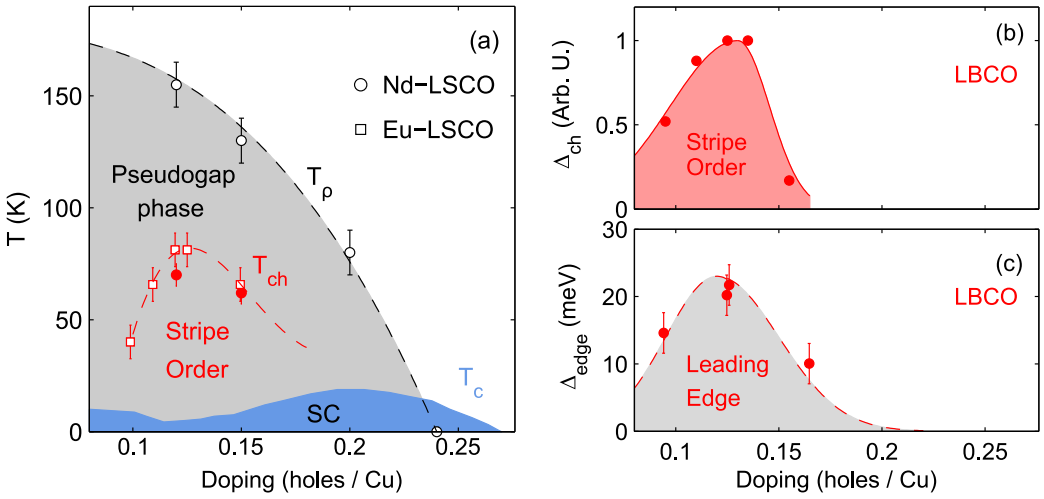

Figure 3.1: **(a)** Temperature-doping phase diagram of $La_{1.6-x}Nd_{0.4}Sr_xCuO_4$ (Nd-LSCO), established by diffraction and resistivity experiments [88, 207, 228–230]. The temperature scale T_ρ is determined by the deviation from high-temperature linear resistivity [207]. The charge ordering temperature (T_{ch}) is obtained from x-ray diffraction [88, 229, 230]. All lines are guides to the eye. **(b)** Charge stripe order parameter Δ_{ch}, derived from hard x-ray diffraction experiments on $La_{2-x}Ba_xCuO_4$ (LBCO) [89]. **(c)** Leading edge gap of LBCO versus doping, from Ref. [231].

3.2 Methods

All experiments presented in this chapter were carried out at the Surface and Interface Spectroscopy (SIS) beam line, [194] using 55 eV circular polarized photons. Single crystals of Nd-LSCO with $x = p = 0.12$, 0.15, 0.20 and 0.24 were cleaved *in-situ* under ultra-high vacuum (UHV) conditions ($\sim 0.5 \times 10^{-10}$ mbar) using a top-post technique or a specially designed cleaving tool [197]. Photo-emitted electrons were analyzed using a SCIENTA 2002 or a R4000 analyzer. A total energy resolution of $\sim$ 15 meV was achieved with this setup. Due to matrix element effects, all data were recorded in the second Brillouin zone but represented by the equivalent points in the first zone.

3.2.1 Acknowledgements

All high quality single crystals of Nd-LSCO with $x = p = 0.12$, 0.15, 0.20 and 0.24 and LSCO with $x = p = 0.105$, 0.12, 0.145, 0.23 were grown by the traveling zone method. Nd-LSCO samples with $x = 0.12$ and all LSCO samples were grown by N. Momono (Department of Applied Sciences, Muroran Institute of Technology, Muroran, Japan), M. Oda, T. Kurosowa and M. Ido (Department of Physics, Hokkaido University, Sapporo, Japan). All Nd-LSCO samples with $x > 0.12$ have been grown by J.-Q. Yan (Materials Science and Technology Division, Oak Ridge National Laboratory, Oak Ridge, Tennessee, USA) and J.-S. Zhou and J. B. Goodenough (Texas Materials Institute, University of Texas at Austin, Austin, Texas, USA). All samples were characterized by x-ray diffraction and the superconducting transition temperature determined by magnetization and resistivity measurement. We would like to thank the sample growers for supplying high quality single crystals.

3.2.2 Detector calibration

Figure 3.2 a) shows the bare spectrum of a polycrystalline copper surface which has been Ar-sputtered in-situ. The Fermi level can be roughly estimated at $\sim$ 50.65 eV, however the precise position of the step varies from channel to channel. Therefore, to calibrate the

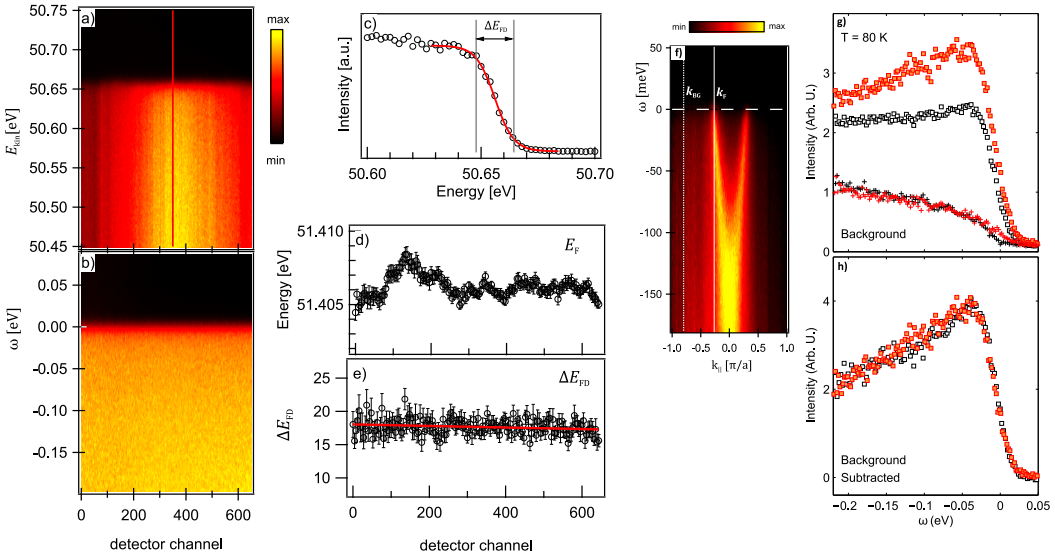

Figure 3.2: **(a)** Raw ARPES spectrum obtained from a clean polycrystalline copper surface. **(b)** Same spectrum as a) but corrected for the chemical potential and detector efficiency of each EDC. **(c)** EDC along red line in a). Red curve indicates fit with a Fermi-Dirac (FD) distribution function. ΔE_{FD} denotes step-width of FD function. **(d)** Position of E_{F} as extracted from the FD-fit of each EDC. **(e)** ΔE_{FD} as extracted from FD-function fit for each EDC. **(f)** Spectrum of $La_{1.6-x}Nd_{0.4}Sr_xCuO_4$, (p=0.2) in the region at $(\pi, 0)$. Comparison of spectra at $(\pi, 0)$ recorded on different surfaces of Nd-LSCO $p = 0.12$ at $T = 80$ K. **(g)** Raw spectra at k_F and at momentum k_{BG}, representing the extrinsic background. Intensities have been normalized so that the background intensities match across different experiments. In this fashion, it is shown how the same spectral lineshape can appear different due to a different signal-to-background ratio. Spectra, at $T \sim 80$ K, were taken after cleaving at $T = 20$ K (black) and at 80 K (red). **(h)** Background subtracted spectra, scaled by an arbitrary constant.

detector each channel of the Cu-spectrum is fitted by the Fermi-Dirac (FD) distribution (eq. 2.10 and Figure 3.2 c-e). The fit by the FD distribution function also provides an estimation of the experimental resolution which is defined as the width of the Fermi-step, ΔE_{FD}. Once the contribution from temperature broadening is deconvoluted from ΔE_{FD}, the instrumental resolution $R(\omega)$ is obtained. All spectra have been corrected by a reference from poly-crystalline copper which is in thermal and electric contact with the sample and has been taken under identical conditions immediately before or after the measurement on the sample. It has also been observed that the efficiency varies for each channel-plate in the detector. To correct for such intensity variations, the spectra have been normalized by the integrated intensity of each channel.

3.2.3 Background subtraction

As already mentioned before, ARPES spectra are composed of an intrinsic signal on top of an extrinsic background which typically varies slowly with momentum and excitation energy $\omega = E - E_{\mathrm{F}}$. A typical binding energy dependence of the background (Background-EDC) can be evaluated at momenta k_{BG}, far away from k_F [see white dotted line in Figure 3.2 f)]. We found that across all dopings studied, the background has a very similar intensity profile as a function of ω. It is thus possible to scale ARPES intensities using this background. In Figure 3.2 g), h), the background of two Nd-LSCO $p = 0.12$ spectra at $(\pi, 0)$ recorded under comparable conditions but on different samples is shown. The background can be scaled/ normalized to give an essentially perfect match. Energy-distribution curves recorded at k_F

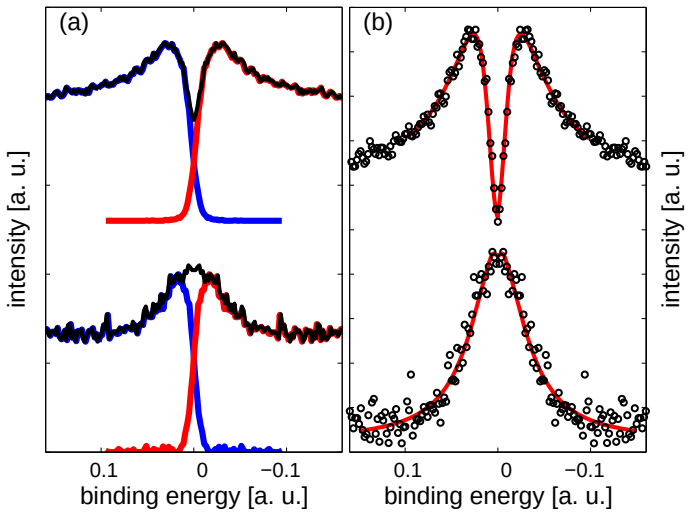

Figure 3.3: **(a)** *Blue*: EDC of Nd-LSCO $x = 0.20$ at $\mathbf{k}_F$ near $(\pi, 0)$, (top curve) and close to (π, π) (bottom curve). *Red*: EDCs reflected at $E = 0$ eV. *Black*: Sum of the original and reflected EDC. **(b)**, black markers: Symmetrized EDCs of (a). red line: Top: Fit of a gapped, resolution broadened Lorentzian function the symmetrized EDC datapoints. Here, $\mathrm{Im}\Sigma = \Gamma$, $\mathrm{Re}\Sigma = \Delta^2/\omega$ where Δ denotes the gap amplitude. Bottom: Fit of a resolution broadened Lorentzian (Voigt) curve (bottom red curve) [232].

are, however, displaying different intensities and lineshapes. This demonstrates that from experiment to experiment, different signal-to-background ratios are observed. We stress that this effect is most visible at $p = 0.12$, where spectral weight at $(\pi, 0)$ appears strongly suppressed or redistributed. Once the background intensities are subtracted, the intrinsic lineshape is essentially identical, irrespectively of the signal-to-background ratio - see Fig. 3.2 h). As shown in Figure 3.5 g) - l), only the lineshape at $(\pi, 0)$ of Nd-LSCO with $p = 0.12$ is significantly influenced by the background subtraction. For all other spectra, the background subtraction has little impact on the overall lineshape. In fact, for Nd-LSCO $p = 0.12$ the signal is comparable to the background, whereas for compounds with $p > 0.15$ the signal-to-background ratio is much larger [see Fig. 3.6]. Again, this is an indication that the 1/8 antinodal spectra at $(\pi, 0)$ are anomalous.

3.2.4 EDC analysis

Important information about the physics in a solid (quasiparticle lifetime, gap in the spectral function, etc.) can be extracted by a quantitative analysis of the EDC lineshape. If matrix element effects are neglected the EDC lineshape as a function of energy ω at a fixed momentum $\mathbf{k}$ is derived by equation 2.9:

$$I_{\mathbf{k}}^{EDC}(\omega) \sim f(\omega) \frac{\mathrm{Im}\Sigma_{\mathbf{k}}(\omega)}{[\omega - \varepsilon_{\mathbf{k}} - \mathrm{Re}\Sigma_{\mathbf{k}}(\omega)]^2 + [\mathrm{Im}\Sigma_{\mathbf{k}}(\omega)]^2} \tag{3.1}$$

with $f(\omega)$ denoting the Fermi Dirac (FD) function. The EDC analysis close to E_F is often complicated by the presence of the FD function. However, for an EDC at the Fermi-momentum $\mathbf{k} = \mathbf{k}_F$ a method exists which allows to remove the FD step function from the

EDC. By symmetrizing $I_{\mathbf{k}}^{EDC}(\omega)$ about E_F, $f(\omega)$ is canceled out:

$$\begin{aligned} I_{\rm sym}(\mathbf{k},\omega) = I(\mathbf{k},\omega) + I(\mathbf{k},-\omega) &= I_0(\mathbf{k}_F)f(\omega)A(\mathbf{k}_F,\omega) + I_0(\mathbf{k}_F)f(-\omega)A(\mathbf{k}_F,-\omega) \\ &= I_0(\mathbf{k}_F)f(\omega)A(\mathbf{k}_F,\omega) + I_0(\mathbf{k}_F)[1-f(\omega)]A(\mathbf{k}_F,\omega) \\ &= I_0(\mathbf{k}_F)A(\mathbf{k}_F,\omega) \end{aligned} \tag{3.2}$$

Here, the identity $f(-\omega) = 1 - f(\omega)$ was used and the particle hole symmetry of the system is assumed by using the identity $A(\mathbf{k}_F,\omega) = A(\mathbf{k}_F,-\omega)$. The symmetrizing procedure is illustrated in Fig. 3.3 for an EDC which shows a gap in the single particle spectral function (top curves) and an EDC which is gapless (bottom curve)[2].
For a sufficiently small energy range close to E_F the lifetime can be assumed to be constant $\tau_0^{-1} = \Gamma = {\rm Im}\Sigma(\omega)$. The gapless symmetrized EDC has then a Lorentzian lineshape.
In the case in which the scattering rate Γ is smaller or similar to the instrumental resolution, the peak is described by a Voigt-like profile which is the convolution of the Lorentzian lineshape with the instrumental resolution function $\mathcal{R}(\omega)$ which has usually a Gaussian profile.

$$I_{\rm sym}(\mathbf{k},\omega) = I_0(\mathbf{k})A(\mathbf{k},\omega) \otimes \mathcal{R}(\omega) \tag{3.3}$$

The symmetrized EDC, lower curve in Figure 3.3 b), is fitted to a Voigt profile. In this chapter symmetrized EDCs are used for qualitative and quantitative analysis of the data.

3.3 Results

Normal state ($T \gtrsim T_c$) energy distribution maps taken in the (π,0)-region of Nd-LSCO $x = p = 0.12$, 0.15, 0.20, and 0.24 are shown in Figure 3.4. As doping p is reduced, the "quasiparticle" excitations are gradually broadened. Finite spectral weight at the Fermi level E_F ($\omega = 0$) is, however, found for all compositions even deep inside the charge stripe ordered phase [236]. It is thus possible to define the underlying Fermi momenta k_F from the maximum intensity of the momentum distribution curves (MDC) at $\omega = 0$. The Nd-LSCO Fermi surface topology [237], shown schematically in Figure 3.4, is similar to that of $La_{2-x}Sr_xCuO_4$ (LSCO) [171, 238] and Bi2212 [239, 240]. A van-Hove singularity crosses E_F at a doping concentration slightly larger than $x = p = 0.20$, separating electron- from hole-like Fermi surfaces.

3.3.1 Spectral lineshapes

Analysis of symmetrized energy distribution curves (EDCs) at $k = k_F$ is a standard method to visualize the existence of a spectral gap near the Fermi level [84]. A single-particle gap shifts the spectral weight away from the Fermi level and hence produces a double peak structure in the symmetrized curves. In absence of a spectral gap, the symmetrized EDC at k_F is on the contrary characterized by a lineshape peaked at the Fermi level. For overdoped LSCO and Nd-LSCO $p \sim 0.24$, the spectra at $(\pi, 0)$ have a Voigt-like profile [see top spectrum of Figure 3.5 a), b)] just above T_c, suggesting resolution limited gapless excitations. At slightly lower doping in Nd-LSCO $p = 0.20$, a clear spectral gap $\Delta \sim 25-30$ meV is found in the region at $(\pi, 0)$ for $T \sim T_c$ [Fig. 3.5 b)]. Similar line-shapes of the ARPES spectra were obtained on Nd-LSCO $p \sim 0.15$ and LSCO with $p = 0.105, 0.12$ and 0.15, see Fig. 3.5 a), b). As in Bi2212 and Bi2201 [241–243], a dramatic change of the line shape at $(\pi, 0)$ appears for underdoped Nd-LSCO [Fig. 3.5 b)]. The peaked lineshape structure – found for Nd-LSCO $p = 0.15$ and 0.20 – is strongly depleted.

A similar evolution of the line-shape is found when moving from the $(\pi, 0)$ to the (π, π) region in Nd-LSCO at $p = 0.12$ [Fig. 3.5 c)]. It resembles the doping dependence [Fig. 3.5 b)]: first the double-peaked structure is recovered and second, upon entering the Fermi

[2] In the field of cuprate research this method is commonly applied [232–235].

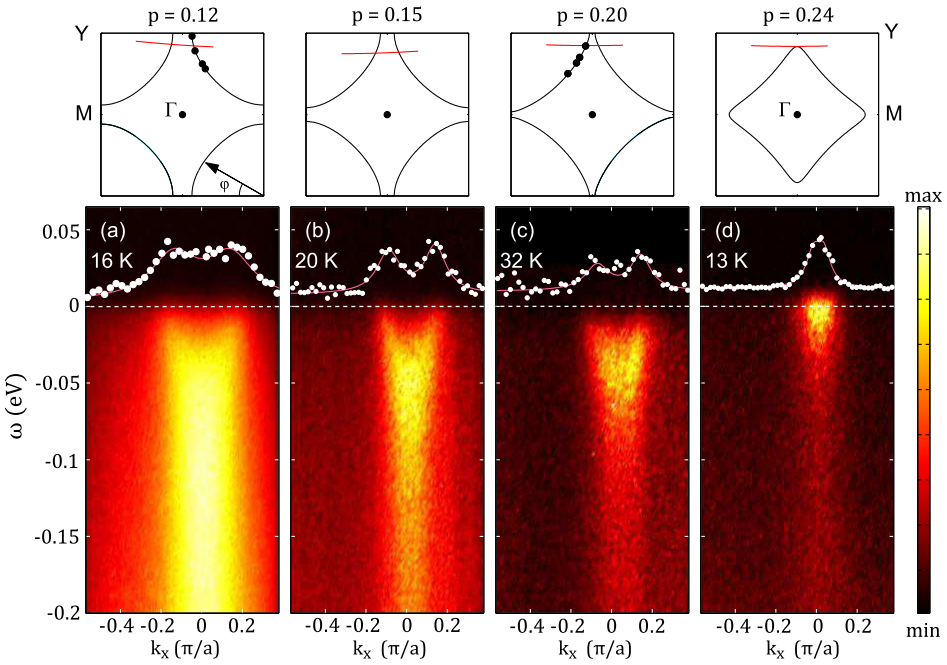

Figure 3.4: (a) - (d) Angle-resolved photoemission spectra at $(\pi, 0)$, taken in the normal state of $La_{1.6-x}Nd_{0.4}Sr_xCuO_4$ for different dopings $p = x$ as indicated. Solid white points are momentum distribution curves at the Fermi level, indicated by horizontal dashed lines. Top panels schematically show the Fermi surface topology for each of the doping concentrations. The red lines indicate the trajectory along which the spectra at $(\pi, 0)$ were recorded. Solid black points indicate the underlying Fermi momenta at which symmetrized EDCs are shown in 3.5 c) - d).

arc, gapless excitations are found [236]. For comparison, the momentum dependence of the EDC lineshapes in Nd-LSCO $p = 0.20$ is shown in Figure 3.5 d). At this doping, a peaked structure is found for all underlying Fermi momenta [see Fig. 3.5 d)]. The temperature dependence of spectra at $(\pi, 0)$ are also very different in Nd-LSCO $p = 0.12$ and 0.20 – see Fig. 3.5 e), f) and 3.6. For $p = 0.20$, the normal state gap closes at $T \approx 80$ K, while it persists in the stripe order $p = 0.12$ compound. Furthermore, the peaked structure in the symmetrized EDC lineshape becomes more pronounced in $p = 0.20$ upon cooling [Fig. 3.5 f)]. The opposite trend is observed at 0.12 doping. In fact, as in Bi2201 [241], a much sharper line-shape at $(\pi, 0)$ is found at 75 K compared to 17 K. Finally, the spectral gap in $p = 0.20$ seems to conserve but redistribute the spectral weight [Fig. 3.6] as it opens upon cooling. In contrast, for underdoped Nd-LSCO $p = 0.12$, spectral weight is either lost or redistributed in a non-trivial fashion upon cooling. The spectra at $(\pi, 0)$ of the anomalous 1/8 doping are thus behaving very differently from what is found in more overdoped samples of Nd-LSCO. The 1/8 spectra at $(\pi, 0)$ are also very different from what is observed in LSCO at similar doping [Fig. 3.5].

3.4 Discussion

3.4.1 Lineshape modelling

Lets start by discussing the spectra on the overdoped side of the phase diagram. Neglecting matrix element effects, the symmetrized intensity $I(k_F, \omega)$ is given by the spectral function [84]

$$A(k_F, \omega) \sim -\mathrm{Im}\Sigma/[(\omega - \mathrm{Re}\Sigma)^2 + \mathrm{Im}\Sigma^2]. \tag{3.4}$$

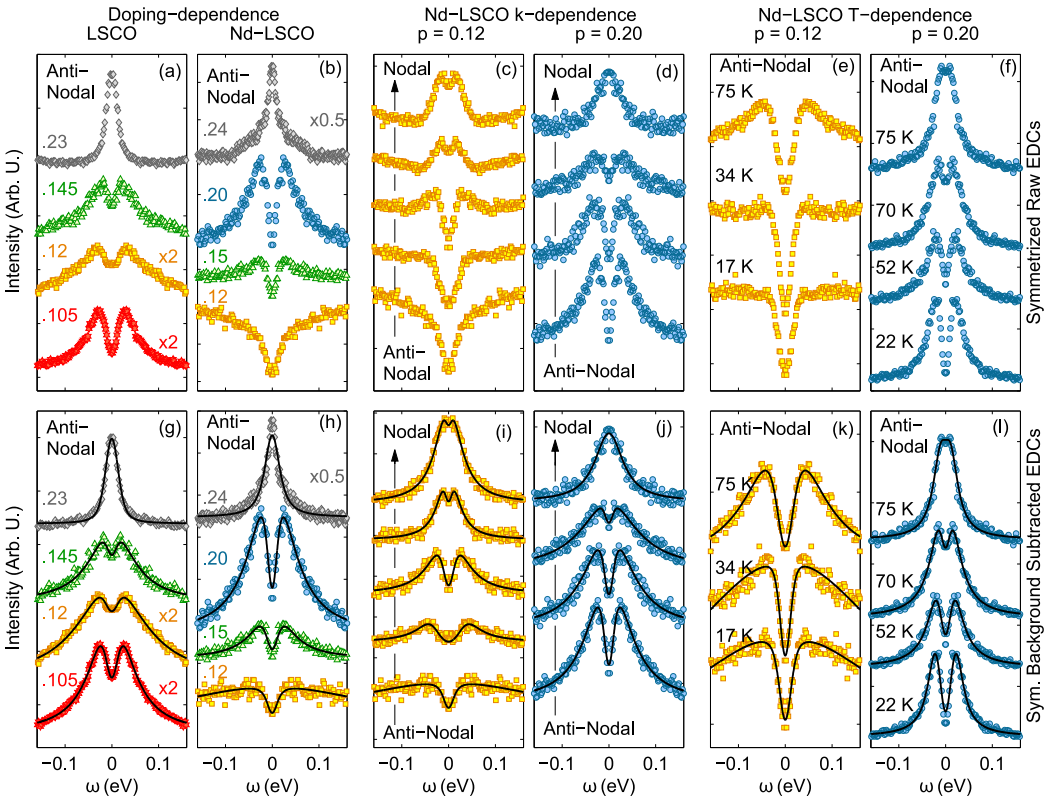

Figure 3.5: Symmetrized normal state energy distribution curves (EDCs) recorded on $La_{2-x}Sr_xCuO_4$ (LSCO) and $La_{1.6-x}Nd_{0.4}Sr_xCuO_4$ (Nd-LSCO). All spectra were taken just above T_c. In top panels **(a)** - **(f)** are raw symmetrized spectra while in bottom panels **(g)** - **(l)** are background subtracted spectra. **(a)** - **(b)** Symmetrized EDCs taken in the region at $(\pi, 0)$, for doping concentrations of LSCO and Nd-LSCO as indicated. ARPES data on LSCO $x = 0.105$ and 0.145 were previously presented in Ref. [233, 234, 244] and all LSCO samples were characterized by neutron scattering experiments [245–247]. **(c)** - **(d)** Momentum dependence of symmetrized energy distribution curves (EDCs) taken at k_F moving from $(\pi, 0)$ (bottom) to at (π, π) (top) region for Nd-LSCO $p = 0.12$ and 0.20. **(e)** - **(f)** Temperature dependence of symmetrized EDCs recorded on Nd-LSCO $p = 0.12$ and 0.20 at $(\pi, 0)$. For clarity, each spectrum has been given an arbitrary vertical shift. Solid lines in bottom panels are fits, see text for an explanation.

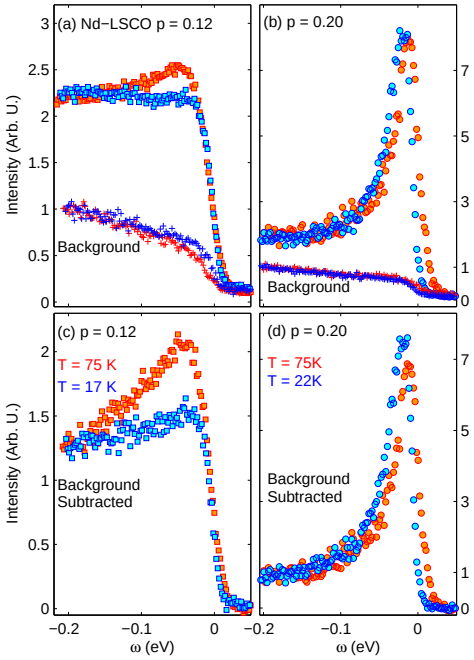

Figure 3.6: Comparison of spectra at $(\pi, 0)$ at $T \sim 20$ K (blue) and 75 K (red). **(a)** and **(b)** show raw energy distribution curves recorded at k_F on Nd-LSCO $p = 0.12$ and 0.20 with the respective background intensities, measured at momenta far from k_F. In **(c)** and **(d)**, the respective background subtracted curves are compared.

In absence of a spectral gap, $\mathrm{Re}\Sigma = 0$ at $k = k_F$ and the spectral function is nothing else than a Lorentzian function, when approximating $\mathrm{Im}\Sigma$ by a constant Γ. If $\mathrm{Im}\Sigma = \Gamma$ is comparable to the applied energy resolution, a Voigt lineshape is effectively observed. This is the case for spectra at $(\pi, 0)$ of Nd-LSCO $p = 0.24$ [Fig. 3.5 h)]. The intrinsic linewidth Γ is a measure of the "quasiparticle" scattering. With increasing scattering, the linewidth broadens (Γ increases) and the peak amplitude – sometimes referred to as the "quasiparticle residue Z" – is lowered. In this fashion, a metal can loose its coherence.

In presence of a spectral gap, Eliashberg theory applied to the normal state finds the Green's function $G(k_F, \omega) = [(\omega + i\Gamma) - \Delta^2/(\omega + i\Gamma)]^{-1}$ to be given by two parameters: the gap Δ and the scattering rate Γ [248]. This functional form mimics roughly the observed lineshape, but does not provide a fulfilling description of the experimental spectra. We therefore adopted a simpler phenomenological Green's function, $G(k_F, \omega) = [(\omega + i\Gamma) - \Delta^2/\omega]^{-1}$, that contains the same two parameters and has previously been used to analyze symmetrized energy distribution curves [206, 232–235, 249]. The spectral function $A(k_F, \omega) = \pi^{-1}\mathrm{Im}G(k_F, \omega)$ can now be expressed by two dimensionless quantities,

$$A(x) \sim \frac{1}{\Delta} \frac{\gamma}{(x - 1/x)^2 + \gamma^2} \tag{3.5}$$

where $x = \omega/\Delta$ and $\gamma = \Gamma/\Delta$. This phenomenological spectral function preserves the Lorentzian lineshape and total spectral weight, but shifts the peaks to $x = \pm 1$ ($\omega = \pm\Delta$) while the linewidth Γ/Δ is renormalized by the spectral gap. For a fixed gap Δ, increasing quasiparticle scattering still leads to a broader line and weaker peak amplitude. Absence of a peaked structure may therefore be a signature of strong quasiparticle scattering.

3.4.2 Spectral gap and scattering

Using Eq. 2, analysis of background subtracted spectra [250, 251] was carried out. Resolution effects are modelled by Gaussian convolution of the model function $A(k_F, \omega)$ (Eq. 1 and 2). In this fashion, Γ and Δ were extracted along the underlying Fermi surface of Nd-LSCO $p = 0.20$. As shown in Figure 3.7, a correlation between the gap Δ and the scattering rate Γ is found. A similar trend is observed when the gap Δ is weakened by increasing temperature in Nd-LSCO $p = 0.20$. This relation between the gap at $(\pi, 0)$ (usually referred to as the pseudogap) and electron scattering is consistent with previous observations. It is, for example, established that the pseudogap is largest near the zone boundary [84, 205, 209]. At the same time, the scattering rate Γ has been shown to increase when moving from (π, π) to $(\pi, 0)$ regions [252, 253]. Furthermore, the photoemission lineshape broadens and the pseudogap increases when doping is reduced from the overdoped side of the phase diagram [242]. The same trend has been reported by STM studies of the density-of-states [254, 255]. The exact experimental relation between scattering and pseudogap (normal state gap) has, however, not been discussed much [256]. A correlation between scattering and the spectral gap has previously been predicted by dynamical mean-field theory (DMFT) calculations for the Hubbard model [257]. Within the DMFT approach [258–261], the pseudogap emerges from electron correlations as a primary effect that, in turn, enhances the tendency for the system to undergo superconducting and charge-density-wave instabilities, at lower temperatures. Notice that, as opposed to superconductivity, charge order has not yet been found directly in DMFT calculations.

From a different point of view, the pseudogap (normal state gap) emerges as a precursor to superconductivity [205, 206, 262], or as a precursor to an order competing with superconductivity [222, 241, 263–265]. In Bi2201, for example, the charge ordering onset temperature is comparable to the pseudogap temperature scale T^* [222]. Furthermore, a connection between the charge ordering vector and the vector nesting the Fermi arc tips was found [222]. It is therefore a possibility that the pseudogap is related to fluctuating CDW order. In two-dimensional CDW systems, spectral gaps are indeed observed above the CDW onset temperature [266, 267]. In cuprates, however, the single particle gap originating from CDW order has not been clearly elucidated by ARPES experiments.

3.4.3 Spectral gaps at 1/8 doping

It is interesting to discuss the spectral lineshapes at the 1/8-doping, where the charge order parameter has its maximum [Fig. 3.1]. Charge order – in principle – should open a single-particle gap somewhere on the Fermi surface [268, 269]. It is commonly assumed that the stripe ordered ground state found in Nd-LSCO is identical to that of $La_{2-x}Ba_xCuO_4$ (LBCO) and $La_{1.8-x}Eu_{0.2}Sr_xCuO_4$ (Eu-LSCO) with $p = x \simeq 1/8$ [270]. All three systems have the same low-temperature tetragonal crystal structure, similar thermopower [271, 272], and the same spin/charge stripe structure [273–276]. At the particular 1/8 doping – due to phase competition – charge stripe order suppresses almost completely superconductivity. ARPES studies on these stripe ordered systems commonly report spectra with little low-energy spectral weight at $(\pi, 0)$ [231, 236, 277–279]. Different interpretations have been put forward [231, 277]. In LBCO it was suggested that the pseudogap (normal state gap) has d-wave character and that the gap amplitude Δ is maximized at 1/8-doping [231] (this result is reproduced in Fig. 3.1 c). Subsequent experiments reported a correction to the d-wave symmetry [277]. This led to the proposal of a two-gap scenario [280–282], with an additional spectral gap (of unknown origin) in the region at $(\pi, 0)$ [277].

In Nd-LSCO $p = 0.12$, Fermi arcs with finite length were found even at the lowest measured temperatures [236]. To access the intrinsic spectral evolution as a function of momentum in Nd-LSCO $p = 0.12$, background subtracted data should be considered. In Figure 3.5 i), spectra near the region of $(\pi, 0)$ and close to the tip of the Fermi arc are compared. Near to the tip, the spectrum resembles that observed in overdoped Nd-LSCO.

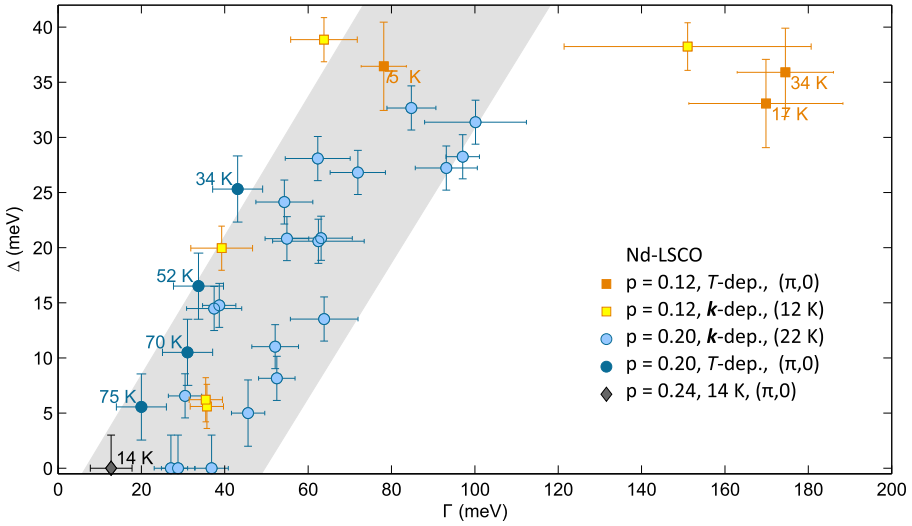

Figure 3.7: Normal state gap Δ versus the scattering rate Γ. Both quantities were extracted by fitting background subtracted symmetrized energy distribution curves along the underlying Fermi surface of Nd-LSCO $p = 0.12$, 0.20 and 0.24, as well as spectra at $(\pi, 0)$ versus temperature. The fitting procedure is explained in the text. Gray shaded area indicates schematically the correlation between the normal state gap and the electron scattering.

Fitting to Eq. (2) yields $\Delta = 20 \pm 2$ meV and a scattering constant $\Gamma = 39 \pm 8$ meV. This is consistent with the approximate constant ratio of Δ/Γ [see Fig. 3.7] found for Nd-LSCO $p = 0.20$. The lineshape of the spectra at $(\pi, 0)$ is, however, dramatically modified. A similar evolution was found in LBCO [277]. It seems that the system has lost coherence. Fitting using Eq. 2, indeed yields much smaller ratios of Δ/Γ – see Fig. 3.7. Thus, a sudden quasiparticle decoherence effect is one possible explanation for the different lineshape at $(\pi, 0)$ observed in the underdoped regime.

3.4.4 Effects of competing orders

Next, we discuss the possible influence of static long-range charge density-wave order. For conventional CDW systems, the order parameter is identical to the single-particle gap [283], and Δ_{ch} scales with the lattice distortion u [283]. By measuring this distortion using hard x-ray diffraction, it was found that Δ_{ch} has a strong doping dependence [89] (reproduced in Figure 3.1 b)) – peaking sharply at the 1/8-doping. Just a slight increase of doping, to $p = 0.15$, results in a single-particle gap Δ_{ch} renormalized by a factor of five [89] (compared to 1/8-doping). Notice that the charge stripe onset temperature T_{ch} – observed by x-ray diffraction – varies more smoothly with doping. Hence, the coupling constant $\alpha = \Delta_{ch}/k_B T_{ch}$ has a strong doping dependence – being largest at 1/8 doping. It is also around this doping that quantum oscillation [284–287] and transport [219, 271, 288, 289] experiments have revealed the Fermi surface reconstruction in YBCO and Hg1201. Charge ordering has been proposed as the mechanism responsible for this reconstruction [220, 288]. Hence, strongly coupled charge order is not necessarily in contradiction with the observation of quasiparticles with light masses. Interestingly, neither the Fermi surface reconstruction nor the effect of charge order have been convincingly probed by photoemission spectroscopy.

The observation of an electronic Fermi surface reconstruction is complicated by orthorhombic distortions, that fold the bands similarly to what is expected from density-wave orders [290–292]. Moreover, identification of charge density wave order effects on the lineshape at $(\pi, 0)$ in very underdoped compounds is complicated by superconductivity, pseudogaps and possibly also spin-freezing phenomena [293, 294]. The choice of Nd-LSCO ensures,

due to it's low T_c, that superconductivity is not influencing the problem. Furthermore, in this system spin and charge density wave orderings are coupled [88], and hence part of the same phenomenon.

When a spectral gap Δ opens, low-energy spectral weight is either suppressed or redistributed in (k, ω)-space. It has, for example, been shown that in Bi2212, pronounced redistribution of spectral weight – extending beyond 200 meV – appears inside the pseudogap [265]. In Figure 3.6 b), spectra at $(\pi, 0)$ of Nd-LSCO $p = 0.20$ display how the normal state gap opens upon cooling. As the gap opens, spectral weight is transferred to larger energies, while the total amount of spectral weight remains approximately constant. This rearrangement of spectral weight manifests itself within an energy scale $(2-3)\Delta < 100$ meV. In the region of $(\pi, 0)$ of stripe ordered Nd-LSCO $p = 0.12$, within the same temperature and energy window, the behavior is very different [see Fig. 3.6 a)]. Upon cooling, low-energy ($\omega < 100$ meV) spectral weight is removed with an apparent net loss of total weight. The $k-$dependence in Figure 3.5 c), i), does not suggest any pile up of spectral weight at other locations in momentum space. Thus either spectral weight is transferred to $\omega > 5\Delta$, or it is simply not conserved. A system that undergoes a phase transition may not display spectral weight conservation. Appearance of charge stripe order in the low-temperature tetragonal crystal structure may therefore lead to effective loss of spectral weight. In that case, stripe order seems to influence mainly the region at $(\pi, 0)$ and, remarkably, suppression of spectral weight extends up to energies as large as 100 meV.

3.5 Conclusions

In summary, we have presented a systematic angle resolved photoemission spectroscopy, normal state study of the charge stripe ordered cuprate compound $La_{1.6-x}Nd_{0.4}Sr_xCuO_4$ (Nd-LSCO). By varying the doping concentration, spectra at $(\pi, 0)$ were recorded from the overdoped metallic phase to the 1/8-doping – where static charge stripe order is stabilized. The metallic phase is characterized by gapless excitations even in the region at $(\pi, 0)$. At $x = 0.20$, a spectral gap $\Delta \approx 30$ meV opens in the region at $(\pi, 0)$ but spectral weight remains conserved, although shifted to slightly larger energies. Analysis of the line shape suggests a correlation between electron scattering and the gap amplitude. Finally, for underdoped compounds the lineshape at $(\pi, 0)$ is quite different. Upon cooling into the stripe ordered phase, spectral weight appears to be lost. An additional source for spectral weight suppression is therefore proposed, and charge stripe order is discussed as an underlying mechanism. Parts of the this chapter have been published in Matt *et al.* [167].

Chapter 4

$NaFe_{0.56}Cu_{0.44}As$: A pnictide insulating phase induced by on-site Coulomb interaction

4.1 Introduction

Similar to the cuprates and iron-chalcogenides, in the phase diagram of the iron-pnictides a superconducting dome develops upon doping a non-superconducting, often magnetically ordered, parent compound. The superconducting dome and/or magnetic phase are formed from an underlying normal state which exhibits bad-metal behavior with large electrical resistivity at room temperature [34, 109, 120, 121]. It has been proposed that the proximity to a Mott insulating phase is responsible for the bad metal behavior and increase in the electronic correlations in those compounds [121, 122]. In the studies of iron-chalcogenides, it has also been suggested that the (orbital-dependent) Mott physics plays a key role in the mechanism for the insulating behavior. In cuprates, electron-electron correlations are reduced by doping either electrons or holes into the Mott insulating parent compound, with superconductivity occurring at a few percent of doping [30, 81, 167]. In contrast, correlation effects in the iron-pnictides are only weakened with the electron doping, but enhanced when doping holes into their parent compounds [126, 127, 295, 296]. However, for all the iron-pnictides, even up to the highest possible hole-doping level (e.g. fully replacing Ba with K in the widely studied $Ba_{1-x}K_xFe_2As_2$), an antiferromagnetically (AFM) ordered insulating state does not occur [295, 297]. It would be highly interesting to identify and investigate an iron-pnictide family that undergoes an AFM insulating – (bad) metallic – superconducting phase transition tuned by doping, and study these compounds' electronic structures in distinct phases.

Very recently, it has been shown that, adjacent to the superconducting phase, an AFM insulating state occurs in heavily doped $NaFe_{1-x}Cu_xAs$ [299, 300]. For $x > 0.3$, below $T_N = 200$ K the system develops antiferromagnetic order which becomes long-range for $x \geq 0.44$. The spin arrangement is depicted in Figure 4.1 c), with a magnetic moment $\sim 1.1\mu_B$ per iron site, ten times larger than that in the parent compound NaFeAs. Using angle-resolved photoemission spectroscopy (ARPES), combined with density functional theory (DFT) and DFT+U calculations, we reveal that in $NaFe_{1-x}Cu_xAs$, with high x values ($x = 0.44$), the Hubbard U and Hund's coupling (J_H) have a strong effect on the underlying electronic structure, which results in a finite energy gap occurring at the Fermi level (E_F). The ARPES results are significantly different from the electronic structure obtained from DFT calculations, but can be reproduced by DFT+U calculations with the inclusion of U and J_H to account for the on-site Coulomb interaction. We show that the main effect of the

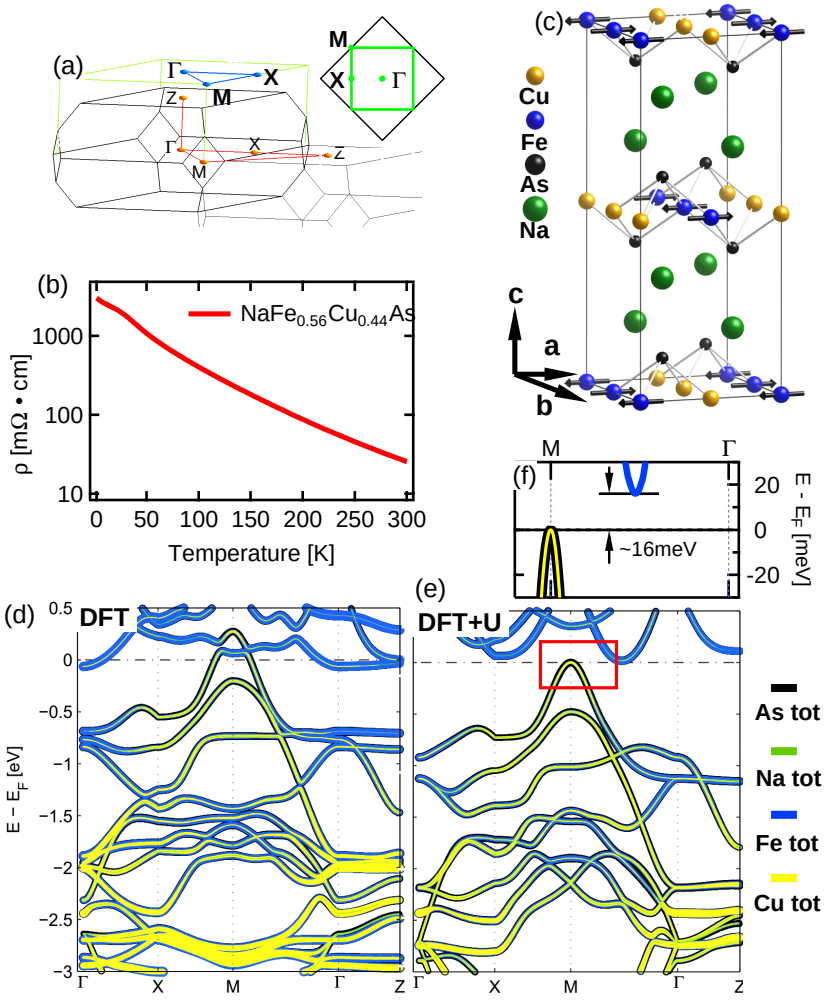

Figure 4.1: Electronic structure of $NaFe_{0.5}Cu_{0.5}As$, as calculated by DFT and DFT+U. **(a)** Brillouin zone (BZ) with high symmetry points and lines indicated by red lines. The light green line indicates the projected BZ. Inset: Light green lines denote the projected BZ of $NaFe_{0.56}Cu_{0.44}As$; black lines the BZ of the 2-Fe unit-cell of $BaFe_2As_2$ as defined in [119, 125]. **(b)** Temperature dependence of the in-plane resistivity for $NaFe_{0.56}Cu_{0.44}As$. **(c)** The crystal structure [298]. **(d), (e), (h), (i)** The band structure along high symmetry lines from DFT and DFT+U calculations, respectively. **(k)** Zoom-in of the red box in i), showing the bandgap about E_F.

interactions is to shift the Fe $3d$ orbital-related bands to higher binding energies, which results in the ground state of $NaFe_{0.56}Cu_{0.44}As$ being an insulator.

4.2 Methods

ARPES experiments were carried out at the Surface and Interface Spectroscopy (SIS) beamline [194], Swiss Light Source (SLS). The measurement was performed on freshly cleaved samples which have been cleaved in-situ under ultrahigh vacuum (UHV) conditions ($< 5 \cdot 10^{-11}$ mbar) by a top post method. During the whole experiment the pressure in the analysis chamber was kept below $< 5 \cdot 10^{-11}$ mbar in order to avoid surface contamination. The

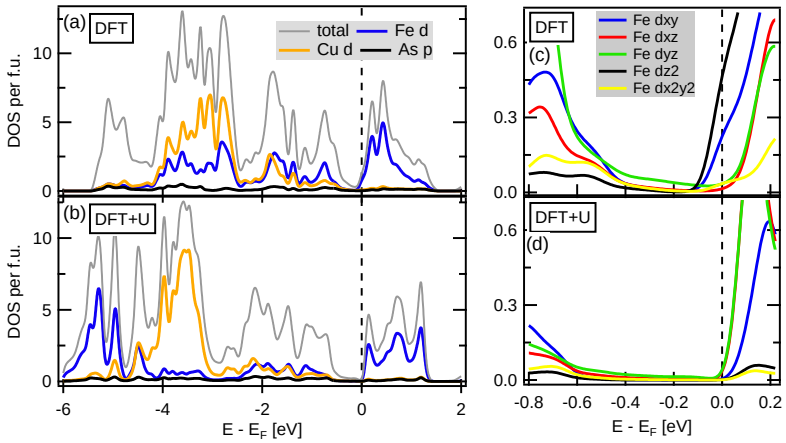

Figure 4.2: The electronic structure of $NaFe_{0.5}Cu_{0.5}As$ from DFT and DFT+U calculations. **(a)** and **(b)** Total and partial density of state (DOS) with different atomic and orbital characters from DFT and DFT+U calculations, respectively. **(c)** and **(d)** The partial DOS of different Fe $3d$ orbitals in the vicinity of E_F, obtained from DFT and DFT+U calculations, respectively.

ARPES spectra were recorded with a Scienta R4000 electron analyzer with total energy and angular resolutions of better than 20 meV and 0.15°, respectively. The Fermi level was determined by recording the photoemission spectra from polycrystalline copper on the sample holder. The ARPES spectra have been normalized by similar methods as described in chapter 3.

The calculations were performed using the WIEN2K package [159] with the crystal structure shown in Figure 4.1 a) and the lattice parameters ($a = b = 5.72$ Å, $c = 13.85$ Å) determined from neutron diffraction on $NaFe_{1-x}Cu_xAs$ ($x = 0.44$) [299]. In the calculations, the Kohn-Sham equation is solved self-consistently by using a full-potential linear augmented plane wave (LAPW) method. The exchange-correlation term is treated within the generalized gradient approximation (GGA) in the parametrization of Perdew, Burke and Enzerhof (PBE) 96 [301]. In the DFT+U calculations, a Hubbard $U = 3.15$ eV was used with Hund's coupling $J_H = 0.4$ eV in the self-interaction correction (SIC) formalism incorporated in the WIEN2K package [302, 303]. The U and J_H values used in this work have been deduced by constrained-RPA approach as average values of LiFeAs, representing the 111 family [128]. Hence, we assume that these values are justified for $NaFe_{1-x}Cu_xAs$. The ARPES measurement were performed on $NaFe_{0.56}Cu_{0.44}As$, however it is much easier to perform the calculation for the $NaFe_{0.5}Cu_{0.5}As$. Neutron diffraction data has shown that the lattice parameters depend only weakly on x, (for x close to 0.5). Therefore, the difference in the electronic structure between $x = 0.44$ and $x = 0.5$ is presumed to be uncritical [299].

4.2.1 Acknowledgements

All high quality single crystals of $NaFe_{1-x}Cu_xAs$ with $x = 0.44$ have been grown using the self-flux method by Yu Song, P.C. Dai, Chongde Chao, Department of Physics and Astronomy, Rice University, Houston, Texas 77005, USA and Department of Applied Physics, Northwestern Polytechnical University, Xian 710072, China. The single-crystal growth method has been described in [300, 304] which is similar to the procedure for the growth of $NaFe_{1-x}Co_xAs$. The doping levels were determined by inactively coupled plasma (ICP) atomic-emission spectroscopy as described in Ref. [299] and references therein. Resistivity measurements have been performed in a physical property measurement system (PPMS). The contacts for the four-point probe have been prepared inside an Ar-atmosphere and cov-

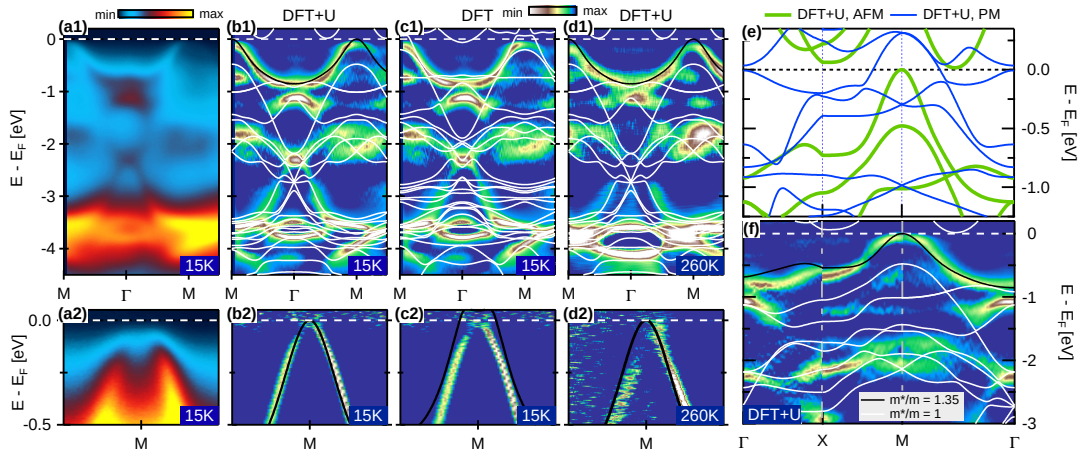

Figure 4.3: ARPES spectra of $NaFe_{0.56}Cu_{0.44}As$. **(a1), (a2)** ARPES spectrum along M-Γ-M direction, taken at $T = 15$ K with $h\nu = 52$ eV, circularly polarized photons. **(b1), (b2)** respectively **(c1), (c2)** Curvature plot of the ARPES spectra in (a1), respectively (a2). The superimposed lines are the band dispersion from DFT+U and DFT calculations, as indicated. The calculated dispersion drawn in black is renormalized by a factor of 1.35. White lines represent non-renormalized bands. **(d1), (d2)** The same as (b1), (b2) but the ARPES spectrum is obtained at $T = 260$ K. **(e)** Band dispersion as calculated by DFT+U for the AFM (green lines) and paramagnetic state (blue lines). **(f)** Curvature plot of the ARPES spectrum at $T = 15$ K along high symmetry lines as indicated in Figure 4.1 a). The superimposed lines are the band dispersion from DFT+U calculation.

ered by Apiezon N grease in order to avoid degradation of the air- respectively water-sensitive samples. No visual deterioration of the samples has been observed under a microscope after the resistivity measurement. We would like to thank the sample growers for supplying high quality single crystals.

4.3 Results

4.3.1 Electronic structure calculations by DFT and DFT+U

To get more insight into the insulating behavior of $NaFe_{0.56}Cu_{0.44}As$ at low temperatures, as observed in the transport measurements [Fig. 4.1 b)] and Refs. [299, 300], we have performed electronic structure calculations without and with on-site correlations by using DFT and DFT+U methods, respectively. The DFT calculation predicts a semi-metallic state with an electron-like pocket at Γ (Fe character) and a hole-like pocket around M (Cu-As character); see Fig. 4.1 d). These pockets produce a finite density of states (DOS) at E_F [Fig. 4.2], which is inconsistent with the insulating behavior of $NaFe_{0.56}Cu_{0.44}As$. On the other hand, if U and J_H are included in the calculations (DFT+U), the valence bands get pushed to higher binding energies and the conduction bands are shifted up, resulting in a finite energy gap between valence and conduction bands [Figs. 4.1 e) and f)]. The magnitude of the band shift depends strongly on the elemental and orbital composition of the bands; it is negligible for the Cu- and As-derived bands but large for the bands formed by Fe 3d orbitals. Among the Fe 3d orbitals, the on-site Coulomb interaction has the strongest effect on d_{xy}-and d_{z^2}-orbital dominated energy bands. Similar to the case of $BaCu_2As_2$ [305, 306], the DFT-band near E_F around the M point is formed by the hybridization of As 4p and Cu 3d orbitals with Fe 3d orbitals [see Figure 4.2]. The inclusion of on-site Coulomb interaction lifts the hybridization, pushing the Cu-As band below E_F and shifting the Fe band above E_F.

4.3.2 ARPES results

Figure 4.3 shows ARPES spectra and their curvature plots along the high symmetry lines in the Brillouin zone (BZ), see Fig. 4.1 a). The overlaid lines are the calculated band dispersion renormalized by a factor of 1.35. The overall agreement between the ARPES spectra and the calculated DFT+U electronic structure is significant: (1) No electron-like pocket around Γ was observed near E_F, which is consistent with the predication by DFT+U calculations and different from that of DFT. (2) Moving from the Γ or X point to the M point, the band approaches but does not cross the Fermi level, thus no hole-like pocket around the M point is formed. (3) At high binding energies, the ARPES results agree better with DFT+U than with DFT. For example, the multiple flat Fe/Cu-derived bands at $\omega = E - E_F \sim -3$ eV in the DFT calculations were not observed by ARPES [Fig. 4.3 c)]. We would like to point out that in contrast to the DFT calculations on the majority of iron pnictides, no shift of individual bands is required in order to match the ARPES results. Our ARPES results reveal that the ground state of $NaFe_{0.56}Cu_{0.44}As$ is an insulator, consistent with the scanning tunneling microscopy (STM) study of heavily Cu-doped $NaFe_{1-x}Cu_xAs$, ($x = 0.3$), which showed diminished density of states at the chemical potential [307]. In Figure 4.3 d), f) we plot the ARPES spectra taken at $T = 260$ K, well above $T_N \sim 200$ K; the dispersion is almost identical to that at low temperatures ($T = 15$ K). However, as shown in Fig. 4.3 e), DFT+U calculation in the paramagnetic state predicts a large, hole-like Fermi surface around M, which is not observed in the ARPES measurement. We would like to emphasize that the local magnetic moment on the Fe sites plays an essential role in order to explain the observed electronic structure below and above T_N.

To further explore the insulating or semi-metallic behavior of $NaFe_{1-x}Cu_xAs$, we have carried out ARPES measurements in several Brillouin zones. Figure 4.4 shows ARPES intensity maps at fixed binding energies. In Figure 4.4 a), b), the intensity map obtained at $T = 15$ K is plotted 25 meV and 300 meV below E_F since the spectral intensity at E_F is vanishing. As expected, except for the (Cu, As)-formed valence band [Fig. 4.3 a), b), e), g)] predicted by the DFT+U calculation, no other band appears at these two energies. The ARPES intensity maps at different binding energies vary little with k_z, indicating that the electronic structure of $NaFe_{0.56}Cu_{0.44}As$ is quasi two-dimensional. These observations are in concert with DFT+U calculations and provide spectroscopic evidence that the system is insulating at low temperatures. In the DFT+U calculations the effect of including U and J_H is to remove the hybridization of As $4p$ and Cu $3d$ with Fe $3d$ orbitals and push the bands dominated by Fe $3d$ orbitals away from the chemical potential. The remaining band near E_F is mainly composed by Cu orbitals [Fig. 4.1 e)]. It has been shown in ref. [299] that the Cu is close to a d^{10} configuration. This could explain why the valence band near E_F is only renormalized by a factor of ~ 1.35 [Fig. 4.3 e)], which is much smaller than the renormalization factor in Fe-pnictide parent or hole-doped superconducting Fe-pnictide compounds (typically $\sim 2 - 4$) whose Fe $3d$ orbitals are partially filled [123, 295, 308, 309]. In Figure 4.4 c), we plot the ARPES intensity map at E_F at $T = 260$ K. Because of broadening, we observe finite spectral weight around M, very similar to the intensity map taken at low temperatures, close to E_F [see Fig. 4.4 a)]. The primary results of our ARPES measurements are the observation of a valence band which is touching, but not crossing the Fermi level. Surprisingly, the observed band dispersion is highly temperature independent and strongly resembles the low-temperature results for temperatures far above T_N.

4.3.3 Lineshape analysis

In heavily doped $NaFe_{1-x}Cu_xAs$, strong suppression of the DOS has been observed by STM measurements for $\omega > -0.2$ eV [307].
The ARPES intensity as function of binding energy is presented in form of an energy distribution curve (EDC) as plotted in Fig. 4.5 e) where spectral weight is integrated over a large momentum window (white lines in panel a). For $\omega < -0.2$ eV, the lineshape is linear and

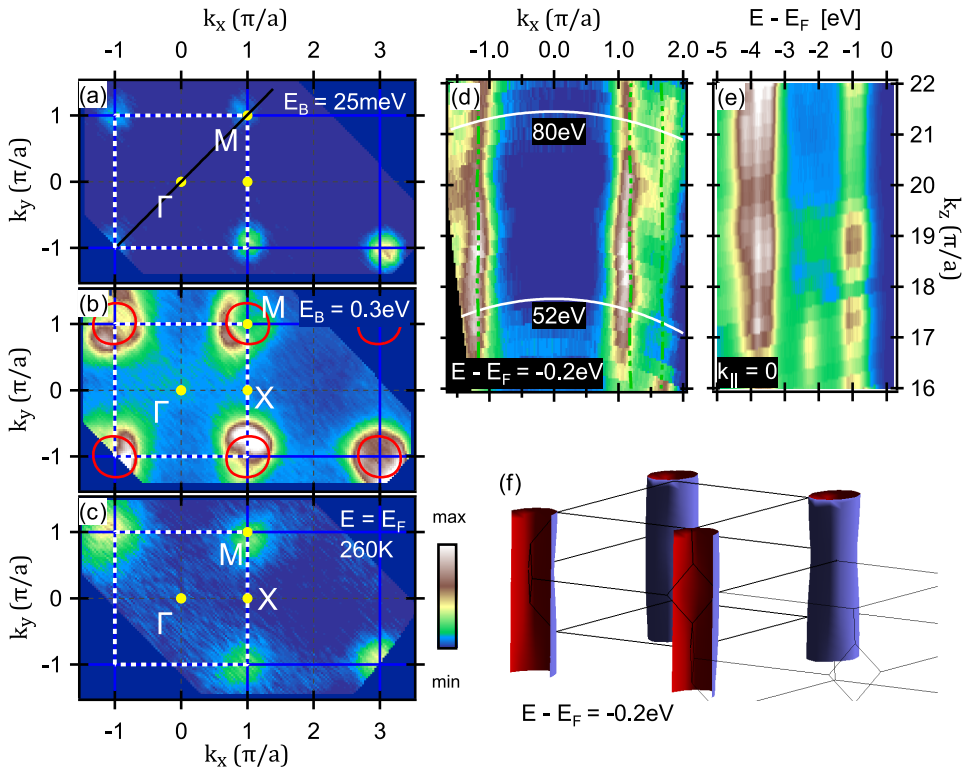

Figure 4.4: **(a)** and **(b)** ARPES intensity maps at energies $\omega = E - E_F = -25$ meV and $\omega = -300$ meV, respectively. The spectra were acquired with $h\nu = 52$ eV, circularly polarized light at $T = 15$ K. The maps have been integrated over an energy window of ± 10 meV. **(c)** ARPES intensity map at E_F, obtained at $T = 260$ K. Due to the thermal broadening, finite intensity appears at the E_F. **(d)** ARPES intensity map at energies $\omega = -200$ meV in the $k_{||}$ - k_z plane, where $k_{||}$ is along $\Gamma - M$ direction. **(e)** The dispersion along k_z direction at $k_{||} = 0$. **(f)** Sketch of the constant energy surface at $\omega = -200$ meV in 3D BZ, calculated by DFT+U method.

above $\omega = \omega_c \equiv -200$ meV enhanced spectral weight suppression is observed, resembling the results of the STM measurements. A similar lineshape evolution is also observed in the peak intensity along the MDC-fitted band dispersion [Fig. 4.5 f)]. Such a suppression of spectral weight is in favor with the insulating behavior of the system and has, for example, been observed below the metal to insulator transition (MIT) in $NdNiO_3$ [310].
The properties of electrons and their interaction in a solid are described by the self-energy $\Sigma = \mathrm{Re}\Sigma + i\mathrm{Im}\Sigma$ [see section 2.2.3]. In Landau Fermi Liquid, the imaginary part, which represents the electron scattering in a material, is given by $\mathrm{Im}\Sigma = \lambda\omega^2$ where λ is the electron coupling constant. $\mathrm{Im}\Sigma$ can be extracted from the experimental ARPES spectrum by the following relation [253, 311]:

$$\mathrm{Im}\Sigma(\omega) = v_{\mathbf{k}}\Gamma_{\mathbf{k}}(\omega) \tag{4.1}$$

where $\Gamma_{\mathbf{k}}(\omega)$ is the half width at half maximum (HWHM) of the MDC [see Fig. 4.5 g), left hand axis]. The imaginary part of the self-energy, $\mathrm{Im}\Sigma(\omega)$, is plotted in Figure 4.5 g), right hand axis. To obtain $\mathrm{Im}\Sigma(\omega)$, the band velocity $v_{\mathbf{k}}$ has been extracted from the renormalized band as calculated by DFT. Similar to the cuprates, $\mathrm{Im}\Sigma$ follows a non-Fermi liquid behavior with $\mathrm{Im}\Sigma = \lambda\omega$ for ω above ω_c, where also spectral weight suppression has been observed [44, 244, 256]. At $T = 15$ K, we extract a coupling constant $\lambda \sim 0.3 \pm 0.03$. Below ω_c, $\mathrm{Im}\Sigma$ is approximately constant. We found that, similar to the band dispersion, also the electron coupling constant λ is not changing between 15 K and 260 K.

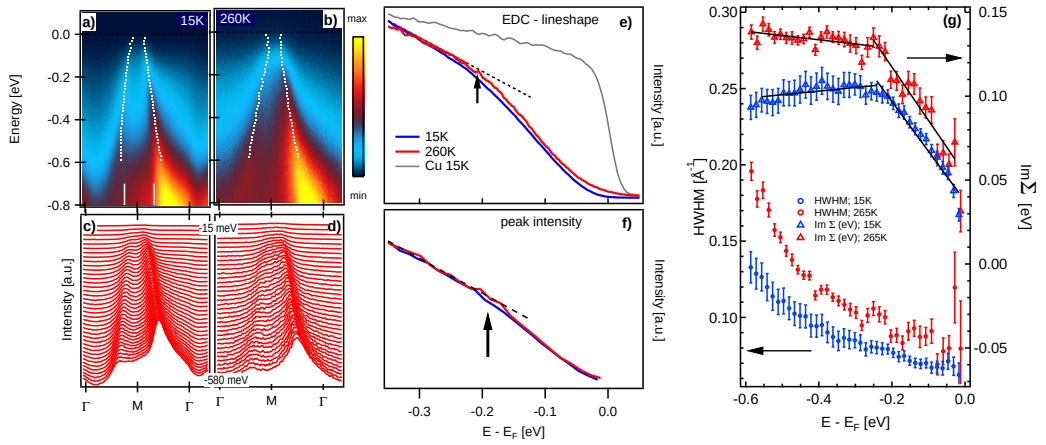

Figure 4.5: Lineshape analysis: **(a), (b)** Raw ARPES intensity spectrum along $\Gamma - M$ as indicated in Figure 4.4 a) for 15 K and 260 K. White dots indicate band dispersion extracted from MDC fits. **(c), (d)** Corresponding MDCs for ω between -15 meV and -580 meV. **(e)** Energy distribution curve (EDC) integrated over region as specified by white lines in panel a) ($\sim \pm 0.1 \text{Å}^{-1}$). **(f)** Peak intensity for right branch of the band around M approaching the Fermi level. **(g)** Left axis: Half width at half maximum (HWHM) $\Gamma_{\mathbf{k}}(\omega, \mathbf{k})$ of MDC curves extracted by fitting MDCs with a Lorentzian lineshape at low and high temperature. Solid lines represent linear fits according to equation 4.1. Right axis: $\text{Im}\Sigma(\omega)$ for low and high temperatures.

4.4 Discussion

Having established that $NaFe_{0.56}Cu_{0.44}As$ is an insulator in the ground state due to correlation effects, we turn to the natural question of how the long-range AFM order disappears at temperatures above the Néel ordering temperature ($T_N = 200$ K), as observed in neutron scattering measurements [299]. In Mott insulators the AFM ordering of local magnetic moments is related to the superexchange energy $J \propto t^2/U$, where t is the hopping integral that scales with the kinetic energy of charge carriers moving in solids [81, 312, 313]. If the on-site Coulomb repulsion exceeds the kinetic energy, the intersite hopping of charge carriers is blocked, causing them to become localized. On the other hand, if the Coulomb energy barrier can be overcome due to a large hopping energy, electrons or holes are delocalized and the long-range AFM ordering is suppressed. It is known that long-range AFM order in a Mott insulator can be suppressed by changing the band filling with chemical doping. For example, in cuprates, at low temperatures, long-range AFM order is destroyed by doping a few percent of holes or electrons into the Mott insulating parent compounds. Note that the Mott gap (or more generally, charge transfer gap) needs not to be suppressed completely for the long-range AFM order to disappear: the insulating Mott state without long-range magnetic order often persists above the Néel temperature [314–316]. This consideration provides a possible explanation for the AFM ordering in $NaFe_{0.56}Cu_{0.44}As$ observed in neutron scattering experiments, as well as its temperature-dependence. Figure 4.6 schematically depicts the DOS of $NaFe_{0.56}Cu_{0.44}As$ in comparison with the parent compounds of cuprates [317]. Due to the on-site Coulombic repulsion, the Fe d orbital-related conduction and valence bands move farther away from the chemical potential. About E_F, a small indirect band gap occurs between the top of the valence band formed by (Cu, As) and the bottom of conduction bands dominated by Fe $3d$ states. In the ground state, the system is insulating: the virtual hopping of electrons with antiparallel spins from one Fe site to the next, restricted

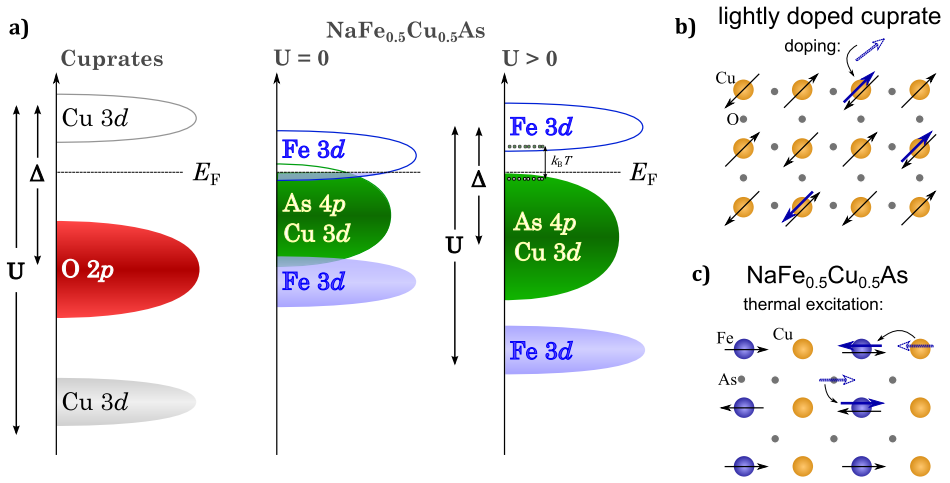

Figure 4.6: **(a)** Schematics of the electronic structure of cuprate parent compounds and $NaFe_{0.56}Cu_{0.44}As$ for the non-interacting case ($U = 0$) and for the case of finite interactions. The quantity $\sim k_B T$ indicates the thermal excitations of electrons from the valence to conduction bands. **(b), (c)** Schematic of a possible real-space Mott scenario for lightly doped cuprates and $NaFe_{0.5}Cu_{0.5}As$.

by the Pauli exclusion principle, leads to the formation of an AFM arrangement in the Fe lattice. Upon increasing temperature, due to the small band gap and thermal excitation, the lowest conduction band starts to be populated by electrons from the highest CuAs valence band, which leaves holes in the valence band [see Fig. 4.6, right panel]. Because the holes (electrons) in the valence (conduction) band are mobile, the resistivity of the material decreases, as manifested in transport measurements [see Fig. 4.1 b)], similarly to thermally activated transport in narrow-band semiconductors. This hopping of the thermally excited electrons in the lowest conduction band [which has Fe $3d$ character, see Fig. 4.1 e), f)] suppresses the long-range AFM-order in the Fe lattice, while the charge gap persists. This is consistent with the non-magnetic insulating behavior of resistivity observed well above the Néel temperature in $NaFe_{1-x}Cu_xAs$ [see Fig. 4.1 b)] [299, 300]. Our ARPES results obtained at $T = 260$ K (well above T_N) show that the band dispersion as well as the band renormalization near E_F are very similar to that at $T = 15$ K (well below T_N) [Fig. 4.3 c) - f)], indicating that there is no significant change in the electronic structure as T_N is crossed. This would suggest that the disappearance of the long-range AFM ordering at $T > 200$ K is indeed related to the occupation of the lowest conduction and highest valence bands, without closing the Mott charge-transfer gap. The robustness of the electronic structure is consistent with transport measurements: upon increasing temperature the resistivity smoothly decreases and the insulating behavior persists at least up to 300 K; no abnormal behavior is observed in the vicinity of T_N ; see Fig. 4.1 b). While not excluding other more sophisticated models (e.g. orbital-selective Mott physics [126, 127, 318]) that would be able to quantitatively account for the experimental results on this material, the basic picture described here provides a qualitatively consistent explanation for the experimental results from neutron scattering, transport and ARPES measurements. This picture in which Mott physics plays a key role for the insulating behavior in highly Cu-doped $NaFe_{1-x}Cu_xAs$ is strongly supported by a recent STM study on insulating $NaFe_{1-x}Cu_xAs$, ($x = 0.3$), which reports striking similarities to lightly doped cuprates [307]. The early ARPES studies on $NaFe_{1-x}Cu_xAs$ with x up to 0.14 showed that, except for introducing extra charge carriers, the overall band dispersion barely changes with Cu doping, and the Fermi surface and/or all the energy bands near E_F are dominated by Fe $3d$ orbitals [319]. It is of high interest to re-

veal the momentum-resolved electronic structure with ARPES in order to get further insight into the evolution of the Cu-3d derived electronic states at or near E_F, as the long-range AFM-ordered insulator evolves into a metallic or superconducting state with decreasing the concentration of the Cu dopant in $NaFe_{1-x}Cu_xAs$.

In addition, strong suppression of spectral weight is observed for $\omega >$ -200 meV on the Cu-As band. Note that a similar suppression of spectral weight in a an equal energy range has been found below the metal to insulator transition (MIT) in $NdNiO_3$ [310]. The electronic spectrum found in scanning tunneling microscope (STM) of heavily Cu-doped $NaFe_{1-x}Cu_xAs$ shows diminishing density of states at the Fermi level, resembling results of lightly doped cuprates close to the parent Mott insulating state [307]. It has been suggested that the suppression of spectral weight which has been found in this STM result and prior ARPES measurements [319] originates from enhanced impurity scattering. The elastic MDC linewidth $\Gamma_0 \equiv \Gamma_{\mathbf{k}}(\omega = 0)$ reflects the strength of impurity scattering. Since we have found a rather sharp linewidth $\Gamma_0 = 0.067\text{Å}^{-1}$, comparable to results from LSCO ($\Gamma_0 = 0.04\text{Å}^{-1}$) [253, 320], we don't consider impurity scattering as the dominant mechanism for the spectral weight suppression. We rather interpret this effect as another sign of strong correlations in the system. Additionally, we suggest that the non-Fermi liquid like behavior which has been observed in the self energy for $\omega > -200$ meV and which resembles the results found in cuprates superconductors is a further manifestation of strong electron correlations in the system [244].

4.5 Conclusion

In summary, using ARPES combined with DFT and DFT+U calculations, we have revealed the electronic structure of the heavily Cu-doped $NaFe_{1-x}Cu_xAs$ ($x = 0.44$) and showed that its ground state is a narrow-gap insulator whose origin lies in strong electron interactions of Fe 3d orbitals. The on-site interaction (Hubbard U and Hunds coupling J_H) remove the hybridizations between Fe 3d and other Cu-As orbitals in the vicinity of E_F. The interactions furthermore elevate the Fe 3d bands near E_F to above the chemical potential and push the fully occupied Fe 3d valence band further down in binding energy. Consequently, an energy gap opens up about the chemical potential, which instigates an insulating phase in the heavily doped $NaFe_{1-x}Cu_xAs$. The effect induced by U and J_H resembles the situation in the parent compounds of the high-T_c cuprates (Mott insulators), with the Mott induced charge transfer gap that underscores the insulating behavior. The quantitative differences to cuprates are that the top of the valence band is derived from CuAs hybridized bands and is very close to (or touching) the chemical potential; and the charge transfer gap between valence and conduction bands is very narrow. The occupation of the Fe 3d conduction band by thermally activated electrons increases the hopping processes between the Fe sites and thus suppresses the AFM ordering, eventually destroying the long-rage order at $T > T_N$. Parts of this chapter have been published in Ref. [321].

4.6 Appendix I: Variation of the electronic structure with the value of U and J_H

Due to the multiorbital nature of the iron pnictides, electronic Coulomb interactions cause not only Mott-type physics but also lead to Hunds exchange coupling [118, 322, 323]. It has been shown that, depending on the global filling in a system, the Hunds coupling can have opposite effects on the Coulomb interaction and electronic mass enhancement. If the system is close to half filling, Hunds coupling enhances electronic correlations and the critical Mott coupling energy U_c which sets the transition to a Mott insulating states is considerably lowered. For lower or higher global filling, the effect of J_H is to push U_c to larger values, i.e. J_H is counteracting to U [126, 322]. However, it has been found that correlations are not

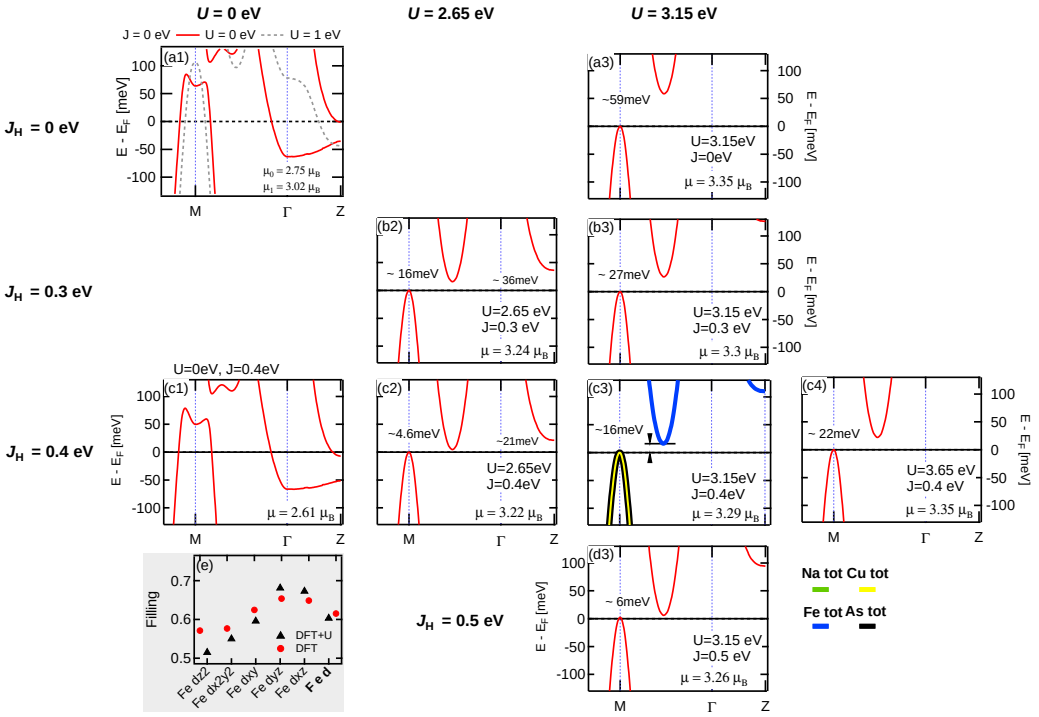

Figure 4.7: **(a) - (f)** Evolution of indirect gap for different values of U and J_{H}. **(a1) - (d3)** DFT+U calculated bandstructure of $NaFe_{0.5}Cu_{0.5}As$ in the vicinity of E_{F} for different values of U (columns) and J_{H} (rows). The indirect gap size and magnetic moment per Fe site is indicated in each panel. **(e)** the filling of the individual Fed orbitals as calculated by DFT and DFT+U ($U = 3.15$ eV and $J_{\mathrm{H}} = 0.4$ eV)

only depending on the global filling but also connected to the filling of individual orbitals [324]. In order to obtain a picture of the role of the interaction parameters U and J_{H} on the formation of the insulating gap, we calculated a series of band structures for a range of U and J_{H} around the reference values $U = 3.15$ eV and $J_{\mathrm{H}} = 0.4$ eV down to $U = 0$ eV and $J_{\mathrm{H}} = 0$ eV. In summary, we observe an opposite effect of U and J_{H}. The gap gets larger when U is increased but shrinks for higher J_{H} [see Fig. 4.7, a1) - d4)]. The integration of the occupied part of the density of states (DOS, Fig 4.7, e) shows that the filling of the individual orbitals is considerably larger than 0.5 (half filling). Therefore the system is in the regime where J_{H} is counteracting to U, which explains the behavior of the insulating gap for the different values of U and J_{H}. As shown by *Song et. al.* [299], the experimental value of ~ 1.1 μB of the ordered Fe magnetic moment of $NaFe_{0.5}Cu_{0.5}As$ is strongly overestimated by the DFT calculations which give a value of ~ 2.77 μB per Fe-site. Our calculations show that the size of the magnetic moment is directly correlated with the size of the insulating ga p. Thus, U and J_{H} have opposite impact on the size of the magnetic moment.

4.7 Appendix II: Comparison of DFT calculations with iron-pnictide compounds

In the studies of iron-based superconductors, first principle DFT calculations are commonly employed as a theoretical guide in the experimental study of the band structure by, for example, ARPES or quantum oscillations. In the metallic and superconducting compounds, it is often found that, in order to match the measured Fermi surface, a particular band which

crosses the Fermi level has to be shifted by a few or several tens of meV. The direction of the shift depends on their position in k-space and on their electron or hole like character [325–329]. Usually the hole like bands around the BZ-center are shifted downwards and the electron like bands at the BZ corner are shifted upwards. Several scenarios have been proposed to account for this behavior (e.g. driven by interactions or due to particle-hole asymmetry), however, more theoretical and experimental work is needed in order to establish a coherent picture. Our combined ARPES and DFT+U study on $NaFe_{0.5}Cu_{0.5}As$ indicates that, close to the chemical potential, the observed energy bands are CuAs-derived and the correlation effect of the electronic states associated with these bands is much weaker than that in most metallic iron-pnictides in which the Fermi surface is formed by Fe $3d$ orbitals. The absence of any band-shift near the chemical potential in $NaFe_{0.5}Cu_{0.5}As$ would suggest that the band shift near the Fermi level as observed in some metallic iron-pnictides is related to the strength of interactions among electrons.

Chapter 5

Effect of As-chain layers on electronic structure in the '112' iron-pnictide family

5.1 Introduction

Since the discovery of high-temperature superconductivity in layered iron-pnictide compounds, the importance of electronic correlation for superconductivity has been one of the focuses of many experimental and theoretical studies [122, 126, 127, 321, 324, 330]. It has been found that the multi-orbital low energy electronic states formed in the FeAs layer are moderately correlated due to finite Hund's coupling and on-site Coulomb interaction. Correlated electrons have an enhanced effective mass which is, in the case of the parent compound $BaFe_2As_2$, by a factor of $m^*/m = 2 - 3$ larger than the free electron mass. Starting from such a representative compound, the effect of charge carrier doping and chemical pressure on the correlation strength has been extensively investigated theoretically and experimentally [122, 123, 295, 296, 330–332]. It has been found that, while electronic correlation is suppressed by isovalent substitution or electron doping it stays constant or is even slightly enhanced when holes are doped into the system. It has also been found that the correlation strength in a given pnictide-family is directly correlated with the Fe-As bond length [330]. However, so far only little is known about the influence of the spacer layer on the low energy electronic states of the FeAs layer. The majority of iron-based superconductors (IBSC) contain insulating spacer layers. Thus, the question is raised what will be the response of the low-energy states in the FeAs layer if the spacer layer becomes metallic?
The class of IBSCs consists of a large amount of different families [113]. All those compounds have in common the iron-pnictide (FePn) respectively iron-chalcogenide (FeCh) layers which are separated by different kinds of spacer layers. This spacer layer can be relatively thick and composed of many elements (e.g. in $(Sr_2Sc_2O_5)Fe_2As_2$, $(Sr_2VO_3)FeAs$), and be regarded as an additional material with its own physical properties stacked alternatively with the FePn layer. In such a case, electronic coupling between the FePn (FeCh) and the spacer layers would manifest itself in a mutual alteration of the low energetic electronic structure in the system
For example it has been shown that in the case of $(Sr_2VO_3)FeAs$, the Mott-insulating $Sr_3V_2O_6$ spacer layer pushes the system further towards a Mott transition. It has been found that within ~ 0.1 eV below the Fermi level the spectral weight of the Fe-derived itinerant states is strongly suppressed [see Fig. 5.1 a) and [333]].
On the other hand, inhomogeneous dynamical mean-field theory calculations predict, that a Mott-insulating layer sandwiched between two metallic layers develops metallic behavior

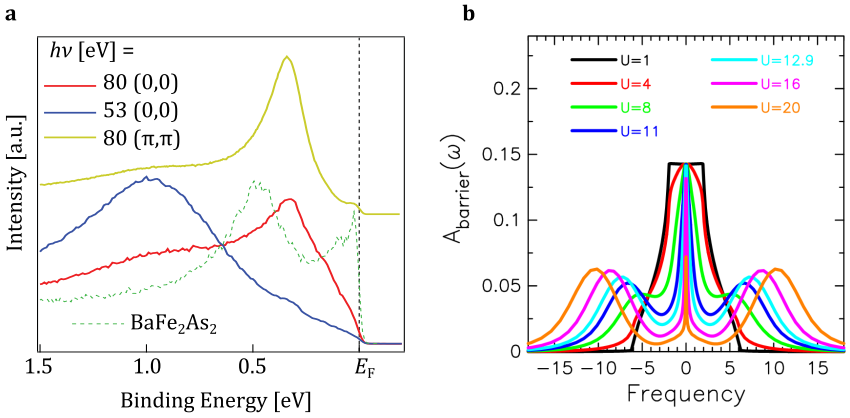

Figure 5.1: Interlayer coupling in superlattice systems. **(a)** Direct comparison of the $(Sr_2VO_3)FeAs$ valence band (VB) measured at $h\nu = 53$ and 80 eV, with the VB of $BaFe_2As_2$. Adapted from [333]. A strong suppression of the peak close to E_F is observed for $(Sr_2VO_3)FeAs$ compared to $BaFe_2As_2$. **(b)** Local spectral function at the Mott insulating barrier plane for a single-barrier-plane sandwiched between metallic layers for low temperature and different U values (increasing from top to bottom near zero frequency). Adapted from [334].

at low temperatures and induces a Fermi liquid like coherence peak at the Fermi level [see Fig. 5.1 b) and [334]].

Since in iron-based superconductors Hund's coupling and on-site Coulomb interactions are believed to be responsible for electronic correlation of the FeAs-derived states [see Ref. [121, 135, 146]] it is expected that correlations are weakened if the spacer layer is a good metal. However, such a study is still lacking in literature since only very recently this kind of compounds, the 112 family ($AEFeAs_2$, AE = Alkaline Earth), became available, although it had already been predicted by density functional theory (DFT) calculations in the early stage of the IBSCs era [335–337]. Preliminary ARPES studies of $Ca_{1-x}La_xFeAs_2$ confirmed the metallicity of the CaAs-spacer layer [338, 339] but reports on the detailed electronic band structure of the CaAs layer and its influence on the overall electronic structure in the 112 compounds are still missing.

In this work, combining DFT calculations and ARPES experiments, we revealed the full electronic band dispersion in the vicinity of the Fermi level of $Ca_{1-x}La_xFeAs_2$, ($x = 0.1$). We could unambiguously assign the different observed bands to the FeAs or CaAs layer as well as elucidate the electronic correlation in the individual layers. The band width of the Fe $d_{xz/yz}$ and d_{xy} orbitals has been compared between $Ca_{0.9}La_{0.1}FeAs_2$ and $Ca_{0.9}La_{0.2}Fe_2As_2$ which has an insulating spacer layer and the same amount of electron doping per Fe, $p = 0.1$. Since both compounds have a similar Fe-As bond length a similar mass enhancement would be expected for the Fe derived states [330, 340, 341].

We found that the electronic correlation of the Fe $3d$ derived bands are not weakened by the metallicity of the spacer layer. On the other hand, we observed a slight increase of the quasiparticle mass in the spacer layer for orbitals which contain out-of plane lobes (e.g. Ca $3d_{z^2}$ and As $4p_z$) but no enhanced correlation for orbitals with only in-plane lobes (e.g. As $4p_x/p_y$).

Additionally, we confirm the predicted non-trivial topological nature of the CaAs spacer layer which, in combination with the superconducting FeAs layer, makes $Ca_{0.9}La_{0.1}FeAs_2$ to a staggered combination of a quantum spin hall (QSH) insulator and a high temperature superconductor hosting topological superconductivity on the edge of the CaAs layer [342].

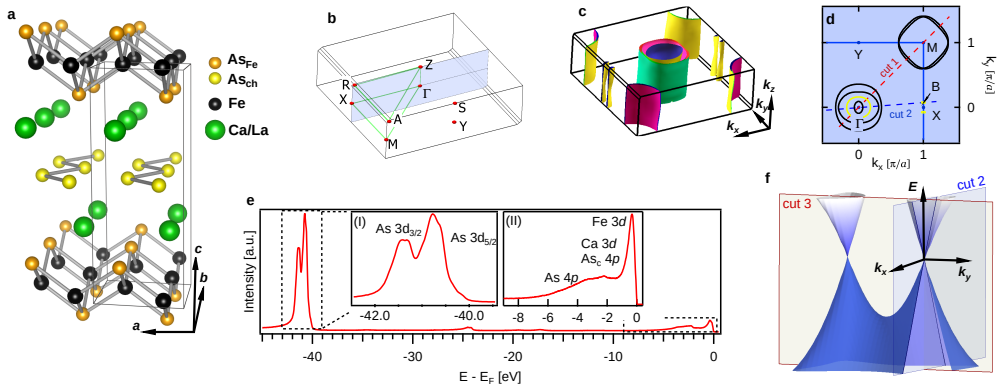

Figure 5.2: **(a)** Crystal structure of $Ca_{1-x}La_xFeAs_2$. **(b)** Brillouin zone of $Ca_{1-x}La_xFeAs_2$ in the monoclinic ($P2_1$) crystal symmetry. **(c)** and **(d)** Fermi surface obtained by DFT calculation consisting of 4 hole-like sheets around Γ, 2 electron-like pockets around the BZ-corner (M point) and two electron-like cones in the vicinity of X. The point $B \approx (1, 0.075)\frac{\pi}{a}$ is defined as the center of the electron pocket. **(e)** Core level spectrum of $Ca_{0.9}La_{0.1}FeAs_2$ taken with $h\nu = 110$ eV photons. Inset shows zoom-in of As $3d$ states and the valence band. **(f)** DFT-calculated, Dirac-cone like band structure in the vicinity of X.

5.1.1 Crystal structure and DFT-calculations

Unlike other iron-arsenide superconductors, $Ca_{1-x}La_xFeAs_2$ crystalizes in the monoclinic space group $P2_1$ (No. 4) with the identity and the two-fold screw axis along the y-axis building the only two symmetry operations [336, 337]. The low crystal symmetry is induced by the novel type of metallic spacer layer containing chain-like arranged Arsenic atoms [see Fig 5.2 a)]. Core level spectroscopy revealed a splitting of the As $3d$ states, likely due to the different chemical environments of the As atoms in the chains (As_{ch}) and in the FeAs layers (As_{Fe}) [see Fig. 5.2 e)]. The total band width of the valence band is $\sim 6-8$ eV, similar as in $BaFe_2As_2$ [see Fig. 5.2 e), inset (II) and [344]]. The characteristic angle $\beta \sim 91.5$ for the $P2_1$ monoclinic crystal structure deviates only slightly from the ideal 90 degrees which would give the usual tetragonal symmetry. As shown in 5.2 b), the Brillouin zone of $Ca_{1-x}La_xFeAs_2$ closely resembles that of tetragonal, face-centered structures such as the 111 and 1111 families. The Fermi surface from DFT calculations is drawn in 5.2 c) and in 5.2 d). Besides the Fe $3d$ derived FS-sheets which consist of three hole-like sheets around the BZ-center and two electron-like sheets around the BZ-corner, there is an additional hole-like

Table 5.1: Symmetry derived selection rules of the p and d orbitals. For a given direction, the allowed orbitals are given for each polarization (columns). The column named "undefined" lists the orbitals which are neither even nor odd along the specified cut. It has been found that in this case, these orbitals contribute with a finite intensity in either polarization [343]. Note that here the orbitals are given in the two-Fe unit cell notation.

	polarization		
direction	s	p	undefined
1: $\Gamma - M$	$d_{x^2-y^2}$	d_{z^2}, d_{xy}, p_z	d_{xz}, d_{yz}, p_x, p_y
2: $\Gamma - B$	d_{xy}, d_{yz}, p_y	d_{xz}, $d_{x^2-y^2}$, d_{z^2}, p_x, p_z	

sheet in the center and small electron-like FS-sheets at two sides of the BZ-boundary [see Fig. 5.4 a, b) [345, 346]]. The hole-like band, labeled as ζ, is of a mixed character, derived from As p_z, Ca d_{z^2} and Ca $d_{x^2-y^2}$ orbitals. The band at the zone boundary (χ) is of mainly As p_x-like character with in-plane lobes and forms a Dirac-cone like structure [see Fig. 5.3]. Note that the notation is refereed to the 2-Fe unit cell convention in this work. The whole FS and the Dirac-cone like structure around X are predicted to be very two dimensional in nature with minor variation along k_z which is in contrast to previous DFT results [345, 346].
We would like to mention that, so far, the Dirac-cone like structure and its two dimensionality has not been confirmed by experiments [338, 339].

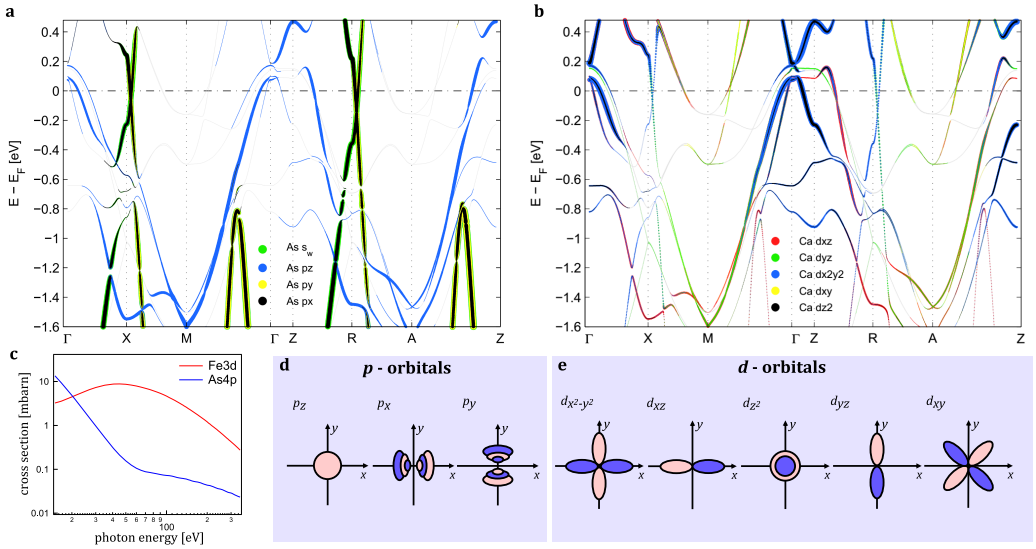

Figure 5.3: DFT-calculated band structure of the stoichiometric compound $CaFeAs_2$ along the path as defined in Figure 5.2 b). **(a)** Character of the band structure resolved for the As_{ch} $4p$ and **(b)** for the Ca $3d$ orbitals. Amount of visible color denotes the weight of the individual orbital. **(c)** Calculated energy dependence of the photo ionization cross section for Fe $3d$ and As $4p$ states [190]. **(d)** and **(e)** Schematics of spacial symmetry of p and d orbital cubic harmonics.

5.2 ARPES results

It has been shown that depending on the orbital characters the photoemission cross section varies significantly with the photon energy ($h\nu$) and the photon polarization (σ) [see section 2.2.5]. Fig 5.3 shows the calculated cross section (CS) vs. $h\nu$ for Fe $3d$ and As $4p$ orbitals. Around $h\nu = 20$ eV, the CSs are equal for As $4p$ and Fe $3d$ but have the largest difference at ~ 60 eV. It is expected that the ARPES intensity is mainly contributed by the Fe $3d$ orbitals at $h\nu = 60$ eV.

5.2.1 Fe-derived band structure

Figure 5.4 c) shows the ARPES Fermi surface (FS) recorded with $h\nu = 62$ eV which corresponds to $k_z \approx 14\frac{\pi}{c}$, in the free electron final-state approximation with an inner potential of $V_0 = 10.5$ eV. The ARPES intensity map at E_F in the $(k_x, k_y = k_x, k_z)$-plane is shown in Figure 5.4 d). No significant variation of the FS along the k_z direction is observed. The ARPES spectra obtained with s and p polarized light along *cut 1* and *cut 2* are shown in Figure 5.4 e1) - h1). Although the As $4p$-derived bands are still visible (see fast dispersing band

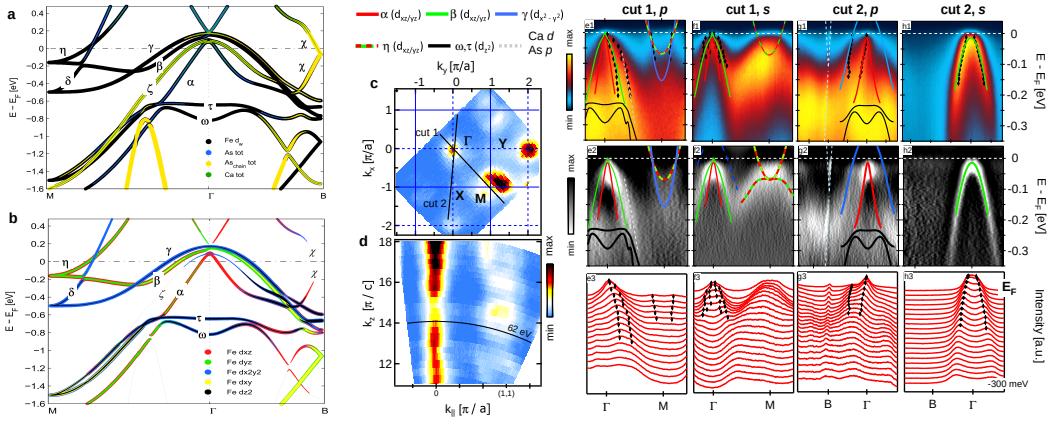

Figure 5.4: Orbital character of the Fe 3*d* derived band structure. DFT calculations for the stoichiometric compound $CaFeAs_2$ along the path as indicated in 5.2 d), resolved for **(a)**, the individual atoms and **(b)**, the Fe 3*d* orbitals. Amount of visible color denotes the weight of the individual orbital. **(c)** ARPES color-coded intensity map of the in-plane Fermi surface, measured by using circularly polarized light with $h\nu = 62$ eV corresponding to $k_z \sim 14\ \frac{\pi}{c}$. **(d)** Out of plane intensity distribution for the cut along the diagonal of the BZ (*cut 1*). **(e1) - (h1)** ARPES spectrum of cuts along $\Gamma - M$ resp. $\Gamma - B$ for *p* and *s* polarized light, respectively. Overlaid DFT bands are renormalized by a factor of approx. 2-3. **(e2) - (h2)** Corresponding curvature plots, obtained by the method as described in [347]. **(e3) - (h3)** Momentum distribution curves of spectra presented in **(e1) - (h1)** for energy range between $E - E_F = -300$ meV and E_F.

around *B*), due to the enhanced cross section of the Fe 3*d* states at $h\nu = 62$ eV, the high intensity is expected to be from the Fe 3*d* states. By changing the polarization, the spectrum is significantly modified. Table 5.1 lists the allowed orbitals for a given sample orientation and photon polarization, as explained in section 2.2.5 and [338, 343]. Strictly speaking, these symmetry rules have been derived for iron-pnictides with tetragonal or orthorhombic structure. However, we found very similar photon-polarization dependent behavior in $Ca_{1-x}La_xFeAs_2$ as for the case of e.g. $Ba(Fe_{1-x}Co_x)_2As_2$ and therefore conclude that these rules still can be applied [119, 343]. By conducting a systematic analysis of the ARPES data obtained in both directions (*cut 1* and *cut 2*) and both, *s* and *p* polarizations, we could resolve the complex, "tangled" band structure around Γ and assign the different bands to those predicted by the DFT calculation. For the Fe 3*d* derived bands a mass enhancement by a factor of 2-3 has been found which is a common value among iron-pnictides. Note that the mass of the $d_{x^2-y^2}$ band at thee *M* point is not found to be strongly enhanced as suggested by Y. Li *et. al.* [338]. As discussed by V. Brouet *et al.* [119] the symmetry arguments

Table 5.2: Band specific mass enhancement and shift needed to fit the DFT-calculated bands to the experimental dispersion (obtained by MDC fitting). Values in brackets are obtained by adjusting the DFT band dispersion by eye to the spectrum and 2D-curvature plots, since the experimental dispersion couldn't be extracted by fitting of the MDCs or EDCs.

	Fe - bands					**CaAs - bands**	
band	α ($d_{xz/yz}$)	β ($d_{xz/yz}$))	γ ($d_{x^2-y^2}$)	η ($d_{xz/yz}$)	δ ($d_{x^2-y^2}$)	ζ (p_z)	χ (p_x)
m^*/m	3 ± 0.2	1.5 ± 0.1	2.2 ± 0.2	(2)	(2.2)	1.5 ± 0.1	1
shift [meV]	-40 ± 10	-100 ± 10	0 ± 10	(10)	(70)	-80 at Γ	-

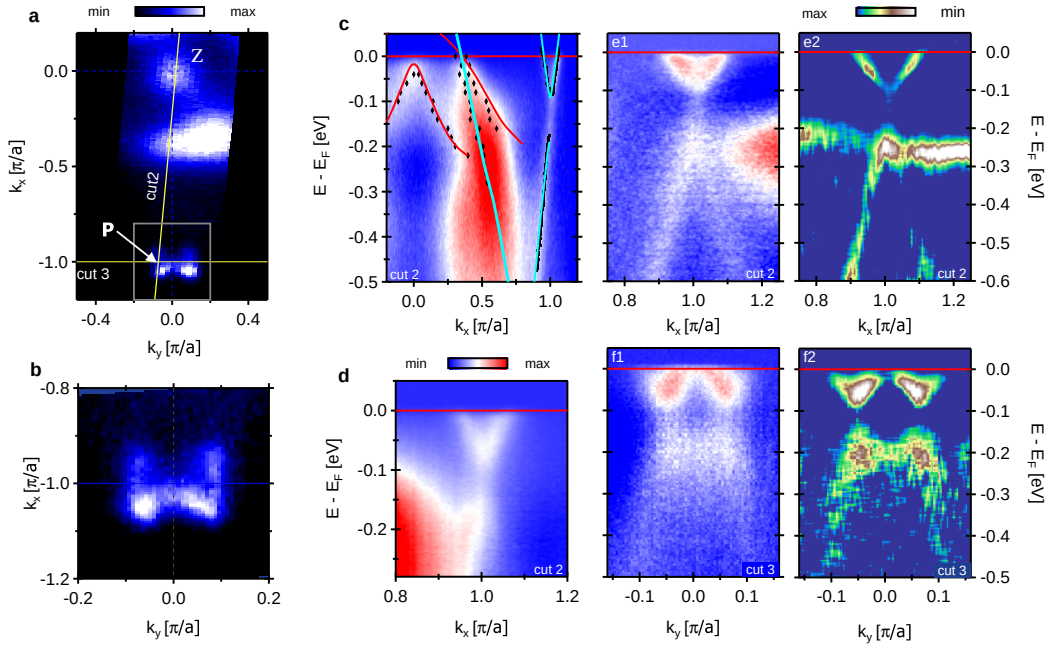

Figure 5.5: **(a)** ARPES intensity map of the Fermi surface in $k_x - k_y$ plane, measured by using circularly polarized light with an energy of $h\nu = 23$ eV which, in the free electron final state approximation corresponds to an out-of plane momentum of $k_z \approx 9\ \pi/c$. **(b)** Enlarged view of the Fermi surface in the region of the BZ-boundary. **(c)** Measured ARPES spectrum along *cut 2* obtained with $h\nu = 23$ eV. Black diamonds indicate position of peaks as derived by fitting multi peak Lorentzian curves to the momentum distribution curves (MDCs). Overlaid red lines represent DFT calculations of the Fe-derived bands and cyan colored lines calculation of the CaAs-layer derived bands. The As p_z derived hole-like band has been renormalized by a factor of 1.5 while the As p_x derived bands at the BZ boundary are not renormalized. **(d)** Zoom-in at the BZ-boundary of the same cut at a lower photon energy of $h\nu = 20$ eV, corresponding to $k_z = 8\ \pi/c$ (B-point). **(e1)** Same direction of the cut as d) but at $h\nu = 25$ eV, corresponding to $k_z = 9\ \pi/c$ (P-point). **(e2)** Curvature plot of e1) obtained with a method as described in Ref. [347]. **(f1), (f2)** ARPES intensity plot and corresponding curvature plot along *cut 3* at $h\nu = 20$ eV. The background has been subtracted for panel c), d), e1) and f1) as described in the methods section.

listed in table 5.1 cannot be applied straight forward for the bands at M since the parity is inverted for those bands. Therefore the lower band observed with p polarization is assigned to $d_{x^2-y^2}$ and the shallower band observed with s-polarization to $d_{xz/yz}$. The energy shift and the renormalization factor of all the bands compared to the bare DFT bands are given in Table 5.2. As already reported for LiFeAs and $Ba(Fe_{1-x}Co_x)_2As_2$ the values vary for the different bands but are in the usual range of $m^*/m = 1.8-3$ with a shift of ± 100 meV [348].

5.2.2 CaAs-derived band structure

To investigate the electronic structure of the CaAs-layer, the photon energy has been tuned to the range around $h\nu = 20$ eV. The in-plane Fermi surface intensity map taken at $h\nu = 23$ eV is plotted in Figure 5.5 a), b) which shows the Fermi surface sheets around X and an additional large sheet around Γ, which was not observed at higher photon energies. The ARPES spectrum along *cut 2* [Fig. 5.5 c)] shows this additional band, (ζ band), which is hole-like, strongly dispersive and has a large Fermi momentum $k_F \sim 0.35\ \pi/a$. The ζ band is formed by strongly hybridized As p_z, Ca d_{z^2} and Ca $d_{x^2-y^2}$ orbitals [see Fig. 5.3 a) and b)]. Additionally, in this spectrum the linear, As p_x-derived χ band is observed

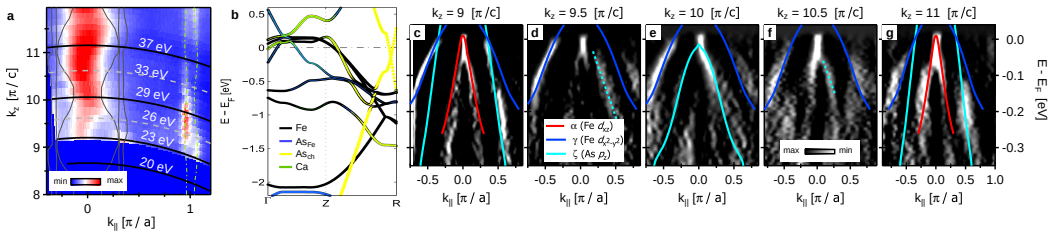

Figure 5.6: **(a)** ARPES intensity map of the out-of-plane Fermi surface along *cut 2*, as indicated in Figure 5.5 a). **(b)** DFT calculation of the k_z-dependence of band structure in the BZ-center. Amount of visible color represents weight of the atomic contribution to the band. **(c) - (g)** Curvature plots of the band dispersion in the center of the $k_x - k_y$ plane for different values of k_z. Overlaid solid lines represent the renormalized and shifted DFT calculations [see table 5.2] of the different Fe and As derived bands, as indicated.

around $k_x = \pi/a$. Note that the measured bands have the same slope as those from DFT calculations, indicating negligible electronic correlation of these states. As shown in Figure 5.6 a), the cut at $h\nu = 23$ eV is curved in 3D-momentum space. Thus, the region around $(k_x, k_y) = (1, 0)\frac{\pi}{a}$ is located at a k_z position below the zone boundary. The measured band structure along *cut 2*, passing through $B = (1, 0.075, 0)\frac{\pi}{a}$ resp. $P = (1, 0.075, 1)\frac{\pi}{a}$ is shown in Figure 5.5 d) and e1), e2) respectively. A cut along the BZ-boundary (*cut 3*) through B is shown in panel f1), f2). In panels d) - f2) the individual branches can be identified unambiguously. It is unveiled that the DFT-predicted Dirac cone is gapped with a gap of around 0.1 eV between the lower and upper "V"-shaped bands.

Dispersion of the χ and ζ band along k_z

As shown in Figure 5.6 a), the χ bands are two-dimensional and their FS doesn't vary along k_z, which is in good agreement with the DFT calculations. The only band which is predicted to be dispersing along k_z is the ζ band, derived by the As p_z and Ca d_{z^2} orbitals with out-of-plane lobes. The k_z dependence along *cut 3* is shown in Figure 5.6 a). Between $k_z = 9\ \pi/a$ and $k_z = 10\ \pi/a$ a band dispersing from $k_F = 0.35\ \pi/a$ towards the center is observed. However, for larger k_z the intensity of this band becomes weaker and a clear dispersion can only be followed by a careful analysis of the individual bands, as presented in Figures 5.6 c) - g) for different values of k_z. In contrast to the Fe $3d$ bands, which are barely changing for the different values of k_z, the ζ band is found to cross E_F at the BZ-boundary (odd k_z values) and to sink below the Fermi level at the BZ-center (even k_z values). This analysis reveals that the ζ band is forming a closed Fermi surface around Z.

5.2.3 Electronic coupling of the FeAs and the CaAs layers

So far we have found that the effective mass of the CaAs-derived states is enhanced for the As p_z band but not for the As p_x band. Considering the Fe $3d$ states, an exclusive comparison to DFT calculations wouldn't deliver much insights to the change of electronic correlation due to electronic coupling to the spacer layer, since among the iron-pnictides resp. iron-chalcogenides strong variation of the band width renormalization factor is found. [318, 348, 349]. In order to quantify the electronic coupling of the metallic spacer layer to the FeAs layer we directly compare the band width of the β and γ-band to the related 122 compound $Ca_{1-x}La_xFe_2As_2$ (Ca122) ($x = 0.2$). Figure 5.7 compares the band width of the β band which is derived by Fe $d_{xz/yz}$ orbitals along *cut 1*. As shown in Figure 5.7 g) the bands from both compounds (Ca112 and Ca122) fall almost exactly on each other. Thus, a very similar amount of electronic correlation is found for this orbital. This is confirmed by a comparison of the β-band dispersion along a cut from Γ to X [see Fig. 5.7 h)]. Although no

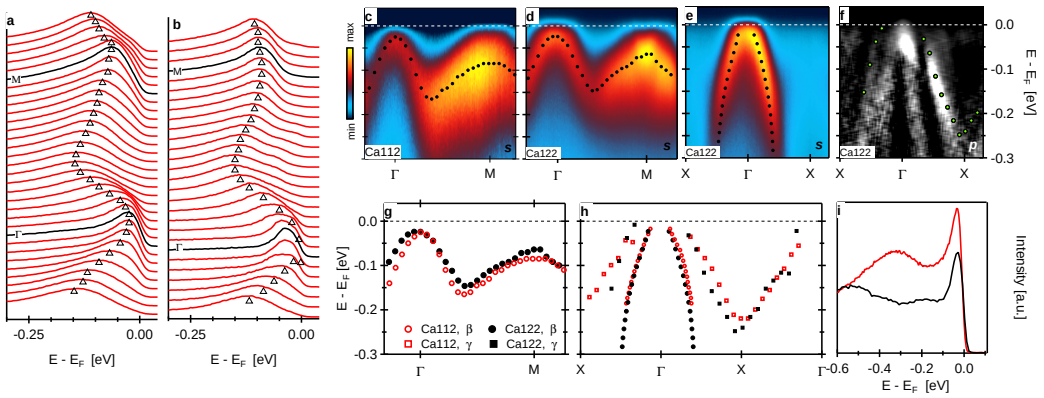

Figure 5.7: (a), (b) EDCs of the ARPES spectrum obtained with s polarized light along *cut 1* (as indicated in Figure 5.4 c) for $Ca_{1-x}La_xFeAs_2$ (Ca112) resp. $Ca_{0.9}La_{0.2}Fe_2As_2$ (Ca122). Black markers indicate the position of the peak to indicate the dispersion. **(c), (d)** Same as a,b) illustrated as ARPES intensity map. Again, black markers indicated the band dipersion obtained from the EDC peak positions. **(e)** APRES intensity map of Ca122 obtained with s polarized light along $\Gamma - X$ direction. The black markers indicate band dispersion as obtained from MDC fitting. **(f)** Curvature plot of ARPES spectrum along $\Gamma - X$ direction, obtained with p polarized light. The band dispersion is traced by cyan colored plots; obtained by peak position of the Curvature plot. **(g), (h)** Comparison of the band dispersion for the β and γ band along $\Gamma - M$ resp. $\Gamma - X$. **(i)** EDC at Γ of Ca112 and Ca122.

band bottom is found the dispersion is again very similar. Along this direction the dispersion of the $d_{x^2-y^2}$ derived γ band is also compared. Even though the agreement in the one-to-one comparison is less good, the band width of both bands is again identical. We conclude that electronic correlation in the FeAs layer is very similar in both compounds. Also, different to what is shown in Figure 5.1 b) the density of states near E_F at Γ is not significantly enhanced [see Fig. 5.7 i)].

5.3 Discussion

It has been demonstrated that in a iron-pnictide family, electronic correlation is mainly determined by carrier doping and by structure factors such as the Fe-As bond length [330]. For comparison we chose the well studied 122 pnictide, $Ca_{0.9}La_{0.2}Fe_2As_2$ (Ca122), as a reference compound, which has a similar Fe-As bond length (2.38 ± 0.01 Å) to the Ca112 and the same electron-doping per Fe ($p = 0.1$) [340, 341]. The crystal structure of Ca112 is also very similar to the one of Ca122 except the addition of the metallic As-chains in the Ca spacer layer [see Fig. 5.2 a)]. In order to quantify the influence of a metallic layer on the electronic correlation in the FeAs layer, the band width of both compounds has been compared. It turned out that the β and γ bands are the best choices for a one-to-one comparison since the bands can be traced over their whole band width. We found, that the both bands overlay nearly perfectly on each other, indicating that the proximity of a metallic layer has only negligible effect on electronic correlation in the FeAs layer. The electronic correlation is similar in both compounds.

As for the CaAs spacer layer we observed notable mass enhancement of the ζ band, derived from orbitals with lobes along the z direction. On the other hand, we found that the χ bands derived by in-plane As p_x orbitals are strongly dispersing and don't show enhanced effective mass. Hence we conclude that the overlap of As p_z orbitals with orbitals of the FeAs layer induces electronic correlation into the ζ band of the CaAs layer. This confirms that indeed the layers are at least weakly electronically coupled but electronic correlation

in the FeAs layer are not influenced by the presence of a metallic spacer layer. This is in concert with the very similar maximum $T_{c,max} = 49$ K which is found for optimally doped $Ca_{1-x}La_xFeAs_2$ and $Ca_{1-x}La_xFe_2As_2$.

The observation of no mass-enhancement in the χ bands around X suggests, that these states are electronically decoupled from the FeAs layer. In addition, we observed that the Dirac cone like structure is gapped with a gap of the size of ~ 0.1 eV which is consistent with the theoretical consideration by X. Wu *et al.* - i.e. strong spin orbit coupling (SOC) of the As in the As-chain opens the gap at the Dirac cone with a non-trivial band structure [342]. Our results would suggest that below T_c, $Ca_{1-x}La_xFeAs_2$ is an alternating stack of layers which are either a superconductor or a topological non trivial quantum spin hall (QSH) insulator.

5.4 Conclusion

In summary, we have presented a combined DFT and ARPES study of the band structure of $Ca_{0.9}La_{0.1}FeAs_2$ with the focus on electronic correlation in the FeAs, the CaAs spacer layer and their mutual influence. In an exhaustive deployment of the full variability of the photon energy and polarization we have extracted all individual bands of the rich electronic structure consisting of eight bands in the vicinity of the Fermi level. For the bands derived by the Fe $3d$ orbitals we have found the usual magnitudes for the mass enhancement which slightly varies between the different bands. The comparison to $Ca_{0.9}La_{0.2}Fe_2As_2$, which structurally differs from $Ca_{0.9}La_{0.1}FeAs_2$ only by the additional metallic As chains, revealed a very similar band structure for both compounds. This indicates that the metallicity of the spacer layer has unexpectedly small influence on the electronic correlation in $Ca_{0.9}La_{0.1}FeAs_2$.
Additionally, our measurements revealed a clear picture of the band structure of the metallic spacer layer, for the first time. It consists of an additional, three dimensional hole-like FS around Z and two dimensional Dirac-cone like bands at the BZ boundary. The hole-like band is predicted to be derived by hybridized As p_z and Ca d_{z^2} orbitals with out-of plane lobes. The three dimensionality and notable mass enhancement suggests a significant coupling of these states along the z-direction with electronic correlation induced by the FeAs layer.
We found that the Dirac cone like bands at X are gapped with a gap size of ~ 0.1 eV which is predicted to be induced by strong spin-orbit coupling of As in the As-chains. This could indicate that below T_c, $Ca_{1-x}La_xFeAs_2$ is a alternating combination of a quantum spin Hall insulator and a high-temperature superconductor with natural topological superconductivity on the edge states of the CaAs layer [342].

5.5 Appendix: Methods

5.5.1 Single crystal growth - Acknowledgements

High quality single crystals of $Ca_{0.9}La_{0.1}FeAs_2$ have been grown by G.F. Chen, Institute of Physics and Beijing National Laboratory for Condensed Matter Physics, Chinese Academy of Sciences, Beijing 100190, China. The crystals have been grown by the self flux technique, similar to as described in [336]. We would like to thank the sample growers for supplying high quality single crystals.

5.5.2 Free electron final state model

In the free electron final state description of the photoemission process, (FEFS) the location of the out-of plane momentum (0, 0, kz) is given by $k_z = \sqrt{\frac{2m}{\hbar^2}}\sqrt{h\nu + V_0 - \phi_A}$ where ϕ_A is the work function of the electron analyzer and V_0 is the inner potential. For Fe-As

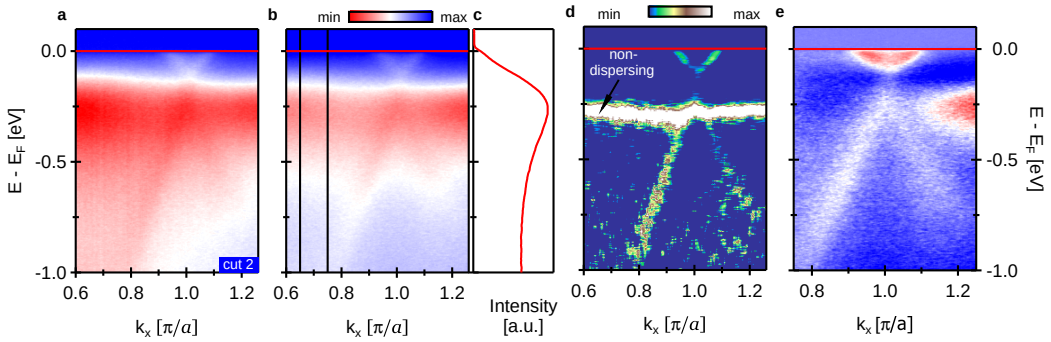

Figure 5.8: **(a)** Raw ARPES intensity map obtained with circularly polarized light of $h\nu = 25eV$. **(b)** Same as a) but normalized such that each EDC has the same integrated intensity. **(c)** Averaged EDC of the region marked by black lines in panel b). **(d)** Curvature plot of spectrum presented in a). The non dispersing part of the band structure is indicated. **(e)** Background subtracted ARPES spectrum where the averaged EDC of panel c) has been subtracted consecutively from the whole spectrum of panel b).

compounds a value of $V_0 = 10 - 15$ eV is usually found. In an ARPES experiment, V_0 is usually determined by the periodicity of the dispersion band structure (as e.g. illustrated in Figure 5.6).

5.5.3 Background subtraction

Background subtraction of the data has been performed for the ARPES spectra of the Dirac cone shaped bands at the BZ-boundary as presented in Fig. 5.5. It has been observed that in the vicinity of the Dirac cone like band structure, a non-dispersion, feature is present at a binding energy of $E - E_F = -0.25$ eV [indicated by arrow in Figure 5.8 d)]. In order to obtain a clear picture of the dispersing band, the spectra has first been normalized such that the featureless dispersion has similar intensity for all momenta and then an EDC which has been obtained at a featureless part of the spectrum is subtracted.

Chapter 6

Electronic structure of $Pr_4Fe_2As_2Te_{0.88}O_4$

6.1 Introduction

Since the discovery of high temperature superconductivity in iron based superconductors (IBSC), the mechanism mediating electron pairing remains an unsolved problem [109, 111]. Important aspects in the search for a theoretical description are the electronic bandstructure, Fermi surface (FS) topology and the symmetry of the superconducting gap. Among the different systems of IBSCs, the Fermi surface topology changes significantly [123, 330]. In many cases e.g. in the iron-pnictide 122 and 111 families the FS consists of hole-like pockets in the Brillouin zone (BZ) center and electron-like pockets in the BZ-corner. This topology has motivated the consideration that the pairing is based on a scattering process between electron and hole pockets. In this theory, the order parameter is an extended s-wave gap ($s\pm$) which' phase changes sign between the BZ-center and the BZ-corner [139, 145, 350–352]. However this FS-nesting scenario faces challenges if the FS-topology changes and consists only of hole-like or electron-like FS-sheets [296, 353, 354]. For example in the iron chalcogenide (FeCH) systems $A_xFe_{2-y}Se_2$, (A = K,Cs,Rb,Tl), $(Li_{1-x}Fe_x)$OHFeSe (Li11111) and monolayer FeSe on $SrTiO_3$ (FeSe/STO) the FS consists only of electron-like pockets in the BZ-corner. For those systems the FS-nesting pairing picture has to be revised [353–359]. Since the highest T_c in IBSCs is hosted by FeSe/STO ($T_c \sim 100K$), the question naturally arises if such an FS-topology is a prerequisite in order to achieve such a high critical temperature. So far a FS formed solely by electron-like sheets has only been found in FeCH.

Until now the highest observed T_c in iron-pnictides (FePN) is hosted by the 1111 family [360]. Since cleaving produces a polar surface on 1111 pnictide crystals, angle-resolved photoemission spectroscopy studies (ARPES) have given ambiguous results for the electronic structure and FS with strong contributions of surface states [325, 361–364]. It is a great challenge to differentiate between bulk and surface contributions, and so far no clear picture of the bulk FS has been obtained experimentally [see Fig 6.1 a), b)]. It would be of high interest to reveal the bulk FS of 1111 compounds to uncover the connection of the FS-topology and the T_c.

With the discovery of the new '42214' iron-pnictide family and its representative compound $Pr_4Fe_2As_2Te_{1-x}O_4$, a compound has been synthesized with a crystal structure which resembles the one of the '1111' family but which has a cleaving plane which is very similar to the one in the '122' family [see Fig. 6.1 e)] [365, 366]. Among all IBSCs, the 122 family has been heavily studied by ARPES and it is widely believed that the observed electronic structure is bulk-representative. Importantly, the cleaved surface doesn't show a polar discontinuity on the termination layer which would lead to a charge transfer from the bottom

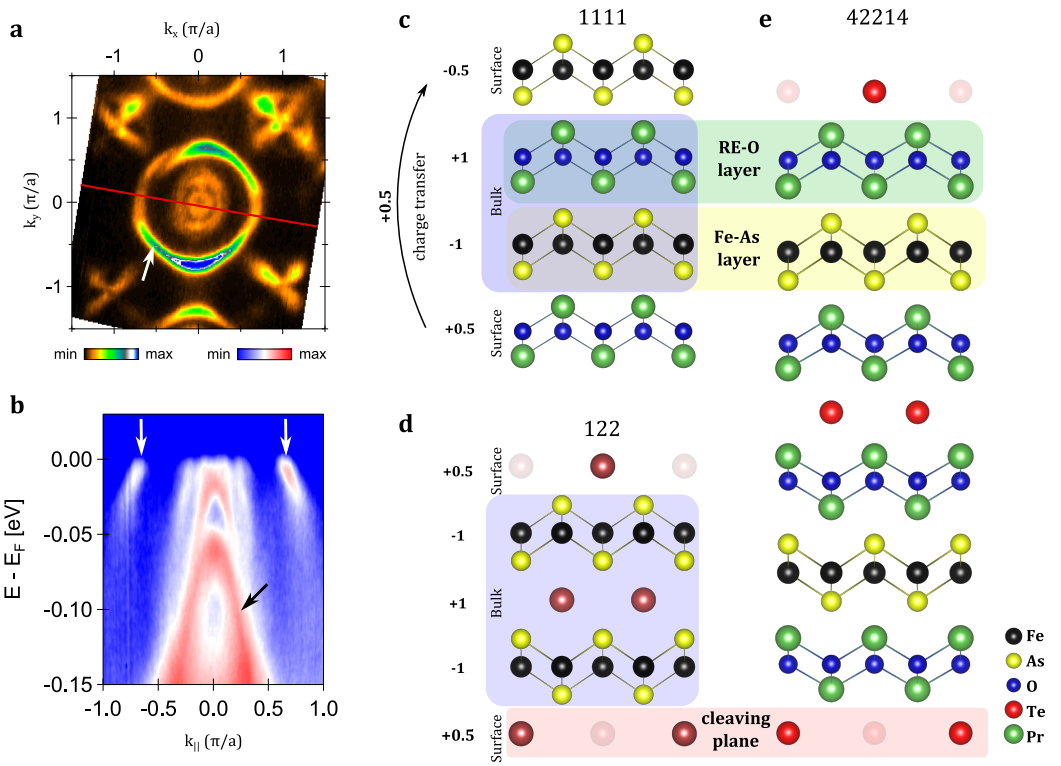

Figure 6.1: **(a)** ARPES intensity map of the Fermi surface in the $k_x - k_y$ plane of LaFeAsO, obtained with $h\nu = 60$ eV, p-polarized light. **(b)** ARPES spectrum of the cut along red line in panel a). Arrows in a) and b) indicate surface states which, so far, have been observed in ARPES measurements of all 1111 compounds. **(c)** Crystal structure of the 1111 family consisting of the common Fe-As layer and a RE-O (RE-rare earth) layer. Arrow indicates the charge transfer from the bottom to the top of the cleaved crystal. **(d)** Crystal structure of 122 family consisting of the common Fe-As layer and an alkaline-earth layer. **(e)** Crystal structure of $Pr_4Fe_2As_2Te_1O_4$. The Fe-As layers are surrounded by RE-O layers, resembling the situation as in 1111 family. The Te layer is the termination layer when the sample is cleaved.

to the top of the surface layer as found, for example, in the '1111' system [see Fig. 6.1 c), d) and Ref. [367, 368]].

In the following we present a systematic high-resolution ARPES study of the electronic structure of $Pr_4Fe_2As_2Te_{1-x}O_4$ ($x = 0.12$) with a T_c of ~ 25 K and an effective electron doping of $p = 0.12$ per Fe. We found that the cleaved sample surface is terminated by the Te layer and no signature of the characteristic surface states as observed in the '1111' compounds could be found. Thus, we conclude that the cleaving surface is non-polar which is a necessary condition for a successful ARPES experiment. Our ARPES measurements on $Pr_4Fe_2As_2Te_{0.88}O_4$ unveiled that the FS is formed by electron-like pockets at the BZ-corner, only. The hole-like bands sink below the Fermi level, resembling the topology of the heavily electron-doped iron chalcogenides.

6.2 Methods

6.2.1 Sample growth - Acknowledgement

Plate-like high quality single crystals of $Pr_4Fe_2As_2Te_{0.88}O_4$ of size 100 μm x 100 μm have been grown by high pressure synthesis as described in Ref. [365, 366]. The single crystals have been grown by Sergiy Katrych, Institute of Condensed Matter Physics, EPFL, CH-1015 Lausanne, Switzerland. X-Ray diffraction has been employed to check that all crystals which have been used in the ARPES experiment are in the correct phase. We would like to thank the sample growers for supplying high quality single crystals.

6.2.2 ARPES experiments

ARPES experiments were carried out at the Surface and Interface Spectroscopy beamline [194], Swiss Light Source, using a Scienta R4000 electron analyzer with total energy and angular resolutions of $\sim$ 20 meV and $\sim 0.15°$, respectively. Samples were cleaved in-situ under ultrahigh vacuum conditions ($< 5 \cdot 10^{-11}$ mbar). All ARPES measurements have been performed at 15 K. The DFT calculations were performed by employing the full-potential linear augmented plane wave method and the generalized gradient approximation as implemented in the WIEN2K package [159] with the crystal structure shown in Figure 6.1 e) and the lattice parameters ($a = b = 4.02$ Å, $c = 29.86$ Å) as determined by x-Ray diffraction on single crystals [365]. The DFT+U method was employed to treat the localized f electrons of Pr. Our choice of $U_f \sim 9$ eV gave realistic results and fully localized the f electrons.

6.3 Results

6.3.1 Nature of termination layer

As shown in Figure 6.2 a) - c) the Fe 3p and Te 4p corelevel states are located at binding energies $\omega = E - E_F \sim -55$ eV and $\omega \sim -103$ eV, respectively. To identify the surface termination layer of the cleaved crystal, the core level spectra of both states have been recorded at various angles, α, between the incident photon beam and the sample surface-normal [see Fig. 6.2 d]. At gracing incidence ($\alpha = 76°$), a large fraction of the photoemission signal originates from the topmost layer while, if the sample is adjusted towards normal incidence ($\alpha = 0$), the photoemission signal of the subsurface layers is gradually enhanced. For $\alpha = 0$ we observe the highest intensity for the Fe 3p states and, on the other hand, the Te 4p peak is enhanced at $\alpha = 76°$, indicating that the sample is terminated by the Te layer.

6.3.2 Electronic band structure

The band structure and Fermi surface calculated by using DFT for $Pr_4Fe_2As_2Te_{1-x}O_4$ ($x = 0$) is shown in Figure 6.3 a) - b). As for most cases of IBSCs, the low energetic electronic bands which cross E_F are predicted to be exclusively derived from Fe 3d orbitals. On the other hand, the DFT calculations additionally show that the Te derived band is located within 2 eV below E_F and is highly dispersive. The calculation predicts three hole-like Fermi surface sheets in the BZ-center and two electron-like sheets at the BZ-corner. Very similar to other iron-pnictide compounds all bands which are crossing E_F are derived from Fe d_{xy} and $d_{xz/yz}$ orbitals. Additionally, the electronic structure two dimensional with almost no dispersion along the k_z direction, even less than in the 111 and 1111 classes [114, 306].

The ARPES spectra in Figure 6.4 a1) - c2) show the measured band dispersion along diagonal directions in the BZ, as indicated in Figure 6.4 c). Similar spectra have also been acquired along directions parallel to the BZ-boundary [see Fig. 6.5]. The measurement has

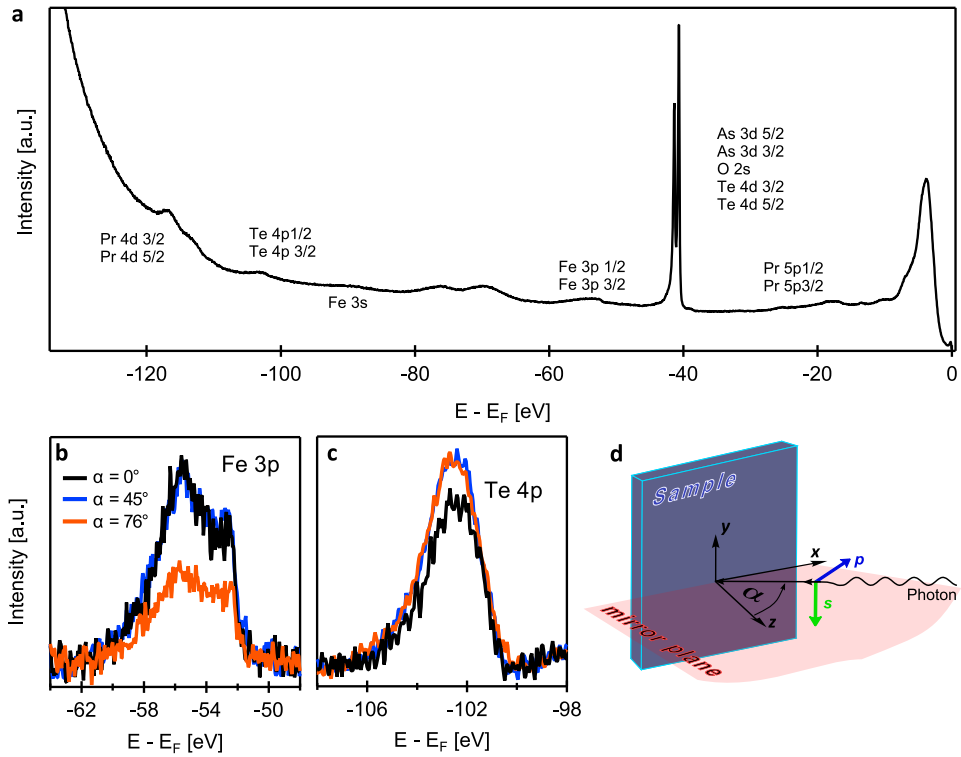

Figure 6.2: **(a)** Core level spectrum recorded with $h\nu = 157$ eV, circularly polarized photons. **(b), (c)** Enlarged view of the Fe $3p$ and Te $4p$ core states, respectively. The intensity has been normalized to the background, and the background (linear slope), has been subtracted. **(d)** Geometry of the ARPES-experiment. The arrows indicate the sample-intrinsic coordinate system with z indicating the surface normal. The angle between the surface normal and the incoming photon beam is indicated by α. The green and red arrows indicate the linear polarization of the light.

been performed by using linear polarized light with the polarization directions as indicated in Figure 6.2 d). The different bands are enhanced respectively suppressed for the different polarizations, depending on the symmetry of their orbital character (e.g see section 2.2.5 and Ref. [119]). This technique allowed us to identify each DFT predicted band in the ARPES measurement and draw a conclusive picture of the low energetic band structure along the high symmetry directions $\Gamma - M$ and $\Gamma - X$. We found that all the hole-like bands are below E_F, thus there exists no hole-like FS at the BZ-center. The obtained spectra show that the top of the d_{xy} band which is the closest to E_F is at a binding energy of -25 ± 5 meV [see Fig. 6.5 b1), b2)]. Thus, the FS consists solely of the electron-like pockets at the BZ-corner. The Luttinger count for the volume of the very two dimensional Fermi surfaces indicates 0.13 ± 0.01 e^- per Fe, in good agreement with the electron doping p. The excellent agreement between the electron doping and the FS volume is interpreted as another sign that the measured electronic bandstructure indeed reflects bulk electronic structure of $Pr_4Fe_2As_2Te_{0.88}O_4$ and is not contaminated by surface states. Note that the Luttinger-count of the ARPES-measured FS of the 1111 family gives a significant excess of holes which reflects its surface like nature [362]. In the comparison with the DFT calculations, we found an average mass enhancement for the Fe states of $m^*/m = 2.5 \pm 0.5$ which is in the usual range of FePn superconductors.

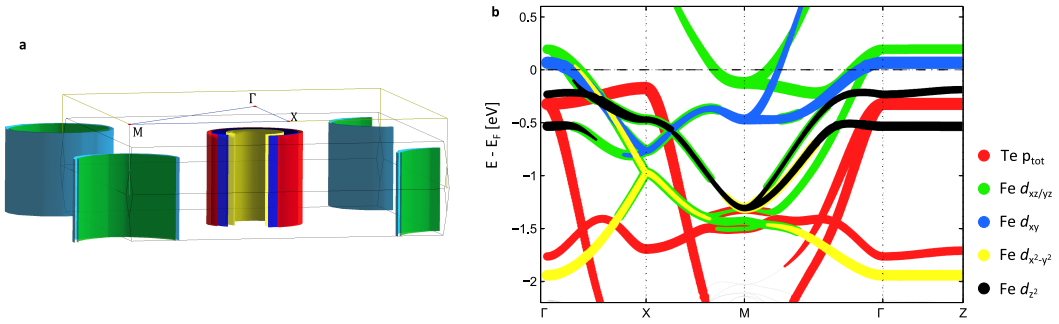

Figure 6.3: **(a)** DFT-calculated Fermi surface (FS) of the parent compound $Pr_4Fe_2As_2Te_1O_4$. All FS-sheets are highly two dimensional. Green lines denote the projected BZ. Blue lines denotes the path along high symmetry lines. **(b)** Calculated electronic band structure along high symmetry directions as indicated in Fig 6.4 c). The amount of visible color represents the weight of each atom respectively orbital.

6.3.3 Fermi surface

The ARPES intensity map of the Fermi surface in the $k_x - k_y$ plane is plotted in Figure 6.6 a). High intensity can be observed in the center of the BZ and at the BZ-corner. The strong intensity in the BZ-center is observed due to the high density of states (DOS) at the top of the hole-like bands which is broadened because of the finite temperature and instrumental resolution. At the M point, the electron-like FS sheets are observed. The difference to the measured Fermi surface of LaFeAsO as shown in Figure 6.1 a) is significant. Characteristic features - e.g. the large hole-like ring around Γ and the propeller-like features at M are not observed in the FS of $Pr_4Fe_2As_2Te_{0.88}O_4$.
The out-of-plane FS and the k_z dependence of the bands at $(k_x, k_y) = (0, 0)$ is shown in Figure 6.6 b). The observed quasi two-dimensional nature of the electronic structure is in good agreement with our DFT calculations [Fig. 6.2].

6.4 Discussion

In the field of IBSCs, the highest critical temperature for superconductivity ($T_c \sim 100$ K) has been reported for monolayer FeSe grown on a $SrTiO_3$ substrate. Its measured Fermi surface consists only of an electron-like sheet in the corner of the BZ, indicating strong negative charge transfer from the substrate to the FeSe film. Such a Fermi surface topology sets strong constraints on the theoretical description for the pairing mechanism in this system and is of high interest. For example, the scenario based on FS-nesting between the hole and electron-like sheets in the weak coupling theory is strongly challenged by such a FS topology. Up to now, three superconducting systems share such a FS-topology: FeSe/STO; $A_xFe_{2-y}Se_2$, Li11111. However, all of them have material-specific properties which don't allow to draw conclusions on the importance of the FS-topology for the high temperature superconductivity. For the FeSe/STO system strong coupling to the STO substrate have been claimed to play the key role for the enhanced superconducting transition temperature [369]. The $A_xFe_{2-y}Se_2$ superconductors are phase separated with the coexistence of an insulating and a superconducting phase which covers only a small volume fraction of the whole sample [370]. For the Li11111 system it has been found (due to a polar discontinuity) that the sample surface is different from the bulk and therefore ARPES results are ambiguous [359].
The newly discovered 42214 family is free from all those complications and additionally resembles the crystal structure of the 1111 family which hosts the highest T_c in bulk IBSCs. The observation of a purely electron-like FS in $Pr_4Fe_2As_2Te_{0.88}O_4$ with the sizeable T_c of 25

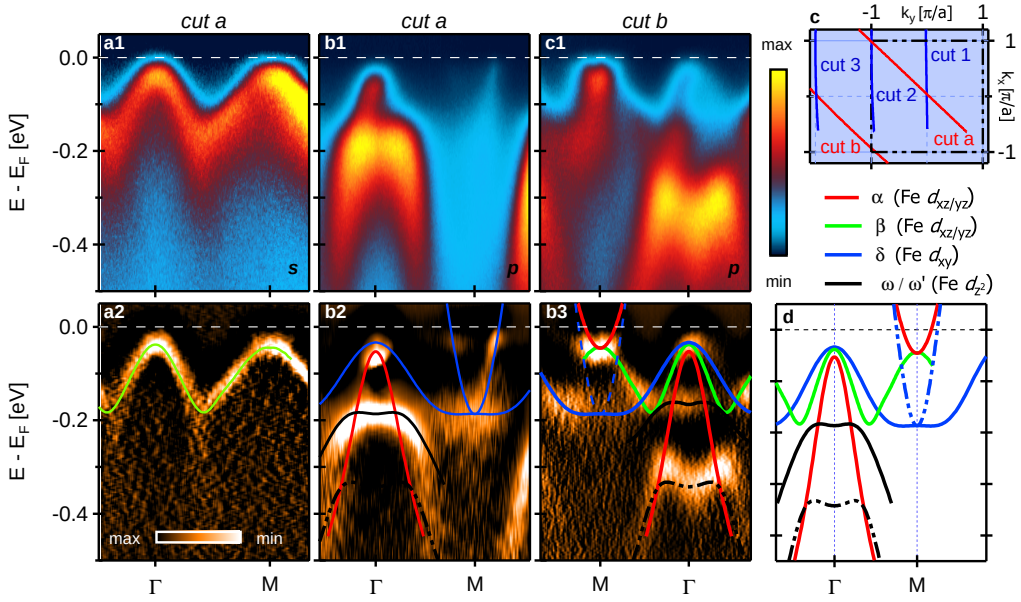

Figure 6.4: ARPES-measured bandstructure along diagonal directions of in the BZ. **(a1) - (c1)** ARPES intensity spectrum along *cut a* and *cut b* as indicated in Figure 6.4 c). The spectra were obtained with $h\nu = 64$ eV photons and the polarization as indicated. **(a2) - (c2)** Curvature plots of spectra presented in a1-c1) obtained by the method as described in Ref. [347]. The renormalized and shifted DFT-calculated bands are overlaid. **(c)** Sketch of the projected BZ. Different diagonal or parallel high symmetry cuts are indicated by red and blue colored lines, respectively. **(d)** Extracted bandstructure along $\Gamma - M$ direction. Colors indicate orbital character of each band.

K suggests that the disappearance of the hole-like FS might be in favor of high temperature superconductivity. The fact that optimally doping of 1111 compounds is at $p \sim 0.3$ suggests that in the case of $Pr_4Fe_2As_2Te_{1-x}O_4$ further electron doping may increase T_c and enlarge the gap between the top of the hole-like band and the Fermi level.

6.5 Conclusion

In summary, by performing high-resolution ARPES measurements we have revealed the electronic structure of $Pr_4Fe_2As_2Te_{0.88}O_4$, for the first time. $Pr_4Fe_2As_2Te_{0.88}O_4$ is a member of the recently discovered 42214 iron-pnictide family which is closely related to the 1111 family. In contrast to ARPES measurements on 1111 compounds, our results don't show any sign of surface states which could provide important insights into the bulk electronic structure of 1111 IBSCs. We have unveiled that all hole-like bands at the BZ-center are below the Fermi level an the FS is formed solely by the electron-like bands located at the BZ-corner. The FS topology resembles that in heavily electron-doped iron-chalcogenides (Li11111) and in monolayer FeSe on STO_3 substrates (FeSe/STO), but is different to the observed FS of all the other superconducting iron-pnictides.

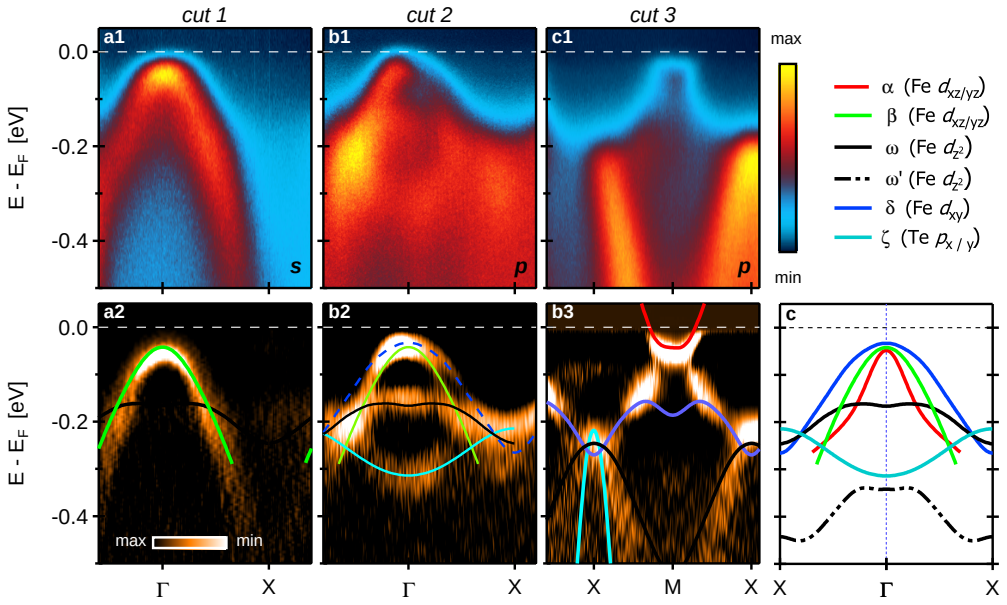

Figure 6.5: ARPES-measured bandstructure along directions parallel to the BZ boundary. **(a1) - (c1)** ARPES intensity spectrum along *cut 1-3* indicated in Figure 6.4 c). The spectra were obtained with $h\nu = 64$ eV photons and the polarization as indicated. **(a2) - (c2)** Curvature plots of spectra presented in a1-c1) obtained by the method as described in Ref. [347]. The renormalized and shifted DFT-calculated bands are overlaid. **(c)** Extracted bandstructure along $\Gamma - M$ direction. Colors indicate orbital character of each band.

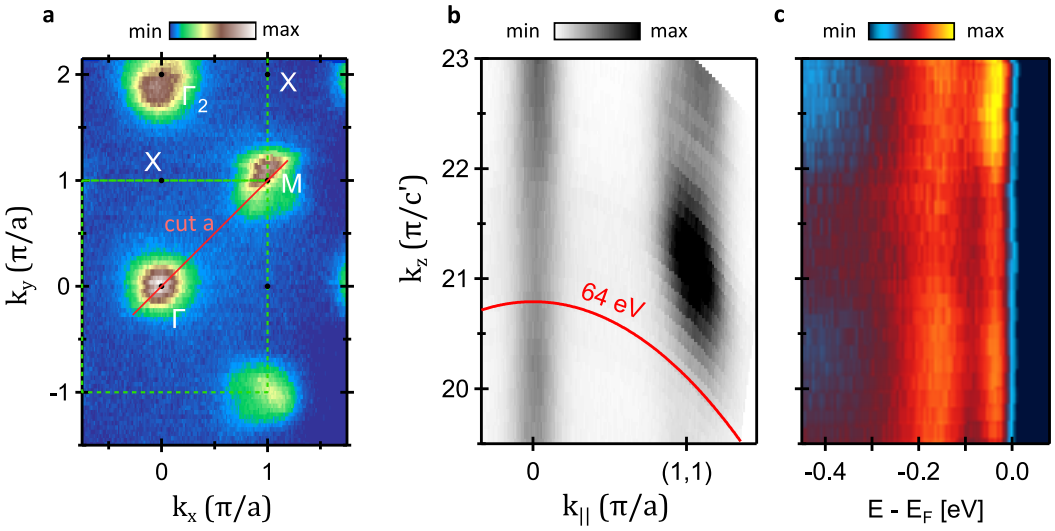

Figure 6.6: **(a)** ARPES intensity map of the in-plane Fermi surface obtained with $h\nu = 64$ eV, circularly polarized photons. The intensity has been integrated over an energy range of ± 10 meV **(b)** Out-of-plane Fermi surface along the diagonal of the BZ (cut a), as indicated in Fig 6.3 a). **c** ARPES-spectrum of the band structure along the $(0,0,k_z)$ direction.

Chapter 7

Conclusions and Outlook

Ever, since the discovery of superconductivity in 1911, there has been a little bit of 'magic' and a lot of 'mystery' in this exciting topic of condensed matter physics [371]. Although conventional superconductivity has been explained by the ground breaking work of J. Bardeen, L. Cooper and J. R. Shrieffer in their "microscopic theory of superconductivity" in 1957, the magic hasn't come to an end [1]. The discovery of high-temperature superconductivity in 1986 by J.G. Bednorz and K.A. Müller reactivated the scientific community which thought that the superconductivity problem has been solved [3]. What followed was an enormous boost of research activity since it was clear that the high-temperature superconductors are fundamentally different from the conventional phonon-mediated superconductors. The discovery of high-T_c superconductivity in iron-pnictides in 2008 has further stimulated the community but despite greatest efforts on the theoretical as well as on the experimental side, the high-T_c problem in either system remains unsolved.
Cuprate and iron-based superconductors belong to the material class of correlated electron systems and have a rich electronic phase diagram. A systematic experimental study of the superconducting state and its adjacent phases might reveal particular features which are responsible for high-T_c superconductivity. As a unique tool which provides direct access to the electronic degrees of freedom in a crystal, ARPES is one of the predestined techniques to reach such an ambitious goal.

In this thesis new results have been presented which might contribute to establish a coherent picture of the electronic phases in cuprates and iron-pnictides.
In chapter 3, a systematic investigation of the low energetic electronic structure of $La_{1.6-x}Nd_{0.4}Sr_xCuO_4$ in a wide doping range ($x = 0.12 - 0.24$) has been presented. The evolution of the EDC-lineshape has been traced as a function of temperature and doping. It has been observed, that the antinodal EDC-lineshape changes drastically depending on the phase in which it has been recorded. In the metallic phase of the overdoped regime ($x = 0.24$), gapless excitations have been found. By entering the pseudogap phase, spectral weight is shifted to higher binding energies and a gap ($\Delta \approx 30$ meV) opens in the single particle excitation spectra. Such a lineshape persists to doping values of $x = 1/8$ at temperatures above the charge-stripe ordering temperature. Upon cooling into to the stripe ordered phase, additional suppression of spectral weight has been observed. Charge-stripe order has been discussed as the responsible reason for this additional suppression. Additionally, in the pseudogap state, a positive correlation between electron scattering and the gap amplitude was observed. In chapter 4, the electronic structure of heavily doped $NaFe_{1-x}Cu_xAs$ ($x = 0.44$) has been presented. $NaFe_{1-x}Cu_xAs$ is the first iron-pnictide system which hosts a superconducting phase in the lightly doped compounds ($x < 0.02$) and becomes an antiferromagnetically ordered insulator for $x > 0.3$. In our combined DFT and ARPES study we have found that the insulating state is induced by strong electronic correlations due to strong and Hund's (J_H) coupling and on-site correlations (U). The effect induced by U and J_H resembles the situation in the parent compounds of the high-T_c cuprates (Mott insulators),

with the charge transfer gap induced by on-site Coulomb interaction that underscores the insulating behavior. The non-Fermi liquid like behavior which is observed in the self energy for $\omega > -200$ meV is interpreted as a further manifestation of strong electron correlations and resembles the results found in cuprate superconductors.

The observation that enhanced electron correlation induce a Mott insulating state in iron-pnictides raises the question about the influence of electronic correlation on superconductivity. The recently discovered 112 family is composed of metallic spacer layers. We revealed, for the first time, the detailed electronic band structure of the spacer layer and found a highly dispersive, almost uncorrelated electronic band structure. We also found that electron correlation in the FeAs layer is not affected by the proximity of the metallic spacer layers. These results are presented in chapter 5.

In combination our observations in $NaFe_{1-x}Cu_xAs$ and $Ca_{1-x}La_xFeAs_2$ suggest that IBSCs might be closer to an insulating state due to on-site Coulomb interactions than so far assumed. We found that electronic correlation is robust against external perturbations and might be one of the key aspects in the search of the description for high-T_c superconductivity. In the case of $Ca_{1-x}La_xFeAs_2$ further studies of the superconducting gap structure would be of high interest. It is expected that superconductivity is also induced into the CaAs layer by the proximity effect. Hence, the gap structure for the bands at $(k_x, k_y) = (1, 0)$ would provide important and new insights into the symmetry of the superconducting gap structure and in general on the pairing mechanism.

A feature of IBSCs which is considered to be highly important for theoretical understanding of high-T_c superconductivity is the FS-topology. In chapter 6 the ARPES study of $Pr_4Fe_2As_2Te_{0.88}O_4$ ($T_c = 25$ K) which belongs to the recently discovered 42214 family unveiled a novel topology of the FS for iron-pnictide superconductors, i.e. a FS consisting solely of electron like sheets in the corner of the BZ. This FS-topology sets strong constraints on the widely discussed FS-nesting based pairing scenario which belongs to the weak coupling theory. Our results suggest that strong electron coupling might be important for superconductivity in the 42214 family.

Additionally, the crystal structure of the 42214 family resembles the one of the 1111 family which hosts the highest T_c in bulk IBSCs. So far, ARPES has not been able to probe the electronic structure of the 1111 family. Hence, our ARPES results may, as well, provide information about the electronic structure of the 1111 family. A next step in the experimental investigation of the 42214 family would be the systematic study of the superconducting gap structure. In addition, the investigation of the FS-evolution as function of doping in $Pr_4Fe_2As_2Te_{1-x}O_4$ would provide further insights on the physics in this iron-pnictide superconductor.

Those are only a few suggestions of a long list with proposals for future experiments which might help to transform a bit of mystery into understanding in the magic field of high-T_c superconductivity.

Bibliography

[1] J. Bardeen, L.N. Cooper, and J.R. Schrieffer. "Theory of Superconductivity". *Phys. Rev.* 108.5 (Dec. 1957), p. 1175.

[2] W. L. McMillan. "Transition Temperature of Strong-Coupled Superconductors". *Physical Review* 167.2 (Mar. 1968), pp. 331–344.

[3] J. G. Bednorz and K. A. Müller. "Possible highTc Superconductivity in the B-La-Cu-O System". *Zeitschrift für Physik B Condensed Matter* 64.2 (1986), pp. 189–193.

[4] Yoichi Kamihara et al. "Iron-Based Layered Superconductor La[$O_{1-x}F_x$]FeAs (x = 0.05-0.12) with Tc = 26 K". *Journal of the American Chemical Society* 130.11 (Mar. 2008), pp. 3296–3297.

[5] Neil W. Ashcroft and N. David Mermin. *Solid State Physics*. English. 1 edition. Brooks Cole, Jan. 1976.

[6] Stefan Cottenier. *Density Functional Theory and the Family of (L)APW-Methods: A Step-by-Step Introduction*. 2nd ed. 2013.

[7] E. Wigner. "Effects of the Electron Interaction on the Energy Levels of Electrons in Metals". en. *Transactions of the Faraday Society* 34.0 (Jan. 1938), pp. 678–685.

[8] N. F. MOTT. "Metal-Insulator Transition". *Reviews of Modern Physics* 40.4 (Oct. 1968), pp. 677–683.

[9] Elbio Dagotto. *Nanoscale Phase Separation and Colossal Magnetoresistance: The Physics of Manganites and Related Compounds*. en. Springer Science & Business Media, Jan. 2003.

[10] Myron B. Salamon and Marcelo Jaime. "The Physics of Manganites: Structure and Transport". *Reviews of Modern Physics* 73.3 (Aug. 2001), pp. 583–628.

[11] P. Coleman. "Heavy Fermions: Electrons at the Edge of Magnetism;" *Wiley: Handbook of Magnetism and Advanced Magnetic Materials, 5 Volume Set - Helmut Kronmuller, Stuart Parkin*. cole. Nov. 2006.

[12] G. R. Stewart. "Heavy-Fermion Systems". *Reviews of Modern Physics* 56.4 (Oct. 1984), pp. 755–787.

[13] Pia Jensen Ray. *Masters thesis, "Structural investigation of $La_{2-x}Sr_xCuO_{4+y}$ - Following staging as a function of temperature"*. Tech. rep. Copenhagen, Denmark: Niels Bohr Institute, Faculty of Science, University of Copenhagen., 2015.

[14] M. K. Wu et al. "Superconductivity at 93 K in a New Mixed-Phase Y-Ba-Cu-O Compound System at Ambient Pressure". *Physical Review Letters* 58.9 (Mar. 1987), pp. 908–910.

[15] A. Schilling et al. "Superconductivity above 130 K in the Hg–Ba–Ca–Cu–O System". en. *Nature* 363.6424 (May 1993), pp. 56–58.

[16] C. W. Chu et al. "Superconductivity above 150 K in HgBa2Ca2Cu3O8+δ at High Pressures". en. *Nature* 365.6444 (Sept. 1993), pp. 323–325.

[17] Cao Wang et al. “Thorium-doping-induced superconductivity up to 56 K in $Gd_{1x}Th_xFeAsO$”. en. *EPL (Europhysics Letters)* 83.6 (2008), p. 67006.

[18] H.K. Onnes. *Commun. Phys. Lab. Univ. Leiden* vol. 120b,122b,124c (1911).

[19] (Mai 2016) null. *Superconductivity 101 - MagLab*. `https://nationalmaglab.org/education/magnet-academy/learn-the-basics/stories/superconductivity-101`.

[20] Reinhold Kleiner et al. “Fundamentals”. en. *Applied Superconductivity*. Ed. by Paul Seidel. Wiley-VCH Verlag GmbH & Co. KGaA, 2015, pp. 1–104.

[21] W. Meissner and R. Ochsenfeld. “Ein neuer Effekt bei Eintritt der Supraleitfähigkeit”. de. *Naturwissenschaften* 21.44 (Nov. 1933), pp. 787–788.

[22] F. London and H. London. “The Electromagnetic Equations of the Supraconductor”. *Proc Roy Soc London* A149 (1935), p. 71.

[23] V.L. Ginzburg and L.D. Landau. *Zh. Eksperim. i Teor. Fiz.* 20 (1950), p. 1064.

[24] Michael Tinkham. *Introduction to Superconductivity: Second Edition*. English. Second Edition edition. Mineola, N.Y.: Dover Publications, June 2004.

[25] A. S. Alexandrov. *Theory of Superconductivity: From Weak to Strong Coupling*. en. CRC Press, Oct. 2003.

[26] P. G. De Gennes. *Superconductivity Of Metals And Alloys*. English. Reading, Mass.: Westview Press, Mar. 1999.

[27] Leon N. Cooper. “Bound Electron Pairs in a Degenerate Fermi Gas”. *Physical Review* 104.4 (Nov. 1956), pp. 1189–1190.

[28] http://wyvern.phys.s.u-tokyo.ac.jp/f/Research/hts_en.htm. *High-Temperature Superconductivity*. `http://wyvern.phys.s.u-tokyo.ac.jp/f/Research/hts_en.htm`.

[29] Neven Barišić et al. “Universal Sheet Resistance and Revised Phase Diagram of the Cuprate High-Temperature Superconductors”. en. *Proceedings of the National Academy of Sciences* 110.30 (July 2013), pp. 12235–12240.

[30] Patrick A. Lee, Naoto Nagaosa, and Xiao-Gang Wen. “Doping a Mott Insulator: Physics of High-Temperature Superconductivity”. *Reviews of Modern Physics* 78.1 (Jan. 2006), pp. 17–85.

[31] D. J. Scalapino. “The case for $d_{x^2y^2}$ pairing in the cuprate superconductors”. *Physics Reports* 250.6 (Jan. 1995), pp. 329–365.

[32] A. P. Drozdov et al. “Conventional Superconductivity at 203 Kelvin at High Pressures in the Sulfur Hydride System”. en. *Nature* 525.7567 (Sept. 2015), pp. 73–76.

[33] C. C. Tsuei and J. R. Kirtley. “Pairing Symmetry in Cuprate Superconductors”. *Reviews of Modern Physics* 72.4 (Oct. 2000), pp. 969–1016.

[34] Johnpierre Paglione and Richard L. Greene. “High-Temperature Superconductivity in Iron-Based Materials”. *Nat Phys* 6.9 (Sept. 2010), pp. 645–658.

[35] H.-J. Grafe et al. “75 As NMR Studies of Superconducting $LaFeAsO_{0.9}F_{0.1}$”. *Physical Review Letters* 101.4 (July 2008), p. 047003.

[36] Fanlong Ning et al. “59Co and 75As NMR Investigation of Electron-Doped High Tc Superconductor BaFe1.8Co0.2As2 (Tc = 22 K)”. *Journal of the Physical Society of Japan* 77.10 (Sept. 2008), p. 103705.

[37] Andrew Peter Mackenzie and Yoshiteru Maeno. “The superconductivity of Sr_2RuO_4 and the physics of spin-triplet pairing”. *Reviews of Modern Physics* 75.2 (May 2003), pp. 657–712.

[38] N. Byers and C. N. Yang. “Theoretical Considerations Concerning Quantized Magnetic Flux in Superconducting Cylinders”. *Physical Review Letters* 7.2 (July 1961), pp. 46–49.

[39] C. E. Gough et al. “Flux Quantization in a High-Tc Superconductor”. en. *Nature* 326.6116 (Apr. 1987), pp. 855–855.

[40] C.-T. Chen et al. “Integer and Half-Integer Flux-Quantum Transitions in a Niobium–iron Pnictide Loop”. en. *Nature Physics* 6.4 (Apr. 2010), pp. 260–264.

[41] Ajay Kumar Saxena. *High-Temperature Superconductors*. English. 2nd ed. 2012 edition. Place of publication not identified: Springer, Aug. 2014.

[42] Ajay Kumar Saxena. “Crystal Structure of High Temperature Superconductors”. en. *High-Temperature Superconductors*. Springer Series in Materials Science 125. Springer Berlin Heidelberg, 2012, pp. 43–60.

[43] J. M. Tarascon et al. “Preparation, structure, and properties of the superconducting compound series $Bi_2Sr_2Ca_{n-1}Cu_nO_y$ with $n = 1, 2, \text{and} 3$”. *Physical Review B* 38.13 (Nov. 1988), pp. 8885–8892.

[44] Andrea Damascelli, Zahid Hussain, and Zhi-Xun Shen. “Angle-Resolved Photoemission Studies of the Cuprate Superconductors”. *Rev. Mod. Phys.* 75.2 (Apr. 2003), pp. 473–541.

[45] Peter Fulde. *Electron Correlations in Molecules and Solids*. en. Springer Science & Business Media, 1995.

[46] L. F. Mattheiss. “Electronic band properties and superconductivity in $La_{2-y}X_yCuO_4$”. *Physical Review Letters* 58.10 (Mar. 1987), pp. 1028–1030.

[47] J. Fink et al. “Electronic Structure Studies of High-Tc Superconductors by High-Energy Spectroscopies”. *IBM Journal of Research and Development* 33.3 (May 1989), pp. 372–381.

[48] X. J. Zhou et al. “Angle-Resolved Photoemission Spectroscopy on Electronic Structure and lectron–Phonon Coupling in Cuprate Superconductors”. en. *Handbook of High-Temperature Superconductivity*. Ed. by J. Robert Schrieffer and James S. Brooks. Springer New York, 2007, pp. 87–144.

[49] C. M. Varma, S. Schmitt-Rink, and Elihu Abrahams. “Charge Transfer Excitations and Superconductivity in “ionic” Metals”. *Solid State Communications* 62.10 (June 1987), pp. 681–685.

[50] S. Uchida et al. “Optical spectra of $La_{2-x}Sr_xCuO_4$: Effect of carrier doping on the electronic structure of the CuO_2 plane”. *Physical Review B* 43.10 (Apr. 1991), pp. 7942–7954.

[51] D. Vaknin et al. “Antiferromagnetism in La_2CuO_{4-y}”. *Physical Review Letters* 58.26 (June 1987), pp. 2802–2805.

[52] N. F. Mott. “The Basis of the Electron Theory of Metals, with Special Reference to the Transition Metals”. en. *Proceedings of the Physical Society. Section A* 62.7 (1949), p. 416.

[53] N. F. Mott. “On the Transition to Metallic Conduction in Semiconductors”. *Canadian Journal of Physics* 34.12A (Dec. 1956), pp. 1356–1368.

[54] P. W. Anderson. “New Approach to the Theory of Superexchange Interactions”. *Physical Review* 115.1 (July 1959), pp. 2–13.

[55] J. Zaanen, G. A. Sawatzky, and J. W. Allen. “Band Gaps and Electronic Structure of Transition-Metal Compounds”. *Physical Review Letters* 55.4 (July 1985), pp. 418–421.

[56] B. Keimer et al. “From Quantum Matter to High-Temperature Superconductivity in Copper Oxides”. en. *Nature* 518.7538 (Feb. 2015), pp. 179–186.

[57] Y. Ando et al. “Mobility of the Doped Holes and the Antiferromagnetic Correlations in Underdoped High- Tc Cuprates”. eng. *Physical Review Letters* 87.1 (July 2001), p. 017001.

[58] A. P. Mackenzie et al. “Normal-state magnetotransport in superconducting $Tl_2Ba_2CuO_{6+\delta}$ to millikelvin temperatures”. *Physical Review B* 53.9 (Mar. 1996), pp. 5848–5855.

[59] Riccardo Comin and Andrea Damascelli. “Resonant X-Ray Scattering Studies of Charge Order in Cuprates”. *Annual Review of Condensed Matter Physics* 7.1 (2016), pp. 369–405.

[60] Debanjan Chowdhury and Subir Sachdev. “The Enigma of the Pseudogap Phase of the Cuprate Superconductors”. *Quantum Criticality in Condensed Matter*. WORLD SCIENTIFIC, May 2015, pp. 1–43.

[61] Louis Taillefer. “Scattering and Pairing in Cuprate Superconductors”. *Annual Review of Condensed Matter Physics* 1.1 (2010), pp. 51–70.

[62] E. Miranda and V. Dobrosavljević. “Disorder-Driven Non-Fermi Liquid Behaviour of Correlated Electrons”. en. *Reports on Progress in Physics* 68.10 (2005), p. 2337.

[63] V. I. Anisimov et al. “Density-Functional Calculation of the Coulomb Repulsion and Correlation Strength in Superconducting LaFeAsO”. en. *JETP Letters* 88.11 (May 2009), pp. 729–733.

[64] M. A. Kastner et al. “Magnetic, Transport, and Optical Properties of Monolayer Copper Oxides”. *Reviews of Modern Physics* 70.3 (July 1998), pp. 897–928.

[65] Daniel I. Khomskii. *Basic Aspects of the Quantum Theory of Solids: Order and Elementary Excitations*. en. Cambridge University Press, Sept. 2010.

[66] R. Coldea et al. “Spin Waves and Electronic Interactions in La_2CuO_4”. *Physical Review Letters* 86.23 (June 2001), pp. 5377–5380.

[67] P. E. Sulewski et al. “Light scattering from quantum spin fluctuations in R_2CuO_4 (R= La, Nd, Sm)”. *Physical Review B* 41.1 (Jan. 1990), pp. 225–230.

[68] Philip Phillips. *Advanced Solid State Physics*. English. 2 edition. Cambridge ; New York: Cambridge University Press, Apr. 2012.

[69] E. M. Lifshitz and L. P. Pitaevskii. *Statistical Physics: Theory of the Condensed State*. English. Oxford: Butterworth-Heinemann, Jan. 1980.

[70] Takashi Manako, Yoshimi Kubo, and Yuichi Shimakawa. “Transport and structural study of $Tl_2Ba_2CuO_{6+\delta}$ single crystals prepared by the KCl flux method”. *Physical Review B* 46.17 (Nov. 1992), pp. 11019–11024.

[71] S. Nakamae et al. “Electronic ground state of heavily overdoped nonsuperconducting $La_{2-x}Sr_xCuO_4$”. *Physical Review B* 68.10 (Sept. 2003), p. 100502.

[72] Cyril Proust et al. “Heat Transport in a Strongly Overdoped Cuprate: Fermi Liquid and a Pure d-Wave BCS Superconductor”. *Physical Review Letters* 89.14 (Sept. 2002), p. 147003.

[73] M. Platé et al. “Fermi Surface and Quasiparticle Excitations of Overdoped $Tl_2Ba_2CuO_{6+\delta}$”. *Physical Review Letters* 95.7 (Aug. 2005), p. 077001.

[74] H. Ding et al. “Angle-resolved photoemission spectroscopy study of the superconducting gap anisotropy in $Bi_2Sr_2CaCu_2O_{8+x}$”. *Phys. Rev. B* 54.14 (Oct. 1996), R9678–R9681.

[75] C. C. Tsuei et al. “Pairing Symmetry and Flux Quantization in a Tricrystal Superconducting Ring of $YBa_2Cu_3O_{7-\delta}$”. *Physical Review Letters* 73.4 (July 1994), pp. 593–596.

[76] H. Takagi. “Systematic Evolution of Temperature-Dependent Resistivity in LSCO”. *Physical Review Letters* 69.20 (1992), pp. 2975–2978.

[77] S. Martin et al. “Normal-state transport properties of $Bi_{2+x}Sr_{2-y}CuO_{6+\delta}$ crystals”. *Physical Review B* 41.1 (Jan. 1990), pp. 846–849.

[78] T. R. Chien, Z. Z. Wang, and N. P. Ong. "Effect of Zn impurities on the normal-state Hall angle in single-crystal $YBa_2Cu_{3-x}Zn_xO_{7-\delta}$". *Physical Review Letters* 67.15 (Oct. 1991), pp. 2088–2091.

[79] Cyril Proust et al. "Heat transport in $Bi_{2+x}Sr_{2-x}CuO_{6+\delta}$: Departure from the Wiedemann-Franz law in the vicinity of the metal-insulator transition". *Physical Review B* 72.21 (Dec. 2005), p. 214511.

[80] C. M. Varma et al. "Phenomenology of the Normal State of Cu-O High-Temperature Superconductors". *Physical Review Letters* 63.18 (Oct. 1989), pp. 1996–1999.

[81] M. R. Norman, D. Pines, and C. Kallin. "The Pseudogap: Friend or Foe of High T c ?" *Advances in Physics* 54.8 (2005), pp. 715–733.

[82] W. W. Warren et al. "Cu spin dynamics and superconducting precursor effects in planes above T_c in $YBa_2Cu_3O_{6.7}$". *Physical Review Letters* 62.10 (Mar. 1989), pp. 1193–1196.

[83] H. Alloul, T. Ohno, and P. Mendels. "^{89}Y NMR evidence for a fermi-liquid behavior in $YBa_2Cu_3O_{6+x}$". *Physical Review Letters* 63.16 (Oct. 1989), pp. 1700–1703.

[84] M. R. Norman et al. "Destruction of the Fermi Surface in Underdoped High-Tc Superconductors". en. *Nature* 392.6672 (Mar. 1998), pp. 157–160.

[85] D. S. Marshall et al. "Unconventional Electronic Structure Evolution with Hole Doping in $Bi_2Sr_2CaCu_2O_{8+\delta}$: Angle-Resolved Photoemission Results". *Physical Review Letters* 76.25 (June 1996), pp. 4841–4844.

[86] Tom Timusk and Bryan Statt. "The Pseudogap in High-Temperature Superconductors: An Experimental Survey". en. *Reports on Progress in Physics* 62.1 (1999), p. 61.

[87] Teppei Yoshida et al. "Pseudogap, Superconducting Gap, and Fermi Arc in High-Tc Cuprates Revealed by Angle-Resolved Photoemission Spectroscopy". *Journal of the Physical Society of Japan* 81.1 (Dec. 2011), p. 011006.

[88] J. M. Tranquada et al. "Evidence for Stripe Correlations of Spins and Holes in Copper Oxide Superconductors". *Nature* 375 (1995), pp. 561–563.

[89] M. Hücker et al. "Enhanced charge stripe order of superconducting $La_{2-x}Ba_xCuO_4$ in a magnetic field". *Physical Review B* 87.1 (Jan. 2013), p. 014501.

[90] J. Chang et al. "Direct observation of competition between superconductivity and charge density wave order in $YBa_2Cu_3O_{6.67}$". en. *Nature Physics* 8.12 (Dec. 2012), pp. 871–876.

[91] G. Ghiringhelli et al. "Long-Range Incommensurate Charge Fluctuations in $(Y,Nd)Ba_2Cu_3O_{6+x}$". en. *Science* 337.6096 (Aug. 2012), pp. 821–825.

[92] M. Le Tacon et al. "Inelastic X-Ray Scattering in YBa2Cu3O6.6 Reveals Giant Phonon Anomalies and Elastic Central Peak due to Charge-Density-Wave Formation". en. *Nature Physics* 10.1 (Jan. 2014), pp. 52–58.

[93] "Towards a Complete Theory of High Tc". en. *Nature Physics* 2.3 (Mar. 2006), pp. 138–143.

[94] Adrian Cho. "High Tc: The Mystery That Defies Solution". en. *Science* 314.5802 (Nov. 2006), pp. 1072–1075.

[95] Tôru Moriya and Kazuo Ueda. "Antiferromagnetic Spin Fluctuation and Superconductivity". en. *Reports on Progress in Physics* 66.8 (2003), p. 1299.

[96] Andrey V. Chubukov and Dirk K. Morr. "Electronic Structure of Underdoped Cuprates". *Physics Reports* 288.1 (Sept. 1997), pp. 355–387.

[97] P. W. Anderson. "The Resonating Valence Bond State in La2CuO4 and Superconductivity". en. *Science* 235.4793 (Mar. 1987), pp. 1196–1198.

[98] P. W. Anderson et al. “The Physics behind High-Temperature Superconducting Cuprates: The 'plain Vanilla' Version of RVB”. en. *Journal of Physics: Condensed Matter* 16.24 (2004), R755.

[99] C. M. Varma. “Non-Fermi-Liquid States and Pairing Instability of a General Model of Copper Oxide Metals”. *Physical Review B* 55.21 (June 1997), pp. 14554–14580.

[100] C. M. Varma. “Pseudogap Phase and the Quantum-Critical Point in Copper-Oxide Metals”. *Physical Review Letters* 83.17 (Oct. 1999), pp. 3538–3541.

[101] Sudip Chakravarty et al. “Hidden Order in the Cuprates”. *Physical Review B* 63.9 (Jan. 2001), p. 094503.

[102] Matthias Vojta, Ying Zhang, and Subir Sachdev. “Quantum Phase Transitions in d-Wave Superconductors”. *Physical Review Letters* 85.23 (Dec. 2000), pp. 4940–4943.

[103] S. A. Kivelson, E. Fradkin, and V. J. Emery. “Electronic Liquid-Crystal Phases of a Doped Mott Insulator”. en. *Nature* 393.6685 (June 1998), pp. 550–553.

[104] S. A. Kivelson et al. “How to Detect Fluctuating Stripes in the High-Temperature Superconductors”. *Reviews of Modern Physics* 75.4 (Oct. 2003), pp. 1201–1241.

[105] Nuh Gedik et al. “Nonequilibrium Phase Transitions in Cuprates Observed by Ultrafast Electron Crystallography”. en. *Science* 316.5823 (Apr. 2007), pp. 425–429.

[106] Jinho Lee et al. “Interplay of electronlattice interactions and superconductivity in Bi2Sr2CaCu2O8+”. en. *Nature* 442.7102 (Aug. 2006), pp. 546–550.

[107] C. W. Chu. “High-Temperature Superconductivity: Alive and Kicking”. en. *Nature Physics* 5.11 (Nov. 2009), pp. 787–789.

[108] S. Fujitsu, S. Matsuishi, and H. Hosono. “Iron Based Superconductors Processing and Properties”. *International Materials Reviews* 57.6 (Nov. 2012), pp. 311–327.

[109] G. R. Stewart. “Superconductivity in Iron Compounds”. *Rev. Mod. Phys.* 83.4 (Dec. 2011), pp. 1589–1652.

[110] Peter D. Johnson, Guangyong Xu, and Wei-Guo Yin, eds. *Iron-Based Superconductivity*. Vol. 211. Springer Series in Materials Science. Cham: Springer International Publishing, 2015.

[111] David C. Johnston. “The Puzzle of High Temperature Superconductivity in Layered Iron Pnictides and Chalcogenides”. *Advances in Physics* 59.6 (Nov. 2010), pp. 803–1061.

[112] Zhi-An Ren et al. “Superconductivity and Phase Diagram in Iron-Based Arsenic-Oxides ReFeAsO 1-δ (Re = Rare-Earth Metal) without Fluorine Doping”. en. *EPL (Europhysics Letters)* 83.1 (2008), p. 17002.

[113] Hideo Hosono et al. “Exploration of New Superconductors and Functional Materials, and Fabrication of Superconducting Tapes and Wires of Iron Pnictides”. *Science and Technology of Advanced Materials* 16.3 (June 2015), p. 033503.

[114] D. J. Singh. “Electronic structure and doping in $BaFe_2As_2$ and LiFeAs: Density functional calculations”. *Physical Review B* 78.9 (Sept. 2008), p. 094511.

[115] S. Graser et al. “Near-Degeneracy of Several Pairing Channels in Multiorbital Models for the Fe Pnictides”. en. *New Journal of Physics* 11.2 (2009), p. 025016.

[116] H. Ding et al. “Observation of Fermi-surfacedependent nodeless superconducting gaps in Ba 0.6 K 0.4 Fe 2 As 2”. en. *EPL (Europhysics Letters)* 83.4 (2008), p. 47001.

[117] M. J. Calderón, B. Valenzuela, and E. Bascones. “Tight-Binding Model for Iron Pnictides”. *Physical Review B* 80.9 (Sept. 2009), p. 094531.

[118] K. Haule and G. Kotliar. “Coherence–incoherence Crossover in the Normal State of Iron Oxypnictides and Importance of Hund's Rule Coupling”. en. *New Journal of Physics* 11.2 (2009), p. 025021.

[119] V. Brouet et al. “Impact of the Two Fe Unit Cell on the Electronic Structure Measured by ARPES in Iron Pnictides”. *Physical Review B* 86.7 (Aug. 2012), p. 075123.

[120] P. L. Bach et al. “High-Temperature Resistivity in the Iron Pnictides and the Electron-Doped Cuprates”. *Phys. Rev. B* 83.21 (June 2011), p. 212506.

[121] Qimiao Si, Rong Yu, and Elihu Abrahams. “High-Temperature Superconductivity in Iron Pnictides and Chalcogenides”. *Nature Reviews Materials* (Mar. 2016), p. 16017.

[122] Z. P. Yin, K. Haule, and G. Kotliar. “Kinetic Frustration and the Nature of the Magnetic and Paramagnetic States in Iron Pnictides and Iron Chalcogenides”. en. *Nature Materials* 10.12 (Dec. 2011), pp. 932–935.

[123] P. Richard et al. “Fe-Based Superconductors: An Angle-Resolved Photoemission Spectroscopy Perspective”. *Reports on Progress in Physics* 74.12 (2011), p. 124512.

[124] M. M. Qazilbash et al. “Electronic Correlations in the Iron Pnictides”. en. *Nature Physics* 5.9 (Sept. 2009), pp. 647–650.

[125] E. Razzoli et al. “Bulk Electronic Structure of Superconducting $LaRu_2\mathbf{P}_2$ Single Crystals Measured by Soft-X-Ray Angle-Resolved Photoemission Spectroscopy”. *Physical Review Letters* 108.25 (June 2012), p. 257005.

[126] Luca de’ Medici, Gianluca Giovannetti, and Massimo Capone. “Selective Mott Physics as a Key to Iron Superconductors”. *Phys. Rev. Lett.* 112.17 (Apr. 2014), p. 177001.

[127] Antoine Georges, Luca de’Medici, and Jernej Mravlje. “Strong Correlations from Hund’s Coupling”. *Annual Review of Condensed Matter Physics* 4.1 (2013), pp. 137–178.

[128] Takashi Miyake et al. “Comparison of Ab Initio Low-Energy Models for LaFePO, LaFeAsO, BaFe2As2, LiFeAs, FeSe, and FeTe: Electron Correlation and Covalency”. *Journal of the Physical Society of Japan* 79.4 (Mar. 2010), p. 044705.

[129] Hideo Aoki and Hideo Hosono. “A Superconducting Surprise Comes of Age”. en. *Physics World* 28.2 (2015), p. 31.

[130] S. Kasahara et al. “Evolution from non-Fermi- to Fermi-liquid transport via isovalent doping in $BaFe_2(As_{1-x}P_x)_2$ superconductors”. *Physical Review B* 81.18 (May 2010), p. 184519.

[131] H. Chen et al. “Coexistence of the Spin-Density Wave and Superconductivity in Ba1-xKxFe2As2”. en. *EPL (Europhysics Letters)* 85.1 (2009), p. 17006.

[132] Takehiro Yamazaki et al. “Appearance of Pressure-Induced Superconductivity in \${\text{BaFe}}_{2}{\text{As}}_{2}\$ under Hydrostatic Conditions and Its Extremely High Sensitivity to Uniaxial Stress”. *Physical Review B* 81.22 (June 2010), p. 224511.

[133] Awadhesh Mani et al. “Pressure-Induced Superconductivity in BaFe 2 As 2 Single Crystal”. en. *EPL (Europhysics Letters)* 87.1 (2009), p. 17004.

[134] A. B. Vorontsov, M. G. Vavilov, and A. V. Chubukov. “Interplay between Magnetism and Superconductivity in the Iron Pnictides”. *Physical Review B* 79.6 (Feb. 2009), p. 060508.

[135] Qimiao Si and Elihu Abrahams. “Strong Correlations and Magnetic Frustration in the High \${T}_{c}\$ Iron Pnictides”. *Physical Review Letters* 101.7 (Aug. 2008), p. 076401.

[136] Pengcheng Dai, Huiqian Luo, and Meng Wang. “Magnetic Order and Dynamics: Neutron Scattering”. en. *Iron-Based Superconductivity*. Ed. by Peter D. Johnson, Guangyong Xu, and Wei-Guo Yin. Springer Series in Materials Science 211. Springer International Publishing, 2015, pp. 151–186.

[137] Pengcheng Dai, Jiangping Hu, and Elbio Dagotto. “Magnetism and Its Microscopic Origin in Iron-Based High-Temperature Superconductors”. en. *Nature Physics* 8.10 (Oct. 2012), pp. 709–718.

[138] Pengcheng Dai. "Antiferromagnetic Order and Spin Dynamics in Iron-Based Superconductors". *Reviews of Modern Physics* 87.3 (Aug. 2015), pp. 855–896.

[139] I. I. Mazin et al. "Unconventional Superconductivity with a Sign Reversal in the Order Parameter of $LaFeAsO_{1-x}F_x$". *Physical Review Letters* 101.5 (July 2008), p. 057003.

[140] I. I. Mazin and J. Schmalian. "Pairing Symmetry and Pairing State in Ferropnictides: Theoretical Overview". *Physica C: Superconductivity*. Superconductivity in Iron-Pnictides 469.9–12 (June 2009), pp. 614–627.

[141] D. S. Inosov et al. "Normal-State Spin Dynamics and Temperature-Dependent Spin-Resonance Energy in Optimally Doped BaFe1.85Co0.15As2". en. *Nature Physics* 6.3 (Mar. 2010), pp. 178–181.

[142] J.-P. Castellan et al. "Effect of Fermi Surface Nesting on Resonant Spin Excitations in $Ba_{1-x}K_xFe_2As_2$". *Physical Review Letters* 107.17 (Oct. 2011), p. 177003.

[143] A. D. Christianson et al. "Unconventional Superconductivity in Ba0.6K0.4Fe2As2 from Inelastic Neutron Scattering". en. *Nature* 456.7224 (Dec. 2008), pp. 930–932.

[144] T. Hanaguri et al. "Unconventional S-Wave Superconductivity in Fe(Se,Te)". en. *Science* 328.5977 (Apr. 2010), pp. 474–476.

[145] Andrey Chubukov. "Itinerant Electron Scenario". en. *Iron-Based Superconductivity*. Ed. by Peter D. Johnson, Guangyong Xu, and Wei-Guo Yin. Springer Series in Materials Science 211. Springer International Publishing, 2015, pp. 255–329.

[146] Kangjun Seo, B. Andrei Bernevig, and Jiangping Hu. "Pairing Symmetry in a Two-Orbital Exchange Coupling Model of Oxypnictides". *Physical Review Letters* 101.20 (Nov. 2008), p. 206404.

[147] Mona Berciu, Ilya Elfimov, and George A. Sawatzky. "Electronic Polarons and Bipolarons in Iron-Based Superconductors: The Role of Anions". *Physical Review B* 79.21 (June 2009), p. 214507.

[148] G. A. Sawatzky et al. "Heavy-Anion Solvation of Polarity Fluctuations in Pnictides". en. *EPL (Europhysics Letters)* 86.1 (2009), p. 17006.

[149] V. J. Emery and S. A. Kivelson. "Importance of Phase Fluctuations in Superconductors with Small Superfluid Density". en. *Nature* 374.6521 (Mar. 1995), pp. 434–437.

[150] Karl-Heinz Bennemann and John B. Ketterson, eds. *Superconductivity: Volume 1: Conventional and Unconventional Superconductors Volume 2: Novel Superconductors*. English. 2008 edition. Berlin ; London: Springer, June 2008.

[151] E. Razzoli et al. "Evolution from a Nodeless Gap to $d_{x^2-y^2}$-Wave in Underdoped $La_{2-x}Sr_xCuO_4$". *Physical Review Letters* 110.4 (Jan. 2013), p. 047004.

[152] Philip W. Anderson. "Is There Glue in Cuprate Superconductors?" en. *Science* 316.5832 (June 2007), pp. 1705–1707.

[153] Peter Blaha et al. *An Augmented Plane Wave + Local Orbitals Program for Calculating Crystal Properties - User Guide*. June 2013.

[154] P. Hohenberg and W. Kohn. "Inhomogeneous Electron Gas". *Physical Review* 136.3B (Nov. 1964), B864–B871.

[155] Klaus Capelle. "A Bird's-Eye View of Density-Functional Theory". *Brazilian Journal of Physics* 36.4A (Dec. 2006), pp. 1318–1343.

[156] W. Kohn and L. J. Sham. "Self-Consistent Equations Including Exchange and Correlation Effects". *Physical Review* 140.4A (Nov. 1965), A1133–A1138.

[157] David Sholl and Janice A. Steckel. *Density Functional Theory: A Practical Introduction*. English. 1 edition. Hoboken, N.J: Wiley-Interscience, Apr. 2009.

[158] Richard M. Martin. *Electronic Structure: Basic Theory and Practical Methods*. English. 1 edition. Cambridge, UK ; New York: Cambridge University Press, Oct. 2008.

[159] Peter Blaha et al. "Wien2k: An Augmented Plane Wave + Local Orbitals Program for Calculating Crystal Properties (Vienna University of Technology, Vienna, 2001)". *Wien2k: An Augmented Plane Wave + Local Orbitals Program for Calculating Crystal Properties (Vienna University of Technology, Vienna, 2001)* (2001).

[160] Carl Nordling, Evelyn Sokolowski, and Kai Siegbahn. "Precision Method for Obtaining Absolute Values of Atomic Binding Energies". *Phys. Rev.* 105.5 (Mar. 1957), pp. 1676–1677.

[161] C. N. Berglund and W. E. Spicer. "Photoemission Studies of Copper and Silver: Theory". *Phys. Rev.* 136.4A (Nov. 1964), A1030–A1044.

[162] C. N. Berglund and W. E. Spicer. "Photoemission Studies of Copper and Silver: Experiment". *Phys. Rev.* 136.4A (Nov. 1964), A1044–A1064.

[163] E. O. Kane. "Implications of Crystal Momentum Conservation in Photoelectric Emission for Band-Structure Measurements". *Phys. Rev. Lett.* 12.4 (Jan. 1964), pp. 97–98.

[164] Neville V. Smith, Morton M. Traum, and F. J. Di Salvo. "Mapping Energy Bands in Layer Compounds from the Angular Dependence of Ultraviolet Photoemission". *Solid State Communications* 15.2 (1974), pp. 211 –214.

[165] Morton M. Traum, Neville V. Smith, and F. J. Di Salvo. "Angular Dependence of Photoemission and Atomic Orbitals in the Layer Compound $1T-\mathrmTa\mathrmSe_2$". *Phys. Rev. Lett.* 32.22 (June 1974), pp. 1241–1244.

[166] S. V. Borisenko et al. "Two Energy Gaps and Fermi-Surface "Arcs" in $NbSe_2$". *Physical Review Letters* 102.16 (Apr. 2009), p. 166402.

[167] C.E. Matt et al. "Electron scattering, charge order, and pseudogap physics in $La_{1.6x}Nd_{0.4}Sr_xCuO_4$: An angle-resolved photoemission spectroscopy study". *Phys. Rev. B* 92.13 (Oct. 2015), p. 134524.

[168] N. C. Plumb et al. "Low-Energy ($ \textless 10\mathrm meV$) Feature in the Nodal Electron Self-Energy and Strong Temperature Dependence of the Fermi Velocity in $\mathrmBi_2\mathrmSr_2\mathrmCaCu_2\mathbfO_8+\ensuremath\delta$". *Phys. Rev. Lett.* 105.4 (July 2010), p. 046402.

[169] X. J. Zhou et al. "High-Temperature Superconductors: Universal Nodal Fermi Velocity". *Nature* 423.6938 (May 2003), pp. 398–398.

[170] H. Ding et al. "Evolution of the Fermi Surface with Carrier Concentration in $Bi_2Sr_2CaCu_2O_{8+\delta}$". *Physical Review Letters* 78.13 (Mar. 1997), pp. 2628–2631.

[171] T. Yoshida et al. "Systematic doping evolution of the underlying Fermi surface of $La_{2-x}Sr_xCuO_4$". *Physical Review B* 74.22 (Dec. 2006), p. 224510.

[172] D. H. Lu et al. "Electronic Structure of the Iron-Based Superconductor LaOFeP". *Nature* 455.7209 (Sept. 2008), pp. 81–84.

[173] M. Z. Hasan and C. L. Kane. "*Colloquium* : Topological Insulators". *Rev. Mod. Phys.* 82.4 (Nov. 2010), pp. 3045–3067.

[174] Xiao-Liang Qi and Shou-Cheng Zhang. "Topological Insulators and Superconductors". *Rev. Mod. Phys.* 83.4 (Oct. 2011), pp. 1057–1110.

[175] B. Q. Lv et al. "Observation of Weyl Nodes in TaAs". *Nat Phys* 11.9 (Sept. 2015), pp. 724–727.

[176] Stefan Hüfner. *Photoelectron Spectroscopy*. Advanced Texts in Physics. Berlin, Heidelberg: Springer Berlin Heidelberg, 2003.

[177] Charles C. Chusuei and D. Wayne Goodman. "X-Ray Photoelectron Spectroscopy". *Encyclopedia of Physical Science and Technology (Third Edition)*. Ed. by Robert A. Meyers. Third Edition. New York: Academic Press, 2003, pp. 921 –938.

[178] Rudy Schlaf. *Calibration of Photoemission Spectra and Work Function Determination*.

[179] Wolfgang Schattke and Michel A. Van Hove. *Solid-State Photoemission and Related Methods: Theory and Experiment*. en. John Wiley & Sons, Nov. 2003.

[180] L. Hedin and J. D. Lee. "Sudden Approximation in Photoemission and beyond". *Journal of Electron Spectroscopy and Related Phenomena* 124.2–3 (2002). Frontiers in photoemission spectroscopy of solids and surfaces, pp. 289 –315.

[181] Henrik Bruus and Karsten Flensberg. *Many-Body Quantum Theory in Condensed Matter Physics: An Introduction*. en. Oxford Graduate Texts, Sept. 2004.

[182] Andrea Damascelli. "Probing the Electronic Structure of Complex Systems by ARPES". *Physica Scripta* 2004.T109 (2004), p. 61.

[183] A. Kaminski et al. "Identifying the Background Signal in Angle-Resolved Photoemission Spectra of High-Temperature Cuprate Superconductors". *Phys. Rev. B* 69.21 (June 2004), p. 212509.

[184] C. Cancellieri et al. "Polaronic Metal State at the LaAlO3/SrTiO3 Interface". *Nat Commun* 7 (Jan. 2016), pp. –.

[185] Gerald D. Mahan. *Many-Particle Physics*. en. Boston, MA: Springer US, 2000.

[186] Jorgen Rammer. *Quantum Transport Theory*. en. Westview Press, Sept. 2004.

[187] Alexander L. Fetter and John Dirk Walecka. *Quantum Theory of Many-Particle Systems*. en. Courier Corporation, 2003.

[188] D. A. Shirley. "High-Resolution X-Ray Photoemission Spectrum of the Valence Bands of Gold". *Physical Review B* 5.12 (June 1972), pp. 4709–4714.

[189] V. N. Strocov. "Intrinsic Accuracy in 3-Dimensional Photoemission Band Mapping". *Journal of Electron Spectroscopy and Related Phenomena* 130.1–3 (July 2003), pp. 65–78.

[190] *WebCrossSections; http://ulisse.elettra.trieste.it/services/elements/WebElements.html*. `http://ulisse.elettra.trieste.it/services/elements/WebElements.html`. 2016.

[191] David Attwood. *Soft X-Rays and Extreme Ultraviolet Radiation: Principles and Applications*. en. Cambridge University Press, 2007.

[192] Philipp Willmott. *An Introduction to Synchrotron Radiation: Techniques and Applications*. en. John Wiley & Sons, June 2011.

[193] Eberhard Jaeschke et al. *Synchrotron Light Sources and Free-Electron Lasers: Accelerator Physics, Instrumentation and Science Applications*. en. Springer International Publishing, Apr. 2016.

[194] U. Flechsig, L. Patthey, and T. Schmidt. "Performance Measurements at the SLS Spectroscopy Beamline". *AIP Conf. Proc.* 705 (2004), p. 316.

[195] V. N. Strocov et al. "High-Resolution Soft X-Ray Beamline ADRESS at the Swiss Light Source for Resonant Inelastic X-Ray Scattering and Angle-Resolved Photoelectron Spectroscopies". *Journal of Synchrotron Radiation* 17.Pt 5 (Sept. 2010), pp. 631–643.

[196] V. N. Strocov et al. "Soft-X-Ray ARPES Facility at the ADRESS Beamline of the SLS: Concepts, Technical Realisation and Scientific Applications". eng. *Journal of Synchrotron Radiation* 21.Pt 1 (Jan. 2014), pp. 32–44.

[197] Martin Månsson et al. “On-Board Sample Cleaver”. *Review of Scientific Instruments* 78.7 (July 2007), p. 076103.

[198] Y. Sassa. “ARPES Investigations on in Situ PLD Grown YBa2Cu3O7±\delta”. PhD thesis. Universitee de Neuchatel, 2011.

[199] Akari Takayama. “Development of High Resolution Spin-Resolved Photoemission Spectrometer”. en. *High-Resolution Spin-Resolved Photoemission Spectrometer and the Rashba Effect in Bismuth Thin Films*. Springer Theses. Springer Japan, 2015, pp. 31–55.

[200] Christian Matt. *The Pseudogap Phase in High-Temperature Superconductors - Master Thesis*. July 2012.

[201] N. Mannella et al. “Nodal Quasiparticle in Pseudogapped Colossal Magnetoresistive Manganites”. en. *Nature* 438.7067 (Nov. 2005), pp. 474–478.

[202] S. V. Borisenko et al. “Pseudogap and Charge Density Waves in Two Dimensions”. *Phys. Rev. Lett.* 100.19 (May 2008), p. 196402.

[203] M. Uchida et al. “Pseudogap of Metallic Layered Nickelate $R_{2-x}\mathrm{Sr}_x\mathrm{NiO}_4$ (R = Nd, Eu) Crystals Measured Using Angle-Resolved Photoemission Spectroscopy”. *Phys. Rev. Lett.* 106.2 (Jan. 2011), p. 027001.

[204] Madhavi Chand et al. “Phase Diagram of the Strongly Disordered S-Wave Superconductor NbN close to the Metal-Insulator Transition”. *Phys. Rev. B* 85.1 (2012), p. 014508.

[205] U. Chatterjee et al. “Observation of a D-Wave Nodal Liquid in Highly Underdoped Bi2Sr2CaCu2O8+d”. *Nature Physics* 6 (2010), pp. 99–103.

[206] Jhinhwan Lee et al. “Spectroscopic Fingerprint of Phase-Incoherent Superconductivity in the Underdoped Bi2Sr2CaCu2O8+d”. *Science* 325 (2009), p. 1099.

[207] R. Daou et al. “Linear Temperature Dependence of Resistivity and Change in the Fermi Surface at the Pseudogap Critical Point of a High-Tc Superconductor”. *Nature Physics* 5 (2009), pp. 31–34.

[208] Makoto Hashimoto et al. “Particle-Hole Symmetry Breaking in the Pseudogap State of Bi2201”. en. *Nature Physics* 6.6 (June 2010), pp. 414–418.

[209] Takeshi Kondo et al. “Competition between the Pseudogap and Superconductivity in the High-T(c) Copper Oxides”. eng. *Nature* 457.7227 (Jan. 2009), pp. 296–300.

[210] Takeshi Kondo et al. “Disentangling Cooper-Pair Formation above the Transition Temperature from the Pseudogap State in the Cuprates”. en. *Nature Physics* 7.1 (Jan. 2011), pp. 21–25.

[211] Takeshi Kondo et al. “Formation of Gapless Fermi Arcs and Fingerprints of Order in the Pseudogap State of Cuprate Superconductors”. *Phys. Rev. Lett.* 111.15 (Oct. 2013), p. 157003.

[212] Shinji Kawasaki et al. “Carrier-Concentration Dependence of the Pseudogap Ground State of Superconducting $\mathrm{Bi_2Sr_{2-x}La_xCuO_{6+\delta}}$ Revealed by ^{63,65}Cu-Nuclear Magnetic Resonance in Very High Magnetic Fields”. *Phys. Rev. Lett.* 105.13 (Sept. 2010), p. 137002.

[213] Yang He et al. “Fermi Surface and Pseudogap Evolution in a Cuprate Superconductor”. *Science* 344.6184 (2014), pp. 608–611.

[214] Tao Wu et al. “Magnetic-Field-Induced Charge-Stripe Order in the High-Temperature Superconductor YBa2Cu3Oy”. *Nature (London, United Kingdom)* 477 (2011), p. 191.

[215] Tao Wu et al. “Emergence of Charge Order from the Vortex State of a High-Temperature Superconductor”. *Nat. Comm.* 4 (2013), p. 2113.

[216] A. J. Achkar et al. “Distinct Charge Orders in the Planes and Chains of Ortho-III-Ordered $YBa_2Cu_3\mathbf{O}_{6+\delta}$ Superconductors Identified by Resonant Elastic X-ray Scattering”. *Physical Review Letters* 109.16 (Oct. 2012), p. 167001.

[217] M. Hücker et al. “Competing charge, spin, and superconducting orders in underdoped $YBa_2Cu_3O_y$”. *Phys. Rev. B* 90.5 (Aug. 2014), p. 054514.

[218] S. Blanco-Canosa et al. “Resonant x-ray scattering study of charge-density wave correlations in $YBa_2Cu_3O_{6+x}$”. *Physical Review B* 90.5 (Aug. 2014), p. 054513.

[219] Nicolas Doiron-Leyraud et al. “Hall, Seebeck, and Nernst Coefficients of Underdoped $HgBa_2CuO_{4+\delta}$: Fermi-Surface Reconstruction in an Archetypal Cuprate Superconductor”. *Phys. Rev. X* 3.2 (June 2013), p. 021019.

[220] W. Tabis et al. “Charge Order and Its Connection with Fermi-Liquid Charge Transport in a Pristine High-Tc Cuprate”. en. *Nature Communications* 5 (Dec. 2014), p. 5875.

[221] Eduardo H. da Silva Neto et al. “Ubiquitous Interplay Between Charge Ordering and High-Temperature Superconductivity in Cuprates”. *Science* 343.6169 (2014), pp. 393–396.

[222] R. Comin et al. “Charge Order Driven by Fermi-Arc Instability in $Bi_2Sr_{2-x}La_xCuO_{6+\delta}$”. *Science* 343.6169 (2014), pp. 390–392.

[223] K. Fujita et al. “Simultaneous Transitions in Cuprate Momentum-Space Topology and Electronic Symmetry Breaking”. *Science* 344.6184 (2014), pp. 612–616.

[224] N. B. Christensen et al. “Bulk Charge Stripe Order Competing with Superconductivity in La2-xSrxCuO4 (x=0.12)” (2014), arXiv:1404.3192.

[225] V. Thampy et al. “Rotated stripe order and its competition with superconductivity in $La_{1.88}Sr_{0.12}CuO_4$”. *Phys. Rev. B* 90.10 (Sept. 2014), p. 100510.

[226] T. P. Croft et al. “Charge density wave fluctuations in $La_{2-x}Sr_xCuO_4$ and their competition with superconductivity”. *Phys. Rev. B* 89.22 (June 2014), p. 224513.

[227] N. B. Christensen et al. “Nature of the Magnetic Order in the Charge-Ordered Cuprate $La_{1.48}Nd_{0.4}Sr_{0.12}CuO_4$”. *Physical Review Letters* 98.19 (May 2007), p. 197003.

[228] Olivier Cyr-Choiniére et al. “Zooming on the Quantum Critical Point in Nd-LSCO”. *Physica C: Superconductivity* 470, Supplement 1.0 (2010), S12 –S13.

[229] S. Wakimoto et al. “Effect of a magnetic field on the spin- and charge-density-wave order in $La_{1.45}Nd_{0.4}Sr_{0.15}CuO_4$”. *Phys. Rev. B* 67.18 (May 2003), p. 184419.

[230] Jörg Fink et al. “Phase diagram of charge order in $La_{1.8-x}Eu_{0.2}Sr_xCuO_4$ from resonant soft x-ray diffraction”. *Phys. Rev. B* 83.9 (Mar. 2011), p. 092503.

[231] T. Valla et al. “The Ground State of the Pseudogap in Cuprate Superconductors”. *Science* 314.5807 (2006), pp. 1914–1916.

[232] M. R. Norman et al. “Phenomenology of the low-energy spectral function in high-T_c superconductors”. *Phys. Rev. B* 57.18 (May 1998), R11093–R11096.

[233] M. Shi et al. “Spectroscopic Evidence for Preformed Cooper Pairs in the Pseudogap Phase of Cuprates”. en. *EPL (Europhysics Letters)* 88.2 (2009), p. 27008.

[234] M. Shi et al. “Coherent *d*-Wave Superconducting Gap in Underdoped $La_{2-x}Sr_xCuO_4$ by Angle-Resolved Photoemission Spectroscopy”. *Phys. Rev. Lett.* 101.4 (July 2008), p. 047002.

[235] A. Kanigel et al. “Evolution of the Pseudogap from Fermi Arcs to the Nodal Liquid”. *Nat Phys* 2.7 (July 2006), pp. 447–451.

[236] J. Chang et al. “Electronic Structure near the 1/8-Anomaly in La-Based Cuprates”. *New J. Phys.* 10 (2008), p. 103016.

[237] T. Claesson et al. "Electronic structure of $La_{1.48}Nd_{0.4}Sr_{0.12}CuO_4$ probed by high- and low-energy angle-resolved photoelectron spectroscopy". *Phys. Rev. B* 80.9 (Sept. 2009), p. 094503.

[238] E. Razzoli et al. "The Fermi surface and band folding in La 2- x Sr x CuO 4 , probed by angle-resolved photoemission". *New Journal of Physics* 12.12 (2010), p. 125003.

[239] A. Kaminski et al. "Change of Fermi-surface topology in $Bi_2Sr_2CaCu_2O_{8+\delta}$ with doping". *Physical Review B* 73.17 (May 2006), p. 174511.

[240] S. Benhabib et al. "Collapse of the Normal-State Pseudogap at a Lifshitz Transition in the $Bi_2Sr_2CaCu_2O_{8+\delta}$ Cuprate Superconductor". *Physical Review Letters* 114.14 (Apr. 2015), p. 147001.

[241] Makoto Hashimoto et al. "Energy Gaps in High-Transition-Temperature Cuprate Superconductors". *Nature Physics* 10 (2014), pp. 483–495.

[242] Utpal Chatterjee et al. "Electronic Phase Diagram of High-Temperature Copper Oxide Superconductors". en. *Proceedings of the National Academy of Sciences* 108.23 (July 2011), pp. 9346–9349.

[243] Kiyohisa Tanaka et al. "Distinct Fermi-Momentum-Dependent Energy Gaps in Deeply Underdoped Bi2212". *Science* 314.5807 (2006), pp. 1910–1913.

[244] J. Chang et al. "Anisotropic quasiparticle scattering rates in slightly underdoped to optimally doped high-temperature $La_{2-x}Sr_xCuO_4$ superconductors". *Physical Review B* 78.20 (Nov. 2008), p. 205103.

[245] J. Chang et al. "Magnetic-Field-Induced Spin Excitations and Renormalized Spin Gap of the Underdoped $La_{1.895}Sr_{0.105}CuO_4$ Superconductor". *Physical Review Letters* 98.7 (Feb. 2007), p. 077004.

[246] J. Chang et al. "Tuning competing orders in $La_{2-x}Sr_xCuO_4$ cuprate superconductors by the application of an external magnetic field". *Physical Review B* 78.10 (Sept. 2008), p. 104525.

[247] J. Chang et al. "Spin density wave induced disordering of the vortex lattice in superconducting $La_{2-x}Sr_xCuO_4$". *Physical Review B* 85.13 (Apr. 2012), p. 134520.

[248] A. V. Chubukov et al. "Gapless Pairing and the Fermi Arc in the Cuprates". *Phys. Rev. B* 76.18 (Nov. 2007), p. 180501.

[249] M. Franz and A. J. Millis. "Phase Fluctuations and Spectral Properties of Underdoped Cuprates". *Phys. Rev. B* 58.21 (Dec. 1998), pp. 14572–14580.

[250] G.-H. Gweon, B. S. Shastry, and G. D. Gu. "Extremely Correlated Fermi-Liquid Description of Normal-State ARPES in Cuprates". *Phys. Rev. Lett.* 107.5 (July 2011), p. 056404.

[251] C. G. Fatuzzo et al. "Nodal Landau Fermi-liquid quasiparticles in overdoped $La_1.77Sr_0.23CuO_4$". *Phys. Rev. B* 89.20 (May 2014), p. 205104.

[252] T. Valla et al. "Temperature Dependent Scattering Rates at the Fermi Surface of Optimally Doped $Bi_2Sr_2CaCu_2O_{8+\delta}$". *Phys. Rev. Lett.* 85.4 (July 2000), pp. 828–831.

[253] J. Chang et al. "Anisotropic breakdown of Fermi liquid quasiparticle excitations in overdoped $La_{2x}Sr_xCuO_4$". en. *Nature Communications* 4 (Oct. 2013), p. 2559.

[254] J. W. Alldredge et al. "Evolution of the electronic excitation spectrum with strongly diminishing hole density in superconducting Bi2Sr2CaCu2O8+[delta]". *Nat Phys* 4 (2008), pp. 319–326.

[255] Takuya Kato et al. "Doping Dependence of Two Energy Scales in the Tunneling Spectra of Superconducting La2-xSrxCuO4". *Journal of the Physical Society of Japan* 77.5 (2008), p. 054710.

[256] A. Kaminski et al. “Momentum Anisotropy of the Scattering Rate in Cuprate Superconductors”. *Phys. Rev. B* 71.1 (Jan. 2005), p. 014517.

[257] David Sénéchal and A.-M. S. Tremblay. “Hot Spots and Pseudogaps for Hole- and Electron-Doped High-Temperature Superconductors”. *Phys. Rev. Lett.* 92.12 (Mar. 2004), p. 126401.

[258] Emanuel Gull, Olivier Parcollet, and Andrew J. Millis. “Superconductivity and the Pseudogap in the Two-Dimensional Hubbard Model”. *Phys. Rev. Lett.* 110.21 (May 2013), p. 216405.

[259] G. Sordi et al. “*c*-axis resistivity, pseudogap, superconductivity, and Widom line in doped Mott insulators”. *Phys. Rev. B* 87.4 (Jan. 2013), p. 041101.

[260] M. Ferrero et al. “Valence Bond Dynamical Mean-Field Theory of Doped Mott Insulators with Nodal/Antinodal Differentiation”. *EPL (Europhysics Letters)* 85.5 (2009), p. 57009.

[261] H. Alloul. “What Is the Simplest Model That Captures the Basic Experimental Facts of the Physics of Underdoped Cuprates?” *C. R. Phys.* 15.6 (2014), p. 519.

[262] Patrick A. Lee. “Amperean Pairing and the Pseudogap Phase of Cuprate Superconductors”. *Phys. Rev. X* 4.3 (July 2014), p. 031017.

[263] I. M. Vishik et al. “Phase Competition in Trisected Superconducting Dome”. *Proc. of the National Academy of Sciences* 109.45 (2012), pp. 18332–18337.

[264] Eun Gook Moon and Subir Sachdev. “Quantum Critical Point Shifts under Superconductivity: Pnictides and Cuprates”. *Phys. Rev. B* 82.10 (Sept. 2010), p. 104516.

[265] Makoto Hashimoto et al. “Direct spectroscopic evidence for phase competition between the pseudogap and superconductivity in $Bi_2Sr_2CaCu_2O_{8+\delta}$”. *Nat. Mat.* 14.1 (Jan. 2015), pp. 37–42.

[266] C. Monney et al. “Electron-hole fluctuation phase in 1*T*-$TiSe_2$”. *Phys. Rev. B* 85.23 (2012), p. 235150.

[267] D. S. Inosov et al. “Temperature-dependent Fermi surface of $2H\text{-}TaSe_2$ driven by competing density wave order fluctuations”. *Phys. Rev. B* 79.12 (2009), p. 125112.

[268] T. Kiss et al. “Charge-Order-Maximized Momentum-Dependent Superconductivity”. *Nat. Phys.* 3 (2007), pp. 720–725.

[269] U. Chatterjee et al. “Emergence of Coherence in the Charge-Density Wave State of 2H-NbSe2”. en. *Nature Communications* 6 (Feb. 2015), p. 6313.

[270] Matthias Vojta. “Lattice Symmetry Breaking in Cuprate Superconductors: Stripes, Nematics, and Superconductivity”. *Advances in Physics* 58.6 (2009), pp. 699–820.

[271] J. Chang et al. “Nernst and Seebeck Coefficients of the Cuprate Superconductor $YBa_2Cu_3\mathbf{O}_{6.67}$: A Study of Fermi Surface Reconstruction”. *Physical Review Letters* 104.5 (Feb. 2010), p. 057005.

[272] Q. Li et al. “Two-Dimensional Superconducting Fluctuations in Stripe-Ordered $La_{1.875}Ba_{0.125}CuO_4$”. *Phys. Rev. Lett.* 99.6 (Aug. 2007), p. 067001.

[273] S. B. Wilkins et al. “Comparison of stripe modulations in $La_1.875Ba_0.125CuO_4$ and $La_1.48Nd_0.4Sr_0.12CuO_4$”. *Phys. Rev. B* 84.19 (Nov. 2011), p. 195101.

[274] B. Nachumi et al. “Muon spin relaxation study of the stripe phase order in $La_{1.6-x}Nd_{0.4}Sr_xCuO_4$ and related 214 cuprates”. *Phys. Rev. B* 58.13 (Oct. 1998), pp. 8760–8772.

[275] J. M. Tranquada et al. “Neutron-scattering study of stripe-phase order of holes and spins in $La_{1.48}Nd_{0.4}Sr_{0.12}CuO_4$”. *Phys. Rev. B* 54.10 (Sept. 1996), pp. 7489–7499.

[276] M. Fujita et al. “Stripe order, depinning, and fluctuations in $La_{1.875}Ba_{0.125}CuO_4$ and $La_{1.875}Ba_{0.075}Sr_{0.050}CuO_4$”. *Phys. Rev. B* 70.10 (Sept. 2004), p. 104517.

[277] Rui-Hua He et al. "Energy Gaps in the Failed High-Tc Superconductor La1.875Ba0.125CuO4". *Nature Physics* 5 (2009), pp. 119–123.

[278] V. B. Zabolotnyy et al. "Evidence for Fermi Surface Reconstruction in the Static Stripe Phase of La 1.8-X Eu 0.2 Sr X CuO 4 , x=1/8". *EPL (Europhysics Letters)* 86.4 (2009), p. 47005.

[279] Tonica Valla. "Angle-Resolved Photoemission from Cuprates with Static Stripes". *Physica C: Superconductivity* 481.0 (2012), pp. 66 –74.

[280] Takeshi Kondo et al. "Evidence for Two Energy Scales in the Superconducting State of Optimally Doped $(Bi,Pb)_2(Sr,La)_2CuO_{6+\delta}$". *Phys. Rev. Lett.* 98.26 (June 2007), p. 267004.

[281] S. Hüfner et al. "Two Gaps Make a High-Temperature Superconductor?" en. *Reports on Progress in Physics* 71.6 (2008), p. 062501.

[282] J.-H. Ma et al. "Coexistence of Competing Orders with Two Energy Gaps in Real and Momentum Space in the High Temperature Superconductor $Bi_2Sr_{2-x}La_xCuO_{6+\delta}$". *Phys. Rev. Lett.* 101.20 (Nov. 2008), p. 207002.

[283] G. Grüner. "The Dynamics of Charge-Density Waves". *Rev. Mod. Phys.* 60.4 (Oct. 1988), pp. 1129–1181.

[284] Nicolas Doiron-Leyraud et al. "Quantum Oscillations and the Fermi Surface in an Underdoped High-Tc Superconductor". *Nature* 447.7144 (May 2007), pp. 565–568.

[285] Suchitra E. Sebastian, Neil Harrison, and Gilbert G. Lonzarich. "Towards Resolution of the Fermi Surface in Underdoped High- T c Superconductors". *Reports on Progress in Physics* 75.10 (2012), p. 102501.

[286] B. Vignolle et al. "Quantum Oscillations and Fermi Surface of High Temperature Cuprate Superconductors". *Comptes Rendus de Physique* 12 (2011), pp. 446 –460.

[287] Neven Barišić et al. "Universal Quantum Oscillations in the Underdoped Cuprate Superconductors". *Nat. Phys.* 9 (2013), pp. 761–764.

[288] F. Lalibert/'e et al. "Fermi-Surface Reconstruction by Stripe Order in Cuprate Superconductors". *Nat Commun* 2 (Aug. 2011), pp. 432–.

[289] David LeBoeuf et al. "Lifshitz critical point in the cuprate superconductor $YBa_2Cu_3O_y$ from high-field Hall effect measurements". *Phys. Rev. B* 83.5 (Feb. 2011), p. 054506.

[290] R.-H. He et al. "Doping Dependence of the (Π, π) Shadow Band in La-Based Cuprates Studied by Angle-Resolved Photoemission Spectroscopy". *New Journal of Physics* 13.1 (2011), p. 013031.

[291] Jianqiao Meng et al. "Coexistence of Fermi Arcs and Fermi Pockets in a High-Tc Copper Oxide Superconductor". *Nature* 462.7271 (Nov. 2009), pp. 335–338.

[292] P. D. C. King et al. "Structural Origin of Apparent Fermi Surface Pockets in Angle-Resolved Photoemission of $Bi_2Sr_{2-x}La_xCuO_{6+\delta}$". *Phys. Rev. Lett.* 106.12 (Mar. 2011), p. 127005.

[293] M. Fujita et al. "Static magnetic correlations near the insulating-superconducting phase boundary in $La_{2-x}Sr_xCuO_4$". *Phys. Rev. B* 65.6 (Jan. 2002), p. 064505.

[294] S. Wakimoto et al. "Systematic study of short-range antiferromagnetic order and the spin-glass state in lightly doped $La_{2-x}Sr_xCuO_4$". *Phys. Rev. B* 62.5 (Aug. 2000), pp. 3547–3553.

[295] N. Xu et al. "Electronic Band Structure of $BaCo_2As_2$: A Fully Doped Ferropnictide Analog with Reduced Electronic Correlations". *Physical Review X* 3.1 (Jan. 2013), p. 011006.

[296] N. Xu et al. "Possible nodal superconducting gap and Lifshitz transition in heavily hole-doped $Ba_{0.1}K_{0.9}Fe_2As_2$". *Physical Review B* 88.22 (Dec. 2013), p. 220508.

[297] Delong Fang et al. “Observation of a Van Hove singularity and implication for strong-coupling induced Cooper pairing in KFe_2As_2”. *Physical Review B* 92.14 (Oct. 2015), p. 144513.

[298] Koichi Momma and Fujio Izumi. “VESTA 3 for Three-Dimensional Visualization of Crystal, Volumetric and Morphology Data”. en. *Journal of Applied Crystallography* 44.6 (Dec. 2011), pp. 1272–1276.

[299] Yu Song et al. “A Mott Insulator Induced near Iron Pnictide Superconductors”. *arXiv:1504.05116* (2015).

[300] A. F. Wang et al. “Phase diagram and physical properties of $NaFe_{1-x}Cu_xAs$ single crystals”. *Physical Review B* 88.9 (Sept. 2013), p. 094516.

[301] John P. Perdew, Kieron Burke, and Matthias Ernzerhof. “Generalized Gradient Approximation Made Simple”. *Physical Review Letters* 77.18 (Oct. 1996), pp. 3865–3868.

[302] V. I. Anisimov et al. “Density-Functional Theory and NiO Photoemission Spectra”. *Physical Review B* 48.23 (Dec. 1993), pp. 16929–16934.

[303] A. I. Liechtenstein, V. I. Anisimov, and J. Zaanen. “Density-Functional Theory and Strong Interactions: Orbital Ordering in Mott-Hubbard Insulators”. *Physical Review B* 52.8 (Aug. 1995), R5467–R5470.

[304] M. A. Tanatar et al. “Evolution of normal and superconducting properties of single crystals of $Na_{1-\delta}FeAs$ upon interaction with environment”. *Physical Review B* 85.1 (Jan. 2012), p. 014510.

[305] S. F. Wu et al. “Direct spectroscopic evidence for completely filled Cu $3d$ shell in $BaCu_2As_2$ and $\alpha - BaCu_2Sb_2$”. *Physical Review B* 91.23 (June 2015), p. 235109.

[306] D. J. Singh. “Electronic structure of $BaCu_2As_2$ and $SrCu_2As_2$: sp-band metals”. *Physical Review B* 79.15 (Apr. 2009), p. 153102.

[307] Cun Ye et al. “Strong Similarities between the Local Electronic Structure of Insulating Iron Pnictide and Lightly Doped Cuprate”. *Phys. Rev. X* 5.2 (Apr. 2015), p. 021013.

[308] N. Xu et al. “Angle-resolved photoemission observation of isotropic superconducting gaps in isovalent Ru-substituted $Ba(Fe_{0.75}Ru_{0.25})_2As_2$”. *Physical Review B* 87.9 (Mar. 2013), p. 094513.

[309] Ambroise van Roekeghem et al. “Spectral Properties of Transition Metal Pnictides and Chalcogenides: Angle-Resolved Photoemission Spectroscopy and Dynamical Mean-Field Theory”. *Comptes Rendus Physique* 17 (2016), pp. 140–163.

[310] R. S. Dhaka et al. “Tuning the metal-insulator transition in $NdNiO_3$ heterostructures via Fermi surface instability and spin fluctuations”. *Phys. Rev. B* 92.3 (July 2015), p. 035127.

[311] Adam Kaminski and Helen M. Fretwell. “On the Extraction of the Self-Energy from Angle-Resolved Photoemission Spectroscopy”. *New Journal of Physics* 7.1 (2005), p. 98.

[312] Philip W. Anderson. “Theory of Magnetic Exchange Interactions:Exchange in Insulators and Semiconductors”. *Solid State Physics*. Ed. by Frederick Seitz Turnbull and David. Vol. 14. Academic Press, 1963, pp. 99–214.

[313] P. W. Anderson. “Local Moments and Localized States”. *Reviews of Modern Physics* 50.2 (Apr. 1978), pp. 191–201.

[314] S. Nakatsuji et al. “Heavy-Mass Fermi Liquid near a Ferromagnetic Instability in Layered Ruthenates”. *Physical Review Letters* 90.13 (Apr. 2003), p. 137202.

[315] Yogesh Singh and P. Gegenwart. “Antiferromagnetic Mott insulating state in single crystals of the honeycomb lattice material Na_2IrO_3”. *Physical Review B* 82.6 (Aug. 2010), p. 064412.

[316] J. E. Keem, J. M. Honig, and L. L. Van Zandt. "Localized Charge Carrier Transport in Pure Single Crystals of NiO". *Philosophical Magazine Part B* 37.4 (Apr. 1978), pp. 537–543.

[317] Shin-Ichi Uchida. "Recent Progress in High- T c Superconductor Research: Unique and Novel Metallic State in Doped CuO 2 Plane". *Japanese Journal of Applied Physics* 32.9R (1993), p. 3784.

[318] M. Yi et al. "Observation of Temperature-Induced Crossover to an Orbital-Selective Mott Phase in $A_xFe_{2-y}Se_2$ (A=K, Rb) Superconductors". *Physical Review Letters* 110.6 (Feb. 2013), p. 067003.

[319] S. T. Cui et al. "ARPES Study of the Effect of Cu Substitution on the Electronic Structure of NaFeAs". *Phys. Rev. B* 88.24 (Dec. 2013), p. 245112.

[320] T. Yoshida et al. "Low-energy electronic structure of the high- T c cuprates $La_{2x}Sr_xCuO_4$ studied by angle-resolved photoemission spectroscopy". *Journal of Physics: Condensed Matter* 19.12 (2007), p. 125209.

[321] C.E. Matt et al. "$NaFe_{0.56}Cu_{0.44}As$: A Pnictide Insulating Phase Induced by On-Site Coulomb Interaction". *Physical Review Letters* 117.9 (Aug. 2016), p. 097001.

[322] Luca de' Medici. "Hund's Coupling and Its Key Role in Tuning Multiorbital Correlations". *Physical Review B* 83.20 (May 2011), p. 205112.

[323] J. E. Han, M. Jarrell, and D. L. Cox. "Multiorbital Hubbard Model in Infinite Dimensions: Quantum Monte Carlo Calculation". *Physical Review B* 58.8 (Aug. 1998), R4199–R4202.

[324] E. Razzoli et al. "Tuning Electronic Correlations in Transition Metal Pnictides: Chemistry beyond the Valence Count". *Physical Review B* 91.21 (June 2015), p. 214502.

[325] A. Charnukha et al. "High-Temperature Superconductivity from Fine-Tuning of Fermi-Surface Singularities in Iron Oxypnictides". en. *Scientific Reports* 5 (Dec. 2015), p. 18273.

[326] A. Charnukha et al. "Interaction-Induced Singular Fermi Surface in a High-Temperature Oxypnictide Superconductor". en. *Scientific Reports* 5 (May 2015), p. 10392.

[327] A. I. Coldea et al. "Fermi Surface of Superconducting LaFePO Determined from Quantum Oscillations". *Physical Review Letters* 101.21 (Nov. 2008), p. 216402.

[328] L. Ortenzi et al. "Fermi-Surface Shrinking and Interband Coupling in Iron-Based Pnictides". *Physical Review Letters* 103.4 (July 2009), p. 046404.

[329] M. Yi et al. "Electronic structure of the $BaFe_2As_2$ family of iron-pnictide superconductors". *Physical Review B* 80.2 (July 2009), p. 024515.

[330] Z.R. Ye et al. "Extraordinary Doping Effects on Quasiparticle Scattering and Bandwidth in Iron-Based Superconductors". *Physical Review X* 4.3 (Sept. 2014), p. 031041.

[331] F. Hardy et al. "Evidence of Strong Correlations and Coherence-Incoherence Crossover in the Iron Pnictide Superconductor KFe_2As_2". *Physical Review Letters* 111.2 (July 2013), p. 027002.

[332] A. S. Sefat et al. "Renormalized behavior and proximity of $BaCo_2As_2$ to a magnetic quantum critical point". *Physical Review B* 79.2 (Jan. 2009), p. 024512.

[333] T. Qian et al. "Quasinested Fe orbitals versus Mott-insulating V orbitals in superconducting $\mathbf{Sr_2VFeAsO_3}$ as seen from angle-resolved photoemission". *Physical Review B* 83.14 (Apr. 2011), p. 140513.

[334] H. Zenia et al. "Appearance of "Fragile" Fermi Liquids in Finite-Width Mott Insulators Sandwiched between Metallic Leads". *Physical Review Letters* 103.11 (Sept. 2009), p. 116402.

[335] J. H. Shim, K. Haule, and G. Kotliar. "Density-functional calculations of the electronic structures and magnetism of the pnictide superconductors $BaFeAs_2$ and $BaFeSb_2$". *Physical Review B* 79.6 (Feb. 2009), p. 060501.

[336] Naoyuki Katayama et al. "Superconductivity in $Ca_{1-x}La_xFeAs_2$: A Novel 112-Type Iron Pnictide with Arsenic Zigzag Bonds". *Journal of the Physical Society of Japan* 82.12 (Nov. 2013), p. 123702.

[337] Hiroyuki Yakita et al. "A New Layered Iron Arsenide Superconductor: (Ca,Pr)$FeAs_2$". *Journal of the American Chemical Society* 136.3 (Jan. 2014), pp. 846–849.

[338] M. Y. Li et al. "Significant contribution of As $4p$ orbitals to the low-lying electronic structure of the 112-type iron-based superconductor $Ca_{0.9}La_{0.1}FeAs_2$". *Physical Review B* 91.4 (Jan. 2015), p. 045112.

[339] Shan Jiang et al. "Structural and magnetic phase transitions in $Ca_{0.73}La_{0.27}FeAs_2$ with electron-overdoped FeAs layers". *Physical Review B* 93.5 (Feb. 2016), p. 054522.

[340] Kazutaka Kudo et al. "Superconducting Transition Temperatures of up to 47 K from Simultaneous Rare-Earth Element and Antimony Doping of 112-Type CaFeAs2". *Journal of the Physical Society of Japan* 83.9 (Aug. 2014), p. 093705.

[341] S. R. Saha et al. "Structural collapse and superconductivity in rare-earth-doped $CaFe_2As_2$". *Physical Review B* 85.2 (Jan. 2012), p. 024525.

[342] Xianxin Wu et al. "$CaFeAs_2$: A staggered intercalation of quantum spin Hall and high-temperature superconductivity". *Physical Review B* 91.8 (Feb. 2015), p. 081111.

[343] Y. Zhang et al. "Orbital characters of bands in the iron-based superconductor $BaFe_{1.85}Co_{0.15}As_2$". *Physical Review B* 83.5 (Feb. 2011), p. 054510.

[344] S. de Jong et al. "High-resolution, hard x-ray photoemission investigation of $BaFe_2As_2$: Moderate influence of the surface and evidence for a low degree of Fe $3d$ – As $4p$ hybridization of electronic states near the Fermi energy". *Physical Review B* 79.11 (Mar. 2009), p. 115125.

[345] Xianxin Wu et al. "Effect of As-chain layers in $CaFeAs_2$". *Physical Review B* 89.20 (May 2014), p. 205102.

[346] Guangtao Wang et al. "The electronic structure and magnetism of $CaFeAs_2$: First principles calculations". *Solid State Communications* 200 (Dec. 2014), pp. 61–65.

[347] P. Zhang et al. "A Precise Method for Visualizing Dispersive Features in Image Plots". *Review of Scientific Instruments* 82.4 (2011).

[348] Véronique Brouet et al. "ARPES View of Orbitally Resolved Quasiparticle Lifetimes in Iron Pnictides". *Phys. Rev. B* 93.8 (Feb. 2016), p. 085137.

[349] J. Maletz et al. "Unusual Band Renormalization in the Simplest Iron-Based Superconductor $\textFeSe_1\ensuremath-X$". *Phys. Rev. B* 89.22 (June 2014), p. 220506.

[350] Kazuhiko Kuroki et al. "Unconventional Pairing Originating from the Disconnected Fermi Surfaces of Superconducting $LaFeAsO_{1-x}F_x$". *Physical Review Letters* 101.8 (Aug. 2008), p. 087004.

[351] Valentin Stanev, Jian Kang, and Zlatko Tesanovic. "Spin Fluctuation Dynamics and Multiband Superconductivity in Iron Pnictides". *Physical Review B* 78.18 (Nov. 2008), p. 184509.

[352] Fa Wang et al. "Functional Renormalization-Group Study of the Pairing Symmetry and Pairing Mechanism of the FeAs-Based High-Temperature Superconductor". *Physical Review Letters* 102.4 (Jan. 2009), p. 047005.

[353] T. Qian et al. "Absence of a Holelike Fermi Surface for the Iron-Based $K_{0.8}Fe_{1.7}Se_2$ Superconductor Revealed by Angle-Resolved Photoemission Spectroscopy". *Physical Review Letters* 106.18 (May 2011), p. 187001.

[354] Defa Liu et al. "Electronic Origin of High-Temperature Superconductivity in Single-Layer FeSe Superconductor". en. *Nature Communications* 3 (July 2012), p. 931.

[355] Jian-Feng Ge et al. "Superconductivity above 100 K in Single-Layer FeSe Films on Doped SrTiO3". en. *Nature Materials* 14.3 (Mar. 2015), pp. 285–289.

[356] Shaolong He et al. "Phase Diagram and Electronic Indication of High-Temperature Superconductivity at 65 K in Single-Layer FeSe Films". en. *Nature Materials* 12.7 (July 2013), pp. 605–610.

[357] Shiyong Tan et al. "Interface-Induced Superconductivity and Strain-Dependent Spin Density Waves in FeSe/SrTiO3 Thin Films". en. *Nature Materials* 12.7 (July 2013), pp. 634–640.

[358] Lin Zhao et al. "Common Electronic Origin of Superconductivity in (Li,Fe)OHFeSe Bulk Superconductor and Single-Layer FeSe/SrTiO3 Films". en. *Nature Communications* 7 (Feb. 2016), p. 10608.

[359] X. H. Niu et al. "Surface electronic structure and isotropic superconducting gap in $(Li_{0.8}Fe_{0.2})$OHFeSe". *Physical Review B* 92.6 (Aug. 2015), p. 060504.

[360] M. Fujioka et al. "Phase Diagram and Superconductivity at 58.1 K in α-FeAs-Free SmFeAsO 1- X F X". en. *Superconductor Science and Technology* 26.8 (2013), p. 085023.

[361] P. Zhang et al. "Disentangling the Surface and Bulk Electronic Structures of LaOFeAs". *arXiv:1606.01033 [cond-mat]* (June 2016). arXiv: `1606.01033 [cond-mat]`.

[362] Chang Liu et al. "Surface-Driven Electronic Structure in LaFeAsO Studied by Angle-Resolved Photoemission Spectroscopy". *Physical Review B* 82.7 (Aug. 2010), p. 075135.

[363] Haiyun Liu et al. "Unusual Electronic Structure and Observation of Dispersion Kink in CeFeAsO Parent Compound of FeAs-Based Superconductors". *Physical Review Letters* 105.2 (July 2010), p. 027001.

[364] Helmut Eschrig, Alexander Lankau, and Klaus Koepernik. "Calculated Cleavage Behavior and Surface States of LaOFeAs". *Physical Review B* 81.15 (Apr. 2010), p. 155447.

[365] S. Katrych et al. "$Pr_4Fe_2As_2Te_{1-x}O_4$: A layered FeAs-based superconductor". *Physical Review B* 87.18 (May 2013), p. 180508.

[366] S. Katrych et al. "$L_4Fe_2As_2Te_{1-x}O_{4-y}F_y (L$ = Pr, Sm, Gd) : A layered oxypnictide superconductor with T_c up to 45 K". *Physical Review B* 89.2 (Jan. 2014), p. 024518.

[367] F. Massee et al. "Cleavage surfaces of the $BaFe_{2-x}Co_xAs_2$ and $Fe_ySe_{1-x}Te_x$ superconductors: A combined STM plus LEED study". *Physical Review B* 80.14 (Oct. 2009), p. 140507.

[368] M. Cordin et al. "Comment on "Cleavage surface of the $BaFe_{2-x}Co_xAs_2$ and $Fe_ySe_{1-x}Te_x$ superconductors: A combined STM plus LEED study"". *Physical Review B* 86.16 (Oct. 2012), p. 167401.

[369] J. J. Lee et al. "Interfacial Mode Coupling as the Origin of the Enhancement of Tc in FeSe Films on SrTiO3". en. *Nature* 515.7526 (Nov. 2014), pp. 245–248.

[370] Elbio Dagotto. "*Colloquium* : The Unexpected Properties of Alkali Metal Iron Selenide Superconductors". *Rev. Mod. Phys.* 85.2 (May 2013), pp. 849–867.

[371] Louis Taillefer. *"Superconductivity: The Magic and the Mystery" Aspen Center for Physics : The 2014 Nick and Maggie DeWolf Lecture Series, Aspen.* `http://vod.grassrootstv.org/cablecast/public/Show.aspx?ChannelID=1\&ShowID=12200`.

Acknowledgments

During the past four years, I have met a multitude of persons who have not hesitated to provide support and help with my PhD project and teach me in all aspects of life. First of all, I would like to thank my supervisors Joël Mesot and Ming Shi who gave me the unique opportunity to work on this PhD project. They have been a never-dwindling source of new ideas, suggestions and comments and in any situation their doors have been open for enlightening discussions. As well, I would like to thank Philipp Aebi for being the co-examiner of my thesis and Manfred Sigrist for being the chair during the examination.
Special thanks also goes to Nan Xu who has been there during all the four years. Together, we have spend "infinite" hours (day and night) of beamtime, sample preparation, Chinese movies, etc. He taught me what it means to squeeze out the last bit of information from a sample and "produce" groundbreaking results within one night. He is/was the most productive person I have ever met.
Besides Nan, I would like to thank Xun Shi, Junzhang Ma, Baiqing Lv and Binbin Fu. You where always available, no matter how many days and weeks of beamtime you had in a row. Working together with you was always a new experience, since all of you taught me many pieces of the rich Chinese culture!
I would also like to thank Elia who introduced me to all the experimental and theoretical tools and software which are used for data analysis and DFT calculations. Especially in the beginning of my PhD, you have been a great support and taught me all the scientific and less-scientific parts in the life of a PhD student.
I will never forget the experimental and technical discussions with Nick, and the many hours we spend together on the bike (may you become the future Strava-KOM!). Thanks for sharing all your scientific expertise, language skills and funny moments.
From the first day that I joined the research group I have been amazed by the broad scientific, political and historical knowledge of Milan. Thank you for sharing your knowledge with me and may you eventually find the "perfect" car! Besides this, of course I would like to thank every (former) member of the Spectroscopy of Novel Materials Group: Vlad, Luc, Zhiming, Tian, Raj, Zoran, Hugo, Stefan, Mauro, Andrew, Gabriel, Federico, Adrian, Daniel, Johny, Marcus, Xingye, Yaobo, Valentina, Claude and Martina. The atmosphere was always friendly, helpful and full of energy not least because of our group leader Thorsten who was always encouraging and open for new ideas. Special thanks also goes to the technicians Fritz, Christoph, Leonard, Andreas and Markus, who kept the machine running and were always on the spot when there was need for another joke or an "off-topic" discussion.
I am very thankful to Johan Chang, who introduced me to the field of high-temperature superconductivity in my Master project and who kept my interest in Cuprates at a high level throughout the whole PhD period. Yasmine Sassa, who taught me the sample preparation procedure and experimental operation was always of big help. Together with Martin Månsson, Claudia, Sarah, Dennys, Daniel and Valerio we spent many beamtimes on Cuprates, had nice and long discussions and all varieties of healthy and less-healthy snacks and candies.
All the ARPES experiments were only possible because high quality crystals have been provided by our collaborating sample growers. Therefore, I would like to thank all the sample

growers for their great effort and support: J.B. Goodenough, J.-S. Zhou, M. Oda, M. Ido, T. Kurosowa, J.-Q. Yan, Yu Song, P.C. Dai, Chongde Chao, G.F. Chen and Sergiy Katrych.

Additionally, I would like to thank the PSI-Tennis team, especially Daniel Grolimund, Haimo Jöhri, Daniel M. and our coach Pawel for the nice and amusing training sessions which certainly have been leading to new ideas and have always been a source of energy.
I am very obliged to my family and friends for the continuous personal and mental support. The countless days and nights which I spent at the experiment and not with them have always been treated with great tolerance and acceptance. From the bottom of my heart I would like to thank Nadine. She has proofread this thesis, met my continuous physical and mental absences with great respect and tolerance and encouraged me in every situation. Nadine, I cannot thank you enough for that. VIELEN DANK AN ALLE!

Zurich, 2016-08-12

Curriculum Vitae

Christian Egon Matt

born: 23.09.1987

Address:	Altstetterstrasse 146, 8048 Zurich, Switzerland
Phone:	+41 77 437 4785
	+49 172 6364344
Email:	christian_matt@gmx.de
Nationality:	German

Education

Swiss Federal Institute of Technology Zurich (ETH), Zürich, CH (Sep. 2012 - present)
Paul Scherrer Institute, Villigen, CH (Sep. 2012 - present)

- PhD candidate at Paul Scherrer Institute and ETH Zurich
- Advisors: Prof. Dr. Joel Mesot, Prof. Dr. Ming Shi

Swiss Federal Institute of Technology Zurich (ETH), Zürich, CH (Sep. 2007 - Sep. 2012)

- Bachelor of Science ETH in Physics, May 2012
- Master of Science ETH in Physics, September 2012
- Advisors: Prof. Dr. Joel Mesot, Dr. Johan Chang
- Thesis Title*: The pseudogap phase in high-temperature superconductors - An angle resolved photoemission spectroscopy study*

Technical secondary school, Waldshut, GER (Sep. 2004 - July 2007)

- Technical diploma (high-school degree); discipline information technology, July 2007
  (Abitur an Technischem Gymnasium, Fachrichtung Informationstechnik).

Research experience

PhD project (Research Assistant of Prof. Dr. Ming Shi and Prof. Dr. Joel Mesot)

- Performed ultraviolet and and soft X-ray angle-resolved photoemission spectroscopy (ARPES) on copper and iron-based high temperature superconductors, semiconductors, topological insulators and PLD-grown oxide films.
  Performed density functional theory (DFT) calculations for iron-based superconductors and Semiconductors with Wien2K.
- Research topics: Strong correlations; Quantum phase transitions; phase competition between charge density wave phase, pseudogap and superconducting phase in La-based cuprate superconductors; metal to insulator transition in nickelates and iron pnictide superconductors; electronic bandstructure in high temperature superconductors; topological properties of iron-based superconductors.
- Research techniques: High Resolution Angle resolved Photoemission Spectroscopy (ARPES) in UV and SX regime, Laue backscattering technique, Low energy electron diffraction (LEED), *ab-initio* density functional theory calculations (Wien2k), Matlab, Wavemetrics IgorPRO, Magnetic and physical properties measurement system (MPMS, PPMS).

Master project: (Research Assistant of Dr. Johan Chang and Prof. Dr. Joel Mesot)

- Investigation of the pseudogap phase in high temperature cuprate superconductors by means of synchrotron based angle-resolved photoemission spectroscopy (ARPES). The special focus was set to the relation between the pseudogap and the superconducting phase in $La_{1.6-x}Sr_xNd_{0.4}CuO_4$.

Awards & Achievements

- Third Place at German regional science youth competition Jugend forscht – Regionalwettbewerb (Technical Sciences) 2007
- Winner of the Physics-Award in high-school, 2007

Additional Qualifications

Languages:

- German (mother tongue)
- English (fluent)
- French (high school level)

Sofware:

- Office 2010, LaTex
- Wien2k density functional theory based compouter code for calculation of DOS and Bandstructure
- Mahematical Software (Matlab, Mathematica, Wavemetrics Igor)
- Java, C/C++, HTML, PHP, Linux (all basic knowledge)

Business courses:

- Discovering Management: Accounting for Managers (ETH Zürich 2014)
- Psychological Aspects of Risk Management and Technology (ETH Zürich 2015)
- Decision Theory: Rationality, Risk and Human Decision Making(ETH Zürich 2013)

Talks at conferences/workshops

1. *The effect of As-chain layers on the electronic structure in '112' iron-pnictides – a high-resolution ARPES study*
   Joint Annual Meeting of ÖPG, SPG, ÖGAA und SGAA, September 1 - 4, 2015, Vienna, AUS

2. *Camelback-shaped band reconciles heavy electron behavior with weak electronic Coulomb correlations in superconducting $TlNi_2Se_2$*
   The International Conference M2S HTSC, August 23 - 28, 2015, Geneva, CH

3. *Disentanglement of pseudogap and charge stripe order in Nd-LSCO*
   SPS meeting, June 30 - July 2, 2014, Fribourg, CH

4. *Electron–electron correlation in 122 pnctides, revealed by SX-ARPES*
   PSI – IOP Joint Workshop, October 16 - 17, 2013, Beijing, CN

Posters at conferences/workshops

1. *The effect of As-chain layers on the electronic structure in '112' iron-pnictides – a high-resolution ARPES study;*
   Gordon Research Conference & Gordon Research Seminar: Unconventional Superconductivity: Materials and Mechanism, Chinese University of Hong Kong, May 23 - 29, 2015, Hong Kong, CN

2. *The effect of As-chain layers on the electronic structure in '112' iron-pnictides – a high-resolution ARPES study;*
   The International Conference M2S HTSC, August 23 - 28, 2015, Geneva, CH

3. I*nvestigation of the Energy Gap in lightly doped $La_{2-x}Sr_xCuO_4$*
   Summerschool on Condensed Matter Research, Materials – Structure and Magnetism, August 17 - 23, 2013, Zuoz, CH

4. *Investigation of the Energy Gap in lightly doped $La_{2-x}Sr_xCuO_4$*
   CORPES (International workshop on Strong correlations and angle-resolved photoemission spectroscopy), July 29 - August 2, 2013, Hamburg, GER

Publications

Submitted / In Preparation

1. **C. E. Matt**, N. Xu, J.Z. Ma, Z. Wang, Z. Ristic, Gen-Fu Chen, N.C. Plumb, M. Radovic, T. Birol, G. Kotliar, J. Mesot, M. Shi; *Effect of metallic spacer layer on electronic correlations in 112 Fe-based superconductors*; in preparation
2. **C. E. Matt**, N. Xu, J.Z. Ma, Z. Wang, Z. Ristic, Gen-Fu Chen, N.C. Plumb, M. Radovic, T. Birol, G. Kotliar, J. Mesot, M. Shi; *Topological nature of As-chain like spacer layer in 112 Fe-based superconductors;* in preparation
3. **C. E. Matt**, N. Xu, Baiqing Lv, J.Z. Ma, Z. Wang, Sergey Katrych, N.C. Plumb, M. Radovic, J. Mesot, M. Shi; *Electronic structure of the '1111'- related 42214 iron-pnictide, without surface states*, in preparation
4. N. Xu, G. Autès, **C. E. Matt**, B. Q. Lv, F. Bisti, V. N. Strocov, D. Gawryluk, E. Pomjakushina, K. Conder, N. C. Plumb, M. Radovic, T. Qian, O. V. Yazyev, J. Mesot, H. Ding and M. Shi; *Distinct evolutions of Weyl quasi-particles and Fermi arcs with bulk band topology in Weyl semimetals*, in preparation
5. D. Sutter, C. G. Fatuzzo, S. Moser, R. Fittipaldi, A. Vecchione, Y. Sassa, F. Cossalter, G. Gatti, M. Grioni, H. M. Rønnow, N. C. Plumb, **C.E. Matt**, M. Shi, M. Hoesch, T. K. Kim, H.-T Jeng, T.-R. Chang T. Neupert and J. Chang; *Two-gap electronic band structure in the Mott-insulator Ca2RuO4;* in preparation
6. E. Razzoli, **C. E. Matt**, Y. Sassa, M. Mansson, O. Tjernberg, G. Drachuck, M. Monomo, M. Oda, T. Kurosawa, Y. Huang, N. C. Plumb, M. Radovic, A Keren, L. Patthey, J. Mesot, M. Shi; *Rotation symmetry breaking in $La_{2-x}Sr_xCuO_4$ revealed by ARPES;* Submitted
7. N. Xu, Z. J. Wang, A. P. Weber, A. Magrez, P. Bugnon, H. Berger, **C. E. Matt**, J. Z. Ma, B. B. Fu, B. Q. Lv, N. C. Plumb, M. Radovic, E. Pomjakushina, K. Conder, T. Qian, J. H. Dil, J. Mesot, H. Ding, M. Shi; *Discovery of Weyl semimetal state violating Lorentz invariance in MoTe2;* submitted
8. N. Xu, **C. E. Matt**, E. Pomjakushina, J. H. Dil, G. Landolt, J. –Z. Ma, X. Shi, R. S. Dhaka, N. C. Plumb, M. Radovic, V. N. Strocov, T. K. Kim, M. Hoesch, K. Conder, J. Mesot, H. Ding, M. Shi; *Surface vs bulk electronic structures of a moderately correlated topological insulator YbB_6 revealed by ARPES;* Under reviewing

Published

1. **C. E. Matt**, N. Xu, Baiqing Lv, Junzhang Ma, F. Bisti, J. Park, T. Shang, Chongde Cao, Yu Song, Andriy H. Nevidomskyy, Pengcheng Dai, L. Patthey, N.C. Plumb, M. Radovic, J. Mesot and M. Shi; *$NaFe_{0.56}Cu_{0.44}As$: A pnictide insulating phase induced by on-site Coulomb interaction;* Phys. Rev. Lett. 117, 097001 (2016)

2. N. C. Plumb, D. J. Gawryluk, Y. Wang, Z. Ristić, J. Park, B. Q. Lv, Z. Wang, **C. E. Matt**, N. Xu, T. Shang, K. Conder, J. Mesot, S. Johnston, M. Shi, and M. Radović; *Momentum-Resolved Electronic Structure of the High-Tc Superconductor Parent Compound BaBiO;* Phys. Rev. Lett. 117, 037002 (2016)

3. N. Xu, H.M. Weng, B.Q. Lv, **C.E. Matt**, J. Park, F. Bisti, V.N. Strocov, D. Gawryluk, E. Pomjakushina, K. Conder, N.C. Plumb, M. Radovic, G. Autes, O.V. Yazyev, Z. Fang, X. Dai, T. Qian, J. Mesot, H. Ding, M. Shi; *Observation of Weyl nodes and Fermi arcs in tantalum phosphide*; Nat Comm. 7; 11006 (2016)

4. X. Shi, P. Richard, Kefeng Wang, M. Liu, **C. E. Matt**, N. Xu, R. S. Dhaka, Z. Ristic, T. Qian, Y.-F. Yang, C. Petrovic M. Shi and H. Ding *, Observation of Dirac-like band dispersion in LaAgSb2*, Phys. Rev. B 93, 081105(R) (2016)

5. C. Monney, **C. E. Matt**, O. J. Lipscombe, J. Mesot, J. Chang, V. N. Strocov, T. Schmitt and S. M. Hayden; *Resonant inelastic x-ray scattering study of the spin and charge excitations in the overdoped superconductor La1.77Sr0.23CuO4;* Phys. Rev. B 93, 075103 (2015)

6. A. Charnukha, D. V. Evtushinsky, **C. E. Matt**, N. Xu, M. Shi, B. Buchner, N. D. Zhigadlo, B. Batlogg and S. V. Borisenko; *High-temperature superconductivity from fine-tuning of Fermi-surface singularities in iron oxypnictides;* Scientific Reports 5, 18273 (2015)

7. Chang Liu, Guang Bian, Tay-Rong Chang, Kedong Wang, Su-Yang Xu, Ilya Belopolski, Irek Miotkowski, Helin Cao, Koji Miyamoto, Chaoqiang Xu, **Christian E. Matt**, Thorsten Schmitt, Nasser Alidoust, Madhab Neupane, Horng-Tay Jeng, Hsin Lin, Arun Bansil, Vladimir N. Strocov, Mark Bissen, Alexei V. Fedorov, Xudong Xiao, Taichi Okuda, Yong P. Chen, and M. Zahid Hasan; *Tunable spin helical Dirac quasiparticles on the surface of three-dimensional HgTe*; Phys. Rev. B 92, 115436 (2015)

8. B. Q. Lv, S. Muff, T. Qian, Z. D. Song, S. M. Nie, N. Xu, P. Richard, **C. E. Matt**, N. C. Plumb, L. X. Zhao, G. F. Chen, Z. Fang, X. Dai, J. H. Dil, J. Mesot, M. Shi, H. M. Weng, H. Ding; *Observation of Fermi arc spin texture in TaAs;* Phys. Rev. Lett. 115, 217601 (2015)

9. **C. E. Matt**, C. G. Fatuzzo, Y. Sassa, M. Mansson, S. Fatale, V. Bitetta, X. Shi, S. Pailhes, M. H. Berntsen, T. Kurosawa, M. Oda, N. Momono, O. J. Lipscombe, S. M. Hayden, J. -Q. Yan, J. -S. Zhou, J. B. Goodenough, S. Pyon, T. Takayama, H. Takagi, L. Patthey, A. Bendounan, E. Razzoli, M. Shi, N.C. Plumb, M. Radovic, M. Grioni, J. Mesot, O. Tjernberg, and J. Chang; *Electron scattering, charge order and pseudogap physics in $La_{1.6-x}Nd_{0.4}Sr_xCuO_4$: An angle resolved photoemission spectroscopy study;* Phys. Rev. B 92, 134524 (2015)

10. B. Q. Lv, N. Xu, H. M. Weng, J. Z. Ma, P. Richard, X. C. Huang, L. X. Zhao, G. F. Chen, **C. E. Matt**, F. Bisti, V. N. Strocov, J. Mesot, Z. Fang, X. Dai, T. Qian, M. Shi, and H. Ding; *Observation of Weyl nodes in TaAs;* Nat Phys 11, 724–727 (2015)

11. N. Xu, **C. E. Matt**, P. Richard, A. van Roekeghem, S. Biermann, X. Shi, S.-F. Wu, H. W. Liu, D. Chen, T. Qian, N. C. Plumb, M. Radovic, Hangdong Wang, Qianhui Mao, Jianhua Du, Minghu Fang, J. Mesot, H. Ding, M. Shi; *Camelback-shaped band reconciles heavy electron behavior with weak electronic Coulomb correlations in superconducting $TlNi_2Se_2$;* Phys. Rev. B 92, 081116(R) (2015)

12. R. S. Dhaka, T. Das, N. C. Plumb, Z. Ristic, W. Kong, **C. E. Matt**, N. Xu, K. Dolui, E. Razzoli, M. Medarde, L. Patthey, M. Shi, M. Radovic and J. Mesot; *Tuning the metal-insulator transition in $NdNiO_3$ heterostructures via Fermi surface instability and spin-fluctuations;* Phys. Rev. B 92, 035127 (2015)

13. E. Razzoli, **C. E. Matt**, M. Kobayashi, X.-P. Wang, V. N. Strocov, A. van Roekeghem, S. Biermann, N. C. Plumb, M. Radovic, T. Schmitt, C. Capan, Z. Fisk, P. Richard, H. Ding, P. Aebi, J. Mesot, and M. Shi; *Tuning electronic correlations in transition metal pnictides: Chemistry beyond the valence count;* Phys. Rev. B 91, 214502 (2015)

14. N. Xu, **C. E. Matt**, E. Pomjakushina, X. Shi, R. S. Dhaka, N. C. Plumb, M. Radovic, P. K. Biswas, D. Evtushinsky, V. Zabolotnyy, J. H. Dil, K. Conder, J. Mesot, H. Ding, and M. Shi *Exotic Kondo crossover in a wide temperature region in the topological Kondo insulator SmB_6 revealed by high-resolution ARPES;* Phys. Rev. B 90, 085148 (2014)

15. N. Xu, P. K. Biswas, J. H. Dil, R. S. Dhaka, G. Landolt, S. Muff, **C. E. Matt**, X. Shi, N. C. Plumb, M. Radovic, E. Pomjakushina, K. Conder, A. Amato, S. V. Borisenko, R. Yu, H.-M. Weng, Z. Fang, X. Dai, J. Mesot, H. Ding, and M. Shi; *Direct observation of the spin texture in SmB_6 as evidence of the topological Kondo insulator;* Nat. Commun. 5, 4566 (2014).

16. N. C. Plumb, M. Salluzzo, E. Razzoli, M. Mansson, M. Falub, J. Krempasky, **C. E. Matt**, J. Chang, M. Schulte, J. Braun, H. Ebert, J. Minar, B. Delley, K. –J. Zhou K, T. Schmitt, M. Shi, J. Mesot, L. Patthey, M. Radovic; *Mixed Dimensionality of Confined Conducting Electrons in the Surface Region of $SrTiO_3$;* Phys. Rev. Lett. 113 086801 (2014)

17. N. Xu, X. Shi, P. K. Biswas, **C. E. Matt**, R. S. Dhaka, Y. Huang, N. C. Plumb, M. Radovic, J. H. Dil, E. Pomjakushina, K. Conder, A. Amato, Z. Salman, D. McK. Paul, J. Mesot, H. Ding, and M. Shi; *Surface and bulk electronic structure of the strongly correlated system SmB_6 and implications for a topological Kondo insulator;* Phys. Rev. B 88, 121102(R) Editors' Suggestion (2013)

18. N. C. Plumb, M. Kobayashi, M. Salluzzo, E. Razzoli, **C.E. Matt**, V. N. Strocov, K.-J. Zhou, C. Monney, T. Schmitt, M. Shi, J. Mesot, L. Patthey, M. Radovic; *From the SrTiO3 Surface to the LAlO3/SrTiO3 Interface How thickness is critical*; Arxiv 1304.5948 (2013)